Physics – Uspekhi **64** (4) 386 – 419 (2021)

INSTRUMENTS AND METHODS OF INVESTIGATION PACS numbers: **07.87.+v**, **96.30.–t**, **96.55.+z**, 97.60.Lf, 98.80.Es

Objectives of the Millimetron Space Observatory science program and technical capabilities of its realization

I D Novikov, S F Likhachev, Yu A Shchekinov, A S Andrianov, A M Baryshev, A I Vasyunin, D Z Wiebe, Th de Graauw, A G Doroshkevich, I I Zinchenko, N S Kardashev, V I Kostenko, T I Larchenkova, L N Likhacheva, A O Lyakhovets, D I Novikov, S V Pilipenko, A F Punanova, A G Rudnitsky, A V Smirnov, V I Shematovich

DOI: https://doi.org/10.3367/UFNe.2020.12.038898

Contents

Abstract. We present the scientific program of the Spectr-M project aimed at the creation and operation of the Millimetron Space Observatory (MSO) planned for launch in the late 2020s. The unique technical capabilities of the observatory will enable broadband observations of astronomical objects from 50 μm to 10 mm wavelengths with a record sensitivity (up to ~ 0.1 μJy) in the single-dish mode and with an unprecedented high angular resolution (~ 0.1 μas) in the ground-space very long baseline interferometer (SVLBI) regime. The program addresses fundamental priority issues of astrophysics and physics in general that can be solved only with the MSO capabilities: 1) the study of physical processes in the early Universe up to redshifts $z \sim 2 \times 10^6$ through measuring μ-distortions of the cosmic microwave background (CMB) spectrum, and investigation of the structure and evolution of the Universe at redshifts $z < 15$ by measuring y-distortions of the CMB spectrum; 2) the investigation of the geometry of space-time around supermassive black holes (SMBHs) in the center of our Galaxy and M87 by imaging surrounding shadows, the study of plasma properties in the shadow formation regions, and the search for observa-

I D Novikov [1,2,3,a], **S F Likhachev** [1,b], **Yu A Shchekinov** [1,4,c], **A S Andrianov** [1,d], **A M Baryshev** [1,5,e], **A I Vasyunin** [6,f], **D Z Wiebe** [7,g], **Th de Graauw** [1,5,h], **A G Doroshkevich** [1,i], **I I Zinchenko** [8,j], **N S Kardashev** [1], **V I Kostenko** [1,k], **T I Larchenkova** [1,l], **L N Likhacheva** [1,m], **A O Lyakhovets** [1,n], **D I Novikov** [1,o], **S V Pilipenko** [1,p], **A F Punanova** [6,q], **A G Rudnitsky** [1,r], **A V Smirnov** [1,s], **V I Shematovich** [7,t]
[1] Lebedev Physical Institute, Astrospace Center, Russian Academy of Sciences, ul. Profsoyuznaya 84/32, 117997 Moscow, Russian Federation
[2] The Niels Bohr International Academy, The Niels Bohr Institute, Blegdamsvej 17, DK-2100 Copenhagen, Denmark
[3] National Research Center Kurchatov Institute, pl. Akademika Kurchatova 1, 123182 Moscow, Russian Federation
[4] Raman Research Institute, C.V. Raman Avenue, 560080 Sadashiva Nagar, Bangalore, India
[5] Kapteyn Astronomical Institute, University of Groningen, PO Box 72, 9700 Groningen, Netherlands
[6] Ural Federal University named after the First President of Russia B N Yeltsin, ul. Mira 19, 620002 Ekaterinburg, Russian Federation
[7] Institute of Astronomy, Russian Academy of Sciences, ul. Pyatnitskaya 48, 119017 Moscow, Russian Federation
[8] Federal Research Center Institute of Applied Physics, Russian Academy of Sciences, ul. Ulyanova 46, 603950 Nizhny Novgorod, Russian Federation
E-mail: [a] novikov@asc.rssi.ru, [b] slikhach@asc.rssi.ru, [c] yus@asc.rssi.ru, [d] andrianovas@lebedev.ru, [e] andrey@astro.rug.nl, [f] anton.vasyunin@urfu.ru, [g] dwiebe@inasan.ru, [h] tdegraau@alma.cl, [i] dorr@asc.rssi.ru, [j] zin@appl.sci-nnov.ru, [k] vkostenko@asc.rssi.ru, [l] ltanya@asc.rssi.ru, [m] larlikh@asc.rssi.ru, [n] lyahovecao@lebedev.ru, [o] novikovdi@lebedev.ru, [p] spilipenko@asc.rssi.ru, [q] anna.punanova@urfu.ru, [r] arud@asc.rssi.ru, [s] asmirn@asc.rssi.ru, [t] shematov@inasan.ru

Received 14 April 2020, revised 7 December 2020
Uspekhi Fizicheskikh Nauk **191** (4) 404 – 443 (2021)
Translated by P Konstantinov

tional manifestations of wormholes; 3) the study of observational manifestations of the origin of life in the Universe — the search for water and biomarkers in the Galactic interstellar medium. Moreover, the technical capabilities of the MSO can help solve related problems, including the birth of the first galaxies and SMBHs ($z \gtrsim 10$), alternative approaches to measuring the Hubble constant, the physics of SMBHs in 'dusty' galactic nuclei, the study of protoplanetary disks and water transport in them, and the study of 'ocean worlds' in the Solar System.

Keywords: submillimeter astronomy, Millimetron Space Observatory, supermassive black holes, wormholes, cosmic microwave background, early Universe, origin of galaxies, interstellar medium, water and biomarkers in the Galaxy, Solar System

1. Introduction

A revolutionary breakthrough in astrophysics made by major space projects like COBE (COsmic Background Explorer), WMAP (Wilkinson Microwave Anisotropy Probe), Hubble, Planck, Chandra, and Fermi-LAT (Large Area Telescope) has significantly expanded our understanding of the Universe in the entire electromagnetic spectrum from microwaves to GeV gamma rays. The main achievements are a more profound understanding of the content of the Universe, its large-scale structure formation and evolution, the evolution of nearby and very distant galaxies (at redshifts $z = 1.5-3$) at the epoch of maximum star formation rate, etc. Thanks to these achievements, observational astronomy has come to the edge of 'new physics' related to the origin of the Universe, its content, and the nature of forces acting in it. To go beyond this threshold, it is necessary to increase the sensitivity of instruments, expand their wavelength band, and substantially increase the spatial (angular) and spectral resolutions. Many large scientific institutions and separate research groups worldwide are pursuing these tasks. Very recently (on July 13, 2019), in Russia, a new space observatory, Spektr-RG (Spektr-Roentgen-Gamma), [1] was launched. Presently, two space observatories are under construction which, together with Spektr-RG, are destined to acquire new knowledge beyond the 'threshold'. They are the World Space Observatory — Ultraviolet (Spektr-UF project, to be launched in 2025) and the Millimetron Space Observatory (MSO, the Spektr-M project, proposed for launch in 2029). The Millimetron Space Observatory will cover a broad spectral band (more than two orders of magnitude) from 50 μm to 10 mm (frequency range from 30 GHz to 6 THz). The observatory can operate in two different observational modes: a single-dish space observatory with a 10-m telescope and an arm of a ground-space very long baseline interferometer (SVLBI) [1–3]. Here, we will discuss the scientific tasks planned for MSO.

1.1 Millimetron Space Observatory for fundamental science

The scientific program of the Millimetron space observatory addresses problems that will enable obtaining fundamentally vital information to solve the following key questions: 1) which physical processes took place in the early Universe before recombination, what determines the parameters of the large-scale structure of the Universe, when and how did the first stars and galaxies emerge and how are they related to nearby stars and galaxies; 2) what is the structure of space-time in the vicinity of massive gravitating bodies, what is their nature, when and how did they emerge; 3) how was life in the Universe born, is it unique or ubiquitous in the Universe, what are the forms of life and their observational manifestations.

The limited, at first glance, list of tasks assumes the investigation of vast fields encompassing extensive time and space scales, starting with planetary systems and protoplanetary disks to central relatively compact regions in our and nearby galaxies, to scales of billions of light years, from our time to the very first instants after the birth of the Universe. Many future international space projects aim to solve particular aspects of the problems included in the MSO program. For example, the James Webb Space Telescope (JWST, 2021), the Wide Field Infra Red Space Telescope (WFIRST, proposed for 2025) in the near IR band, and the space telescope PICO (Probe of Inflation and Cosmic Origin, planned for 2030) will operate in spectral ranges from 400 μm to 1.5 cm, supplementary to the Millimetron band. The Origins Space Telescope (OST) science program partially overlaps that of MSO, but it is anticipated for launch in 2037. Here, we should mention the Laser Interferometer Space Antenna (LISA) that will be able to detect gravitational waves from SMBH coalescences, dynamical processes at the inflationary stage in the early Universe, and other phenomena related to ultra-strong gravitational fields.

The Millimetron Space Observatory plays a unique role in solving these problems, due to several factors. First of all, it will operate in the broad (almost two and a half orders of magnitude) wavelength interval $\lambda = 50-10^4$ μm. Second, the telescope's high sensitivity will be provided by active cooling of the mirror to $T \leqslant 5$ K and its diameter of 10 m, larger than the diameter of all the telescopes mentioned above. Third, the possibility of operating in the SVLBI mode will provide an unprecedentedly high angular resolution of ~ 0.1 micro arcsecond.

1.2 Principles of the scientific program of Spectr-M

The project's scientific program focuses on studying fundamental phenomena and objects from the three fields mentioned above (Section 1.1). The program has a hierarchical structure: each direction is based on a key ('breakthrough') project around which second-level related projects are developed. Such a narrow-focused hierarchical structure is motivated by the telescope's limited operational time in the active cooling regime [1–3]. Therefore, the strategy and planning of observations will be tightly connected to this regime. In our opinion, this will enable the most in-depth investigation of the physics and evolution of the objects and phenomena in each key project by the maximum effective use of MSO's capabilities. Schematically, it can be described as follows.

The principal goal of the *key projects* is to answer the following unsolved issues.

• Fundamental processes in the early Universe. Here, the *key project* is to discover y- and μ-distortions in the spectrum of the cosmic microwave background radiation, which are specific forms of deviations of the CMB from the black-body spectrum.

• Properties of space-time and matter in superstrong gravitational fields. The *key project* here is to probe the space-time geometry in the vicinity of Sgr A* in the galactic

[1] The first results of the Spektr-RG project were presented at the conference High Energy Astrophysics — Today and Tomorrow, 2019, see http://heaconf.cosmos.ru/2019/circ1_hea2019.html.

center and SMBHs in nearby galaxies in the SVLBI regime and reveal observational manifestations of wormholes.

• Origin of life in the Universe. The *key project* here is to search for prebiotic molecules in protostellar clouds and protoplanetary disks, search for water in habitable zones of protoplanetary disks, and clarify the nature of the chirality of complex organic molecules.

Each of the *second-level* projects is related to one of the *key projects*. For example, the measurements of CMB spectral distortions are closely associated with searches for various appearances of the Sunyaev–Zeldovich effect and its relativistic corrections in galaxy clusters. Thus, the *second-level projects* will address the following problems:

1. Cosmology: 1) an alternative method of measurement of the Hubble constant H_0, 2) studies of the Sunyaev–Zeldovich effect and its relativistic corrections, 3) observations of the first galaxies, 4) the discovery and investigation of supermassive black holes in the Universe close to the reionization epoch, 5) the study of properties of dusty infrared galaxies, 6) the study of features of galaxy evolution in the 'noon' Universe, i.e., at the time of the global star formation burst at $z \sim 2$.

2. Superstrong gravitational fields: 1) multifrequency polarization observations of the closest vicinity of black holes in Sgr A*, M87*, 2) the study of turbulence of accretion flows around black holes by measuring its possible spectral, polarization, and time variations, 3) the estimation of parameters of the accretion flow by measuring its multiwavelength brightness spectrum close to BH (~ 0.1 milliarcsec) and in a broader region up to the Bondi radius ($\sim 0.03-0.1$ pc) around Sgr A*, 4) multifrequency polarization observations of the vicinity of black holes in Sgr A*, M87* to measure the magnetic field topology and strength in the broad region up to the Bondi radius, 5) the investigation of physical processes in obscured active galactic nuclei; the search for the activity of SMBHs there, 6) the spectroscopy of giant black holes at the beginning of the reionization epoch ($z \gtrsim 7.5$), the study of the evolutionary growth of black holes in the 'dark ages' at $z = 10-30$, 7) observational appearances of the mutual interaction of galaxies and growing black holes in their centers; the identification of mechanisms determining their concordant evolution.

3. Water in space, the origin of life: 1) filamentary structure of the interstellar medium, giant molecular clouds, and star formation regions close to the Sun, 2) the study of the transport of water into the inner parts of protoplanetary disks from measurements of their spectral features, 3) observational appearances of the formation of Earth-like planets, the habitability zones; effects of the flaring activity of red dwarfs on the physical properties of protoplanetary disks inside the assumed habitability zones, 4) the investigation and estimation of water reservoirs in the Solar System.

1.3 Necessity and importance of the Millimetron Space Observatory

In the last 30 years, our perceptions about the initial evolution of the Universe and the present state of objects have changed dramatically. A 'minimal' 6-parametric model of the Universe (ΛCDM-model with cold dark matter and cosmological constant Λ) was constructed. The model is based on measurements of angular variations of the CMB spectrum with unprecedented accuracy [4–6]. Careful measurements of type Ia supernovae in the Supernova Cosmology Project carried out with the Hubble Space Telescope (HST) led to the discovery of accelerating expansion of the Universe [7, 8]. Deep and ultra-deep HST surveys from the near-IR to the ultraviolet spectrum enabled the discovery of a galaxy with record redshift $z = 11$ [9]. (Interestingly, this galaxy's stellar population has a chemical makeup with the mass proportion of heavy elements of only one third that of the Sun's.) The Herschel and Spitzer space observatories demonstrated that dust in the Universe arose simultaneously with the first galaxies (see, for example, [10, 11]). The Einstein, ROSAT(ROentgen SATellit), and Chandra X-ray observatories discovered giant reservoirs of hot gas in galaxy clusters and explored many high-energy sources in the Universe. In particular, the Chandra Observatory detected X-ray emission from the SMBH in the center of our Galaxy (Sgr A*) [12], discovered traces of dark matter interaction with baryons in the coalescing Bullet galaxy cluster [13], detected a hot gas halo around nearby galaxies [14], etc. The Fermi-LAT gamma-ray telescope discovered, among other things, unusual and unexpectedly energetic activity from the galactic center, which appears as two giant bubbles with a size of 10 kpc symmetrically blown from the galactic center. The detection of gravitational waves in 2016 by the gravitational-wave interferometers LIGO and Virgo [15] was the most striking discovery in recent years. This discovery can be, without exaggeration, called a revolutionary event, after which physics crossed a threshold beyond which properties of space-time can be directly probed. In a certain sense, the Planck space mission reached a similar threshold by demonstrating the possibility of measuring the so-called *B*-mode of the CMB polarization that embodies information about the birth and very first instants of the Universe's evolution — the inflationary stage [16]. Contemporary astronomy approached another 'threshold' task — probing space-time near the black hole event horizon by studying the black hole shadow.

The Event Horizon Telescope (EHT) collaboration recently announced the successful completion of imaging the shadow around the SMBH in galaxy M87 [17]. The image was obtained at a wavelength of 1.3 mm by eight telescopes located at various places around the globe (see [18]). This result was obtained essentially at the limit of modern capabilities. Namely, the EHT experiment used the maximum available VLBI bases on the order of Earth's diameter and the minimum possible wavelength of 1.3 mm to optimally fill the (u, v)-plane. Therefore, with the achieved angular resolution of ~ 20 microarcsec, the construction of the shadow image with an angular diameter of $\simeq 42$ microarcsec required very sophisticated data processing, including statistical analysis of more than 60,000 synthetic images [19, 20]. [2] To get more reliable images of the black hole shadow in M87 and, possibly, in Sgr A*, and investigate in detail *the space-time geometry and physics of the surrounding phenomena*, instruments operating in the SVLBI regime at a shorter wavelength capable of reaching the necessary angular resolution are needed. Real progress will be achieved by the Millimetron Space Observatory, enabling SVLBI observations with a base from $\simeq 400{,}000$ to 1.5 mln km and a maximum angular resolution of better than ~ 0.4 and ~ 0.1 microarcsec, respectively. Thus, presently, MSO is the only project under development capable of accomplishing this task.

[2] For this reason, the estimate of the shadow size, 42 ± 3 microarcsec, should be taken in the statistical sense. The same can be said about the shadow asymmetry $\Delta\theta \leqslant 2\%$ estimate, one of the essential parameters for reliably measuring the space-time geometry.

Other actual fundamental problems relate to the origin of life in the Solar System and the Universe in general. The widespread attention to this problem is evident. This issue stems from Giordano Bruno's times and can be undoubtedly related to the 'threshold' tasks. As of the time of writing this paper (April 8, 2020), 4189 exoplanets are known outside the Solar System.[3] They orbit around 3105 stars and stellar objects. The nearest planet, Proxima Centauri b, is located at a distance of 1.3 pc (slightly above four light years). Most current studies of exoplanets and their atmospheres are carried out in the optical and near-infrared spectra. However, the far-infrared and submillimetre ranges are crucial for many problems related to the formation of exoplanets, their characteristics in the habitability zones, and the transport of chemical elements and water vital for the birth of life into these zones. The study of these problems has just begun, and Millimetron's high sensitivity, spectral resolution, unprecedented angular resolution, and broad spectral coverage will be crucial in solving these issues.

Thus, the Spektr-M project's creation of the Millimetron Space Observatory with its planned features is needed right now, when further progress in science cannot be achieved with previous-generation instrumentation but requires extending the range and increasing the sensitivity and angular resolution.

1.4 Technical characteristics of the Millimetron Space Observatory

As noted above, the international project Spektr-M aimed at developing and constructing the Millimetron Space Observatory stands out among other space projects of the next decade. First of all, this is due to the unique technical characteristics of Millimetron: the large aperture of the primary mirror (10 m), the low temperature of the input optics of the telescope ($T \leqslant 5$ K), and the high surface accuracy (rms error of the optical part is $\leqslant 10$ μm according to the technical requirements (TRs) and $\leqslant 6$ μm according to the current state of manufacturing the optical components and units). Jointly, this will enable the instrument to reach high sensitivity and angular resolution (Fig. 1). The telescope will operate in an unprecedentedly broad wavelength range from 50 μm to 10 mm. In addition, MSO will be able to make observations in two different regimes: as a single space telescope with the unique characteristics presented above and as a space arm of a ground-space very long base radio interferometer. The latter, in combination with the ground arm (for example, ALMA (Atacama Large Millimeter/submillimeter Array)[4] or EHT telescopes [18]) will enable an unprecedented angular resolution of $\Delta\theta \sim 0.1$ microarcseconds. The telescope's scientific instrumentation will include several receivers with specific technical features optimized for particular tasks. The high-resolution spectrometer (HRS) consists of high-sensitivity matrix heterodyne receivers tuned to operate in the frequency range from 0.5 to 6 THz. This device will provide observations with a high spectral resolution of $R \geqslant 10^5$, equivalent to a line width of $\Delta v \leqslant 3$ km s^{-1}. Some spectral bands in the HRS range are fully absorbed in the atmosphere and only partially available for observations from high-mountain observatories (see the discussions in [1, 2, 21]), rendering MSO a unique tool to carry out spectroscopic research impossible with other instruments. The cold and high-precision optical equipment makes it suitable for installing far-IR CCD (cameras and medium-resolution spectrometers) with a noise-equivalent power (NEP) below 10^{-19} W Hz$^{-0.5}$. This equipment will allow MSO to map and measure the faintest spectrum from astronomical sources at a natural noise level $\lambda \leqslant 3000$ μm. The MSO will be equipped with several high-sensitivity heterodyne receivers tuned to operate in the interferometer mode at frequencies from 33 to $\simeq 720$ GHz. In combination with the ground-space interferometer $\geqslant 1.5$ mln km baseline, these detectors will make it possible to study the most compact objects in the Universe, such as quasars, black holes, and their surroundings.

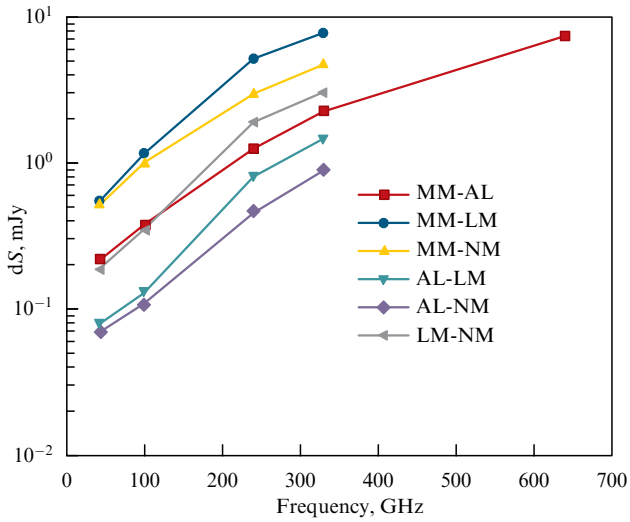

Figure 1. Sensitivity δS (rms deviation) of some space-Earth interferometers compared to the Millimetron Space Observatory at frequencies of 43, 100, 240, 330, and 640 GHz, $\Delta v = 4$ GHz. MM — Millimetron, AL — ALMA, LM — LMT (Large Millimeter Telescope), NM — NOEMA (NOrthern Extended Millimeter Array).

A more detailed analysis of the capabilities of MSO to address specific scientific problems taking into account the technical characteristics of the mission can be found, for example, in papers [22, 23].

1.4.1 Millimetron Space Observatory sensitivity in the SVLBI regime. As noted above, Millimetron stipulates two operation regimes of the on-board 10-m antenna:

- single-dish mode to perform survey and dedicated multi-frequency photometric, spectroscopic, and cosmological observations;
- SVLBI mode realized jointly with a network of ground-based radio telescopes, for example, the EHT global array, that can potentially include more than ten radio telescopes with different apertures from 10 to 80 m [18] and compatible frequency bands of 43, 100, 240, 330, and 640 GHz (wavelength 7.00, 3.33, 1.25, 0.91, and 0.47 mm, respectively). During the first three years of MSO's work, the two-mode operation in the vicinity of the L2 point is envisaged. After that, it is possible (but not obligatory) that the telescope will be transported to a near-Earth orbit where only SVLBI observations will be possible. Priority tasks of MSO in the SVLBI regime include the imaging (mapping of radiation intensity in the sky) of shadows from supermassive black holes (Sgr A*, M87*) and other compact objects included in the scientific program.

[3] https://exoplanetsarchive.ipac.caltech.edu.
[4] https://almaobservatory.org/en/about-alma-at-first-glance/.

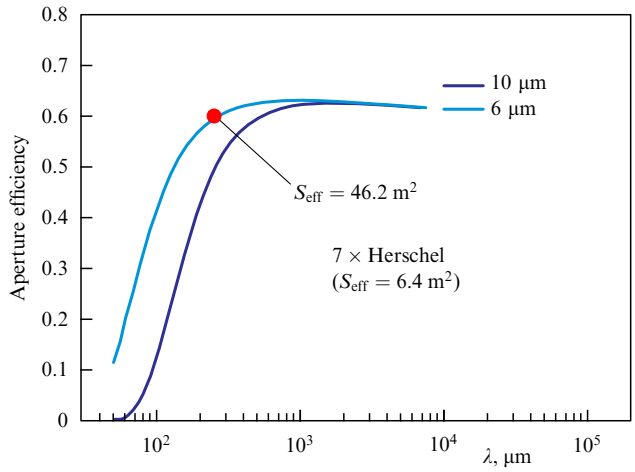

Figure 2. Efficiency of the 10-m Millimetron mirror as a function of wavelength for rms surface deviations of 6 and 10 μm.

The main parameter determining the antenna sensitivity is the spectral equivalent flux density (SEFD),

$$\mathrm{SEFD} = \frac{2760\, T_{\rm sys}}{A_{\rm eff}} \quad [\mathrm{Jy}]\,, \tag{1}$$

where $T_{\rm sys}$ [K] is the system's temperature, and $A_{\rm eff}$ [m^2] is the antenna's effective area. The lower the SEFD, the more effective the antenna system. The efficiency of the 10-m Millimetron antenna as a function of wavelength is presented in Fig. 2. The sensitivity of the 2-element interferometer in units of the flux density Jy is determined by thermal noise, which depends on the SEFD of individual dishes, frequency bandwidth $\Delta\nu$ [Hz], integration time τ [s], and the correction accounting for the quantization losses P_q during digital signal registration [24]:

$$\delta S = \frac{1}{P_q}\sqrt{\frac{\mathrm{SEFD}_1\ \mathrm{SEFD}_2}{2\Delta\nu\tau}} \quad [\mathrm{Jy}]\,. \tag{2}$$

In Millimetron, 1- and 2-bit quantization can be used with the correction coefficient P_q, 0.64 and 0.88, respectively. To estimate the integral SEFD parameter and sensitivity δS for the entire antenna array consisting of N elements, one can use the approximate expression [18, 19]

$$\mathrm{SEFD}_{\rm array} = \frac{1}{\rho_{\rm ph}}\left(\sum_{i=1}^{N}\frac{1}{\mathrm{SEFD}_i}\right)^{-1}, \tag{3}$$

where $\rho_{\rm ph}\,(\leqslant 1)$ is the coefficient of losses of a phased antenna array consisting of N elements.

To recover images of the nearest SMBHs, high-frequency submillimeter observations at 220–250 GHz, 330–360 GHz, and above are preferable due to less significant refractive interstellar scattering effects [25], enabling higher angular resolution of shadows around SMBHs. However, unlike the Millimetron Space Observatory, the sensitivity of the ground antennas decreases at higher frequencies because of higher temperatures, higher efficiency losses due to mirror quality, and phase fluctuations caused by the atmosphere that shorten the coherent accumulation time of the signal (equations (1), (2)).

Table 2. Integral sensitivity of the four-antenna array (Table 1) depending on the frequency band. The detection band is $\Delta\nu = 4$ GHz; integration time τ is from Table 1.

Frequency, GHz	δS, mJy
43	0.18
100	0.30
240	1.12
330	1.84

Table 1 presents SEFD estimates of the 10-m antenna of Millimetron and the parameters of four of the most effective ground-based EHT antennas [18, 19] that can be used in the project's SVLBI. Figure 1 allows one to assess the comparable sensitivity δS for some ground–space interferometers with Millimetron. The integral calculated sensitivity (3) for the entire antenna array of four dishes (Table 1) at five frequencies is listed in Table 2.

1.4.2 Orbit of the Millimetron Space Observatory. The Millimetron Space Observatory will operate near the Sun–Earth L2 libration point in a halo orbit. Such an orbit facilitates the telescope's active cooling system and therefore is the most suitable for the single-dish mode requiring the best sensitivity. In the SVLBI mode, this orbit provides an unprecedented angular resolution. The halo orbit is located at 1.5 mln km in the direction opposite the Sun. The maximum height of the space apparatus from the ecliptics is 910,000 km. The orbital period is 180 days.

Presently, an additional orbital configuration for Millimetron is being considered. The apparatus's return on a near-Earth orbit is planned after the key scientific program for the single-dish mode near the L2 point is completed. The near-Earth orbit provides more capabilities for the SVLBI regime, in particular, for high-quality two-dimensional imaging of black hole shadows. An elongated elliptical orbit appears to be optimal for the near-Earth orbit configuration. A gravitational maneuver near the Moon can help the transfer from the halo orbit at the L2 point to an elliptical orbit with an apogee of up to 340,000 km and a high eccentricity (>0.9) without significant energy expenditures ($\Delta\nu \sim 100$ m s^{-1}) [26]. Such an elongated elliptical orbit has an apogee of 320,000 km, a perigee of 10,000 km, and an orbital period of 10 days.

Table 1. Heterodyne detection efficiency for four antennas at five frequencies of the Millimetron Space Observatory. The signal detection band $\Delta\nu = 4$ GHz.

Antenna/antenna system	SEFD, Jy				
	43 GHz	100 GHz	240 GHz	330 GHz	640 GHz
Millimetron (MM), $d = 10$ m	1172	2305	2551	3402	6805
ALMA (AL), 50 × 12 m, equiv. $d = 85$ m	24	29	62	122	159
LMT (LM), $d = 50$ m	151	281	1055	1444	0
NOEMA (NM), 12 × 15 m, equiv. $d = 52$ m	136	210	347	520	0
τ, s	150	120	25	20	5

2. Cosmology

2.1 Distortions of the CMB spectrum

The search for CMB spectral distortions, i.e., deviations from the black-body spectrum, is a fundamental problem of modern observational cosmology. The first CMB measurements by the COBE/FIRAS (Far InfraRed Absolute Spectrophotometer) experiment [27] firmly established the spectrum's black-body shape. Since then, no attempts have been undertaken to discover any deviations from the black-body spectral distribution. Nevertheless, in the pre-recombination epoch in the Universe, there were processes with energy release [28–32] that should have left inevitable footprints in the form of characteristic spectral distortions. Such distortions also appear in a comparably late Universe after recombination due to photon scatterings in a hot plasma [33, 34]. These distortions bear unique information on the physical processes at different evolutionary stages of the Universe related to deviations from thermal equilibrium. Spectral distortions arise due to energy injection into plasma. They can evidence the existence of possible primordial black holes [35], unstable particles with a lifetime of $10^9 - 10^{10}$ s [36], and acoustic wave dissipation and bear information on the power spectrum of primordial fluctuations at small scales [37, 38]. It is important to note that any other observations but spectral CMB distortions cannot probe the primordial small-scale perturbations. Such perturbations do not leave traces in the CMB anisotropy because of dissipation processes and in the large-scale structure of the Universe due to strong nonlinearity at small scales. Simultaneously, distortions produced in the late epoch embody information on the emergence of the large-scale structure of the Universe, the intergalactic medium, and galaxy clusters.

The discovery of CMB distortions will open a totally new and so far unavailable informational channel on the structure and evolution of the Universe.

This section considers some processes that can lead to CMB frequency distortions and analyze the Millimetron's capabilities to observe them.

2.1.1 Arising and structure of spectral distortions. During the evolution of the Universe, there were several qualitatively different stages of the interaction of radiation with matter. At the earliest stage at redshifts $z > 2 \times 10^6$, double Compton scattering and bremsstrahlung radiation were strong enough to maintain close thermodynamical equilibrium between matter and radiation. At this stage, any energy injection into plasma (a process accompanied by energy release) leads to rapid thermalization, i.e., equilibration of radiation with plasma, which results in temperature growth while preserving the black-body radiation spectrum. This stage in the history of the Universe is dubbed the T-era (Fig. 3). The efficiency of double Compton scattering and free-free processes decreases with time, and at $z < 2 \times 10^6$, these effects are negligible. Thus, starting from this moment, the total number of photons is preserved, and the radiation spectrum evolution is described by the Kompaneets equation [39]:

$$\frac{\partial n}{\partial t} = \frac{\sigma_T N_e h}{m_e c} \frac{1}{v^2} \frac{\partial}{\partial v} v^4 \left(n + n^2 + \frac{kT_e}{h} \frac{\partial n}{\partial v} \right), \qquad (4)$$

$$hv,\ kT_e \ll m_e c^2;$$

the solution to this equation depends on the time of the energy (or photon) 'injection' into the plasma. (Here, $n(v)$ is the occupation number of photons, h and k are the Planck and Boltzmann constants, respectively, c is the speed of light, m_e is the electron rest mass, σ_T is the Thomson scattering cross section, N_e is the electron number density, and T_e is the plasma temperature.) If the injection occurred at redshifts $10^5 < z < 2 \times 10^6$, a Bose–Einstein spectrum with nonzero chemical potential μ is the solution to the Kompaneets equation. Such perturbations are called μ-distortions, and the corresponding epoch in the evolution of the Universe is called the μ-era. Suppose the energy injection occurs at later times, from $z \sim 10^4$ to $z \sim 10^3$. In that case, the radiation has no time to equilibrate with the matter before recombination. So-called y-distortions arise in the CMB spectrum (following the commonly used notation of the photon Comptonization parameter in plasma, $y = (kT_e/m_e c^2) N_e \sigma_T c t$). The spectral form of such distortions amounts to the Sunyaev–Zeldovich effect [40], and the corresponding era in the history of the Universe is called the Y-era. Distortions with the same spectral shape also appear after recombination at low redshifts $z < 10$ during the large-scale structure formation, when photons are scattered on hot plasma.

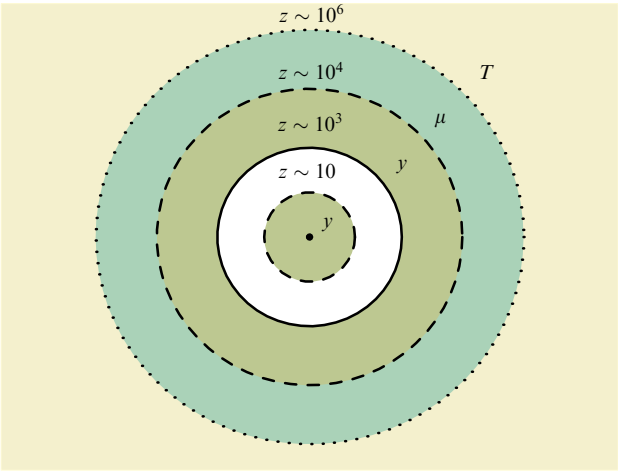

Figure 3. CMB frequency evolution stages: T-era at $z > 2 \times 10^6$ (black-body spectrum conservation), μ-era at $5 \times 10^4 < z < 2 \times 10^6$ (μ-deviation era), and Y-era at $1.4 \times 10^3 < z < 5 \times 10^4$ and $z < 10$ (appearance of y-deviations). The observer is at the center.

Thus, from the point of view of the CMB spectrum evolution, the Universe passes through three stages (Fig. 3): 1 — at redshifts above 2×10^6 any energy injection leads to rapid thermalization, and the spectrum preserves the black-body shape with a somewhat different temperature; 2 — at redshifts $5 \times 10^4 < z < 2 \times 10^6$, μ-distortions arise; 3 — at $z < 5 \times 10^4$, the epoch of y-distortions begins.

μ- and y-distortions have the following form [41]:

$$\Delta I_\mu = I_{CMB} \frac{x e^x}{e^x - 1} \left(\frac{1}{\beta} - \frac{1}{x} \right) \mu,$$

$$\Delta I_y = I_{CMB} \frac{x e^x}{e^x - 1} \left(Y_0(x) + \Theta_e Y_1(x) \right) y, \qquad (5)$$

$$I_{CMB} = \frac{2hv^3}{c^2} \frac{1}{e^x - 1}, \quad \Theta_e = \frac{kT_e}{m_e c^2}, \quad x = \frac{hv}{kT_r};$$

here, $I_{CMB} = (2hv^3/c^2)n$ is the CMB intensity, T_r is its temperature $\Theta_e = kT_e/m_e c^2$, μ and y are amplitudes of μ- and y-distortions, respectively, and $Y_0(x)$ and $Y_1(x)$ represent the thermal Sunyaev–Zeldovich effect and its first relativistic

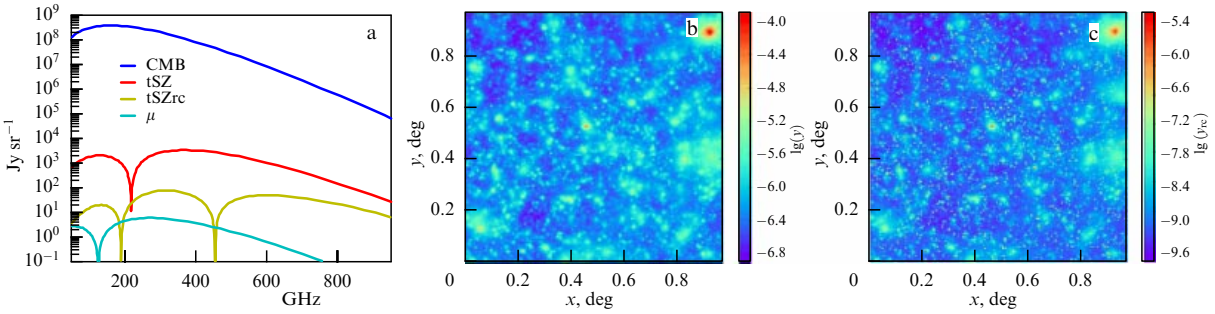

Figure 4. (Color online.) (a) CMB spectrum (in dark blue), y-distortion spectrum (in red), the first relativistic correction to y-distortions and μ-distortions (in yellow and in blue, respectively). (b) A numerical model of a $1^\circ \times 1^\circ$ (100×100 pixels) map of the y-distortion amplitude. (c) The same as in (b) for the first relativistic correction to y-distortions. Numerical modeling of these maps courtesy of Klaus Dolag.

correction, respectively. It should be noted that equation (4) is presented in this paper in the original form, without relativistic corrections. Taking into account corrections up to Θ_e^5, such an equation was derived in paper [42]. If no unknown energy release occurred in the μ-epoch and the expected CMB distortions were determined by acoustic wave dissipation only, a conservative estimate of the expected amplitude μ in equation (5) is 2×10^{-8}. The approximate estimation of y is 1.77×10^{-6}, while the mean temperature of the scattering plasma is $\Theta_e \sim 2.5 \times 10^{-3}$. The spectral form of the expected CMB distortions for these parameters is shown in Fig. 4. The amplitude of y-distortions in the sky appears as a continuous field of fluctuations with a characteristic size of about one angular minute and sufficiently bright spots from individual galaxies and clusters. The first relativistic correction amplitude behaves similarly, but small-scale fluctuations are more pronounced (Fig. 4). As for μ-distortions, in the first approximation with immense accuracy, they can be viewed as a monopole, i.e., the expected amplitude of μ is some constant across the whole sky.

2.1.2 Observations of spectral distortions against a noise background. When measuring the CMB spectrum, various galactic and extragalactic noises should be considered [43]. These noises in the frequency range from 0.1 to 1 THz are due to galactic thermal dust, synchrotron radiation, infrared background, free-free transitions, CO line emission from distant galaxies, and rotating dust emission. Unlike experiments like PIXIE (Primordial Inflation Explorer) [44], Millimetron will have a comparatively narrow field of view of $\sim 7' \times 7'$ and, hence, will be unable to survey the whole sky or a significant part of it. MSO will not have enough time to accumulate this signal. Instead, it appears worthwhile to observe comparatively small patches in the sky of the order of $1^\circ \times 1^\circ$ (Fig. 4). The cleanest sky regions will be used. To reveal such zones, we use the Planck data [45, 46]. Our preliminary analysis indicates that the cleanest very small patches in the sky enable the dust radiation effect on the resulting signal to be reduced by two orders of magnitude compared to the mean value across the sky (Fig. 5). Considering that galactic dust provides the most emission at high frequencies, we can increase the experiment sensitivity significantly.

In the considered frequency range, the CMB photon noise, the background noise from the telescope's optical elements (mainly from the primary mirror), the dust background emission discussed above, and the infrared background provide most of the photon noise restricting the capabilities of any CMB measurements, including the Millimetron observations. Other backgrounds, such as synchrotron and free-free radiation, contribute much less to the total noise and can be ignored. Simultaneously, in the data analysis, when

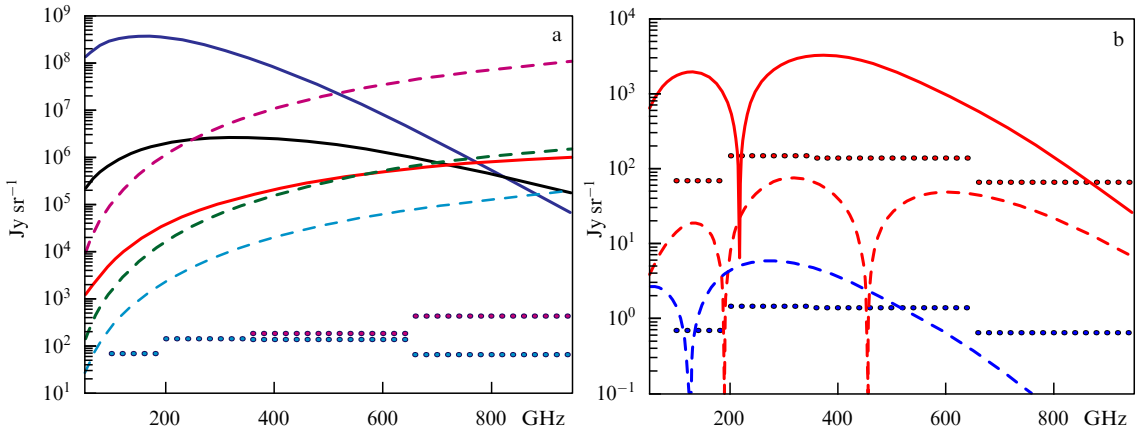

Figure 5. (Color online.) (a) CMB spectrum (blue line), mirror contribution (black line), IR background spectrum (red line). The dashed lines show the dust spectrum: the violet line for the sky-average spectrum, the green line for the mean spectrum for galactic latitudes above 30°, the blue line for the cleanest sky area. Violet and blue dots, respectively, show the sky-averaged Millimetron sensitivity and sensitivity in the sky area that is the cleanest of dust. (b) y-distortions — solid red curve, first relativistic correction — dashed red curve, μ-distortions — blue curve. The red dotted line shows the sensitivity to y-perturbations (one-hour exposure time per pixel). The blue dotted line corresponds to the signal accumulation time for the full map and shows the μ-perturbation sensitivity.

separating the signal components, they must be taken into account. The noise equivalent power (NEP) for a Fourier spectrometer in the frequency range from ν_1 to ν_2 reads [47]

$$\begin{aligned}\mathrm{NEP}^2 &= \mathrm{NEP}_\mathrm{d}^2 + \sum_{j=1}^{4} \mathrm{NEP}_j^2\,,\\ \mathrm{NEP}_j^2 &= 4\int_{\nu_1}^{\nu_2} \frac{A\Omega}{\lambda^2}\,\frac{h^2\nu^2\varepsilon_j(\nu)}{\exp\left(h\nu/kT_j\right)-1}\\ &\quad\times\left[1+\frac{\varepsilon_j(\nu)}{\exp\left(h\nu/kT_j\right)-1}\right]d\nu\,.\end{aligned} \tag{6}$$

Here, $\mathrm{NEP}_\mathrm{d}\sim 10^{-18}$ [W/$\sqrt{\mathrm{Hz}}$] is the receiver's noise power; the summation index j corresponds to the CMB noise components: $j=1$ from CMB, $j=2$ from dust, $j=3$ from the infrared background, $j=4$ from the telescope mirror, A is the effective area of the mirror, and Ω is the angular resolution. For the first three components, the temperatures T_j and dimensionless modification functions $\varepsilon_j(\nu)$ (equivalent to emission coefficients) are taken from [41]. The Millimetron mirror temperature is $T_4=5$ K and, according to preliminary estimates, $\varepsilon_4(\nu)=0.001\times[0.42+0.30(\nu/100\ \mathrm{GHz})]$. The sensitivity in the frequency range $[\nu_1:\nu_2]$, according to [48], is

$$S = 0.61\,\frac{\mathrm{NEP}}{A\Omega\delta\nu\sqrt{t}\sqrt{N_b}}\,, \tag{7}$$

where t is the signal accumulation time, $\delta\nu$ is the frequency channel width, and N_b is the number of independent receivers. In our case, $\delta\nu=20$ GHz, and the numbers N_b for different frequency bands are collected in the following table:

Band (GHz)	100:200	200:353	353:667	667:1000
N_b	6	9	16	25

Figure 5a presents the Millimetron sensitivity in units Jr sr^{-1} for the configuration of spectropolarimeters described above for observations in the patch of sky that is the cleanest of dust emission. Here, the assumed signal accumulation time per pixel in a one-by-one degree map with 100×100 pixels is one hour. This time is long enough to reproduce the y-distortions map with reasonable accuracy. The map of the first relativistic correction is also well reproduced, although with significantly lower reliability. A possible improvement in the statistics can be achieved by coarsening the map for the first relativistic correction by decreasing the resolution (smoothening of the map). As for μ-distortions, thanks to the constant amplitude over the map, the signal exposure is 10^4 times longer than that of one pixel. This increases the experiment's sensitivity to μ-distortions correspondingly by two orders of magnitude compared to y-distortions.

2.1.3 Effect of the mirror on observed spectral distortions. When separating different signal components to measure y- and μ-spectral distortions, it is necessary to take into account, besides the natural sky components, additional signals from the telescope optics (the primary mirror, first and foremost), which has a mean expected temperature of $T_m=5$ K. The mirror not only generates additional white noise in observations but also gives rise to very specific signal distortions due to inhomogeneous surface cooling. It consists of 96 panels, each with a temperature somewhat different from the mean temperature (Fig. 6). Other parts of the telescope's optical system have a temperature close to that of the primary mirror and contribute to the total signal. We use the Taylor series decomposition for convenience and to optimize the separation of signal distortions produced by the optics. The intensity produced by each small part of the mirror surface with temperature T reads

$$\begin{aligned}I_m(\nu,T) &= I_m(\nu,T_m) + \left.\frac{\partial I_m(\nu,T)}{\partial T}\right|_{T=T_m}\Delta T\\ &\quad+\frac{1}{2}\left.\frac{\partial^2 I_m(\nu,T)}{\partial T^2}\right|_{T=T_m}(\Delta T)^2+\ldots\\ &\quad+\frac{1}{n!}\left.\frac{\partial^n I_m(\nu,T)}{\partial T^n}\right|_{T=T_m}(\Delta T)^n+\ldots\,,\\ \Delta T &= T-T_m\,.\end{aligned} \tag{8}$$

Thus, the mirror contribution to the total signal can be written as the sum of several analytical functions $B_n(\nu,T_m)$:

$$\begin{aligned}I_m &= \sum_{n=0}^{N}\gamma_n B_n(\nu,T_m),\\ B_n(\nu,T_m) &= \frac{1}{n!}\left(T^n\frac{\partial^n I_m(\nu,T)}{\partial T^n}\right)\Bigg|_{T=T_m},\\ \gamma_n &= \left\langle\left(\frac{\Delta T}{T_m}\right)^n\right\rangle,\quad n=2,\ldots,N,\quad \gamma_0=1\,,\quad \gamma_1=0\,.\end{aligned} \tag{9}$$

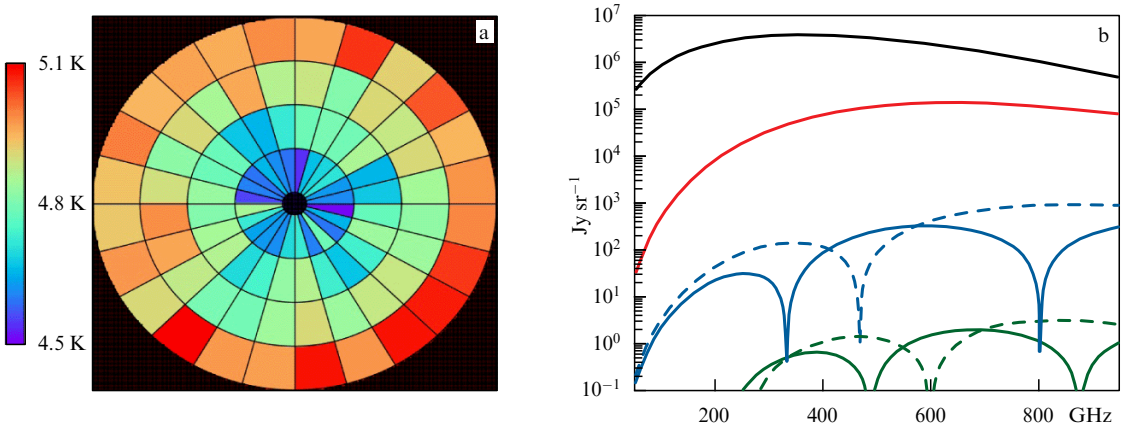

Figure 6. (Color online.) (a) Temperature distribution across the primary mirror surface. Ninety-six panels have different temperatures increasing from the center to the edges by 0.5 K. (b) The mirror contribution to the total signal. Signal decomposition moments $\gamma_n B_n$: $n=0$ (black), $n=2$ (red), $n=3,4$ (blue), $n=5,6$ (green). The dashed lines indicate odd moments ($n=3,5$).

The coefficients γ_n should be found from the separation of the components from observations. We obtain their approximate estimate by considering that the temperature of the mirror panels can vary from the center to the edge by approximately 0.5 K:

$$\gamma_n = \frac{1}{2(n+1)}\left(\frac{0.5\ \mathrm{K}}{T_m}\right)^n, \quad n = 2,4,6,\ldots$$
$$\gamma_n = \frac{1}{\sqrt{(4n+2)N_{\mathrm{pan}}}}\left(\frac{0.5\ \mathrm{K}}{T_m}\right)^n, \quad n = 3,5,\ldots, \tag{10}$$

where $N_{\mathrm{pan}} = 96$. The spectral form of the decomposition moments and their expected amplitudes are shown in Fig. 6.

2.2 Cosmological tasks for the next level

2.2.1 Determination of the Hubble constant. Measurement of the Hubble constant, which is the critical parameter characterizing the current rate of the Universe's expansion, age, and critical density, is one of the fundamental cosmological problems. In the last few years, this problem has attracted a great deal of interest due to a 4.4σ discrepancy between the Hubble constant inferred from the Planck CMB observations [49] and the value obtained through local measurements using the 'distance ladder' from the Hubble Space Telescope observations [50]. In particular, the value of H_0 is 67.4 ± 0.5 km s^{-1} Mpc^{-1} as extrapolated from the Planck CMB measurements, assuming the ΛCDM-model [49], and 74.03 ± 1.42 km s^{-1} Mpc^{-1} as obtained from SH0ES (The Supernovae, H0, for the Equation of State of Dark Energy) observations [50]. At the same time, data on baryon acoustic oscillations jointly with type Ia supernova observations suggest a Hubble constant value close to that obtained by the Planck observatory, $H_0 = 67.3 \pm 1.0$ km s^{-1} Mpc^{-1} [51]. Notably, the CMB experiments and observations of baryon acoustic oscillations now enable distance scale measurements with a 1% accuracy; however, one should bear in mind that these measurements are model dependent.

The local value of the Hubble constant reported in [50] is measured with an accuracy of better than 2%. Such a high precision was achieved due to observations of long-period cepheids and DEBs (Detached Eclipsing Binaries) in the Large Magellanic Cloud. These cepheids were used to calibrate the distance to variable cepheids in galaxies with recent type Ia supernovae. High precision has also been provided by observing masers in the galaxy NGC4258 and parallax measurements of Milky Way cepheids.

In the Carnegie-Chicago Hubble Program, instead of cepheids, observations of the brightest giant branch stars (TRGB) were used to obtain $H_0 = 69.8 \pm 0.8(\pm 1.1\%\ \mathrm{stat.}) \pm 1.7(\pm 2.4\%\ \mathrm{syst.})$ km s^{-1} Mpc^{-1} [52], which at a 1.2σ confidence level agrees with the Planck results, and at a 1.7σ level, with the SH0ES observations, i.e, it lies between these values.

Values of H_0 as inferred from megamaser observations are also close to the Planck results but have larger errors. For example, paper [53] reports the value 66.0 ± 6.0 km s^{-1} Mpc^{-1}, paper [54] — 68.9 ± 7.1 km s^{-1} Mpc^{-1}, and paper [55] — 73^{+26}_{-22} km s^{-1} Mpc^{-1}.

Thus, observations suggest that the Hubble constant in the local and distant Universe is likely to be different. Independent measurements of H_0 should be utilized to confirm this difference. One such method, first suggested in [56], proposes to measure the so-called time-delay distance between lensed images of a bright variable source, for example, a quasar or a supernova. The time-delay distance is inversely proportional to the Hubble constant; therefore, it can constrain both the Hubble constant and other cosmological parameters. However, time-delay between images alone is insufficient to determine H_0 with reasonable accuracy (see, for example, [57]). Paper [58] showed that one strong lensing event supplemented with measured time-delay and additional observational data enables determining the Hubble constant with about 7–8% accuracy. Presently, based on six lensed quasars, the Hubble constant is measured to be $73.3^{+1.7}_{-1.8}$ km s^{-1} Mpc^{-1} with an accuracy of 2.4% [59]. This means that the discrepancy with the Planck observations is $3.1\,\sigma$. When combining this finding with results in [50], the difference between H_0 in the early and late Universe increases to $5.3\,\sigma$ (Fig. 7).

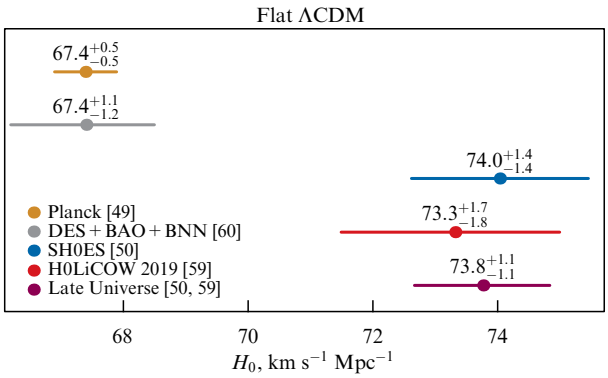

Figure 7. (Color online.) Hubble constant estimates in the early and late Universe assuming the ΛCDM model. In the early Universe: Planck observatory results [49] (in orange) and the combination of data from galaxy clusters and weak lensing, baryon acoustic oscillations, and nucleosynthesis [60] (in grey). In the late Universe: SH0ES results [50] (in blue), H0LiCOW (H0 Lenses in COSMOGRAIL's Wellspring; COSMOGRAIL — COSmological MOnitoring of GRAvitational Lenses) results [59] (in red) and their combination (in purple). (Figure from paper [59].)

If the reason for different H_0 at different times is not due to systematic errors, the ΛCDM model needs to be modified. For example, one should consider dynamical dark energy and dark matter, a nonzero curvature, a large number of effective relativistic particles, etc. (see, for example, the discussion in [61]). A 1% accuracy is required to solve the issue of different values in various experiments and get information about dark energy properties. As shown in some papers (see, for example, [59] and references therein), detailed observations of about 40 gravitational lenses, including time-delay measurements between images, are required to achieve such precision.

Data used to determine the Hubble constant have been obtained in the optical, near-IR, and radio bands. Far-IR and sub-millimeter observations by Millimetron can provide additional information to solve this problem. The telescope's angular resolution will be about 1–2 arcseconds at the shortest wavelengths, and the broadband photometry sensitivity can reach 0.01 mJy [3]. The principal goal is to discover new gravitationally lensed systems with multiple images that can be used to determine the Hubble constant. The number of sources that Millimetron can potentially observe was estimated in detail in [62]. This paper also gives the number of lensed sources, their distribution on redshift, and the magnification. Here, we present some estimates and conclusions from this paper.

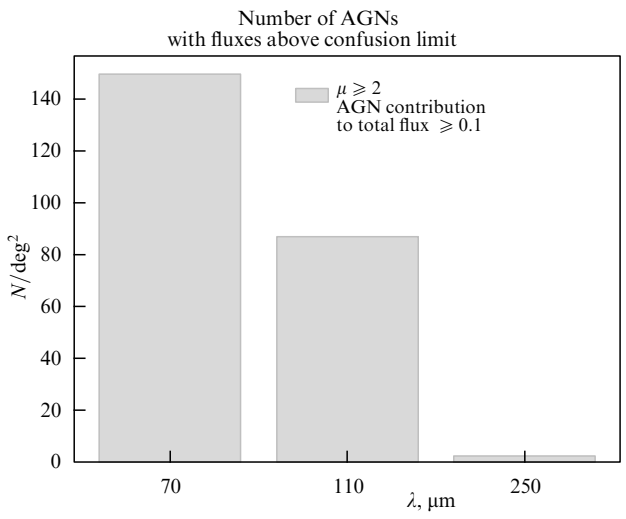

Figure 8. Number of lensed AGNs with the magnification $\mu \geqslant 2$ per square degree and fluxes above the 'confusion limit' at 70–250 μm. (Figure from paper [62].)

The number of lensed active galactic nuclei (AGNs) with magnification $\mu \geqslant 2$ at 70–250 μm with fluxes above the 'confusion limit' is shown by the histogram in Fig. 8. The figure suggests that we can expect about 140 lensed AGNs with $\mu \geqslant 2$ by observing a one-square-degree area at 70–250 μm. However, not all of these lensed AGNs will have an angular distance between images that can be measured by the short-wavelength CCD (SWCCD) of the Millimetron Space Observatory. As follows from [62], the maximum of the lens mass distribution is at $\sim 10^{11} M_\odot$. The angular separation between images will be about one arcsecond for a lens with such mass, comparable to the SWCCD angular resolution. In about 15% of detected lensed AGNs, image separation will exceed two arcseconds and can be utilized to determine H_0. At least a two-square-degree sky area should be scanned to detect images of approximately 40 such AGNs.

Thanks to the record sensitivity of the Millimetron instruments, the expected scanning rate will be 0.005 square degrees per minute at the shortest wavelength. It will be an order of magnitude higher at 100–250 μm. This will enable us to scan two square degrees in about seven hours at the shortest wavelength and an order of magnitude faster at longer wavelengths.

Note that photometric data should be supplemented with spectroscopic observations that will enable AGN identification and the redshift determination of their images required for the H_0 measurement. Due to gravitational lensing achromaticity, the multiple-lensed AGNs found in the Millimetron survey can be further investigated at other wavelengths by ground-based telescopes with higher sensitivity and angular resolution. For some sources with small angular separation between images, subsequent series of repeated photometric Millimetron observations can estimate the time delay between images. Nevertheless, this task requires modeling the specific experiment that can be postponed until the next stages of preparation of a detailed scientific program, taking into account the mission planning strategy and tactics.

Besides searching for gravitationally lensed AGNs in small sky area surveys, it is worth observing multiple-lensed sources with measured time delays between images found at other wavelengths but without information about the lens galaxy mostly shining in the far IR band. Millimetron will be able to take photometric images of such galaxy lenses and determine their redshift.

2.2.2 Early galaxies: first stars and galaxies. The beginning of stellar nucleosynthesis, including the formation of the first stars and galaxies, reionization of the Universe by hard radiation from the first stars, and its enrichment by heavy elements is a significant problem in post-recombination cosmology. The beginning of stellar nucleosynthesis determined the face of the modern Universe.

Early galaxies probably reionized and heated the intergalactic gas at redshifts $z \sim 7-12$ (see, for example, the discussion in paper [63]). The gas thermodynamics in the early Universe are radically different from those at later times, starting with moderate redshifts $z \leqslant 5$. This is related to the fact that the chemical composition of the early Universe included only $\sim 75\%$ hydrogen and $\sim 25\%$ helium with their isotopes and an insignificant amount of lithium. Gas cooling in these conditions is mediated by the formation of hydrogen molecules H_2, which, in turn, depends on the electron density.

Two processes directly determine the formation of the first stars in galaxies. First of all, there is the appearance of sufficiently massive dark matter halos depending on the perturbation amplitude on the corresponding scales. Second, there is the cooling of baryons compressed inside these massive dark matter halos. The gas cooling results in the formation of the first stars, initiating stellar nucleosynthesis and metal production, leading to reionization and radiation heating of the intergalactic gas at redshifts $z \sim 10-5$ (see, for example, [64]).

Modern theoretical models of the first galaxy formation and observations of the most distant galaxies [65–68] suggest that these galaxies

(a) have a moderate dynamical mass $M_{\mathrm{dyn}} \sim (10^6-10^{10}) M_\odot$;

(b) have low metallicity ($Z \leqslant 10^{-3} Z_\odot$);

(c) likely harbor supermassive stars with $M_{\mathrm{star}} \sim (50-10^3) M_\odot$.

The mass, luminosity, and metallicity of early galaxies are similar to those of the Milky Way and Andromeda satellites. It is known that active metal formation in the local Universe is possible both immediately after galaxy formation and in the course of later evolution [69]. Presently, such information is unavailable for galaxies at high redshifts. Nevertheless, metal formation in the early galaxies can be probed only directly from observations.

Observations by the Herschel telescope [70, 71] clarified massive galaxy formation at redshifts $z \leqslant 3$. These observations revealed an essential role of galaxy mergers enhancing the creation of stars, metals, and dust. Several galaxies discovered by the Herschel telescope and later studied with ALMA were identified as early galaxies [69]. For example, for the galaxy T0346-52 lensed by a galaxy cluster, the redshift $z = 5.7$ and far IR luminosity $L \sim 3.7 \times 10^{13} L_\odot$ were measured [72].

Possible 'targets' for investigating early star formation in the Universe in the far IR and submillimeter range include galaxies from ultra-deep Hubble fields. In particular, one such galaxy is GN-z11 at redshift $z = 11.1$ [9]. Apparently, it is one of the first galaxies. It is observed at the beginning of reionization (the age of the Universe for $z = 11$ is only 400 Myr) and still has, for that time, an excessive luminos-

ity: $L \sim 3 \times 10^{10} L_{\odot}$. Its luminosity is three times as high as that of a typical galaxy $\sim 10^{10} L_{\odot}$ at redshifts $z \sim 6-8$ [73]. The discovery of a galaxy similar to GN-z11 can be either a lucky incident or suggest that the luminosity function of early galaxies differs from the standard Press–Schechter law. Presently, 13 galaxies with redshifts $z > 8.5$ are known (see, for example, [74, 75]). Possibly, $z = 11$ is already close to the beginning of stellar nucleosynthesis, because, on time scales of ~ 200 Myr from $z \simeq 12$ to $z \simeq 8$, the effective star formation rate increases by an order of magnitude from $\rho_{\rm SFR} \sim 2 \times 10^{-4} M_{\odot}$ yr^{-1} Mpc^{-3} to $\rho_{\rm SFR} \sim 3 \times 10^{-3} M_{\odot}$ yr^{-1} Mpc^{-3}. By extrapolating this dependence to earlier epochs, at redshifts $z \simeq 15$, the star formation rate can be $\rho_{\rm SFR} \sim 10^{-5} M_{\odot}$ yr^{-1} Mpc^{-3} (see Fig. 4 in [75]).

Note that studying the beginning of stellar nucleosynthesis is one of the priority tasks of the James Webb Space Telescope (JWST). The JWST, equipped with the MIRI (Mid-InfraRed Instrument, photometric bands 5.6–25.5 μm), will be able to discover sources with fluxes $F_{\nu} \sim 10^{-6}$ Jy [76] corresponding to the galactic luminosity $L_{\rm H\alpha} \sim 10^{40}$ erg s^{-1} in the Hα-line [5] at redshift $z \sim 3$. A similar galaxy at redshift $z \sim 10$ will radiate in the Paschen and Brackett series (laboratory wavelengths $\lambda \leqslant 1.8556$ μm and $\lambda \leqslant 4.0523$ μm, respectively) about one fifth of what they emit in the Hα line. At wavelengths of ~ 30 μm, this corresponds to a flux of $F_{\nu} \sim 0.1$–0.3 μJy, close to the sensitivity limit of Millimetron. Thus, this observatory will be able to discover galaxies with a star formation of $\sim 0.15 M_{\odot}$ yr^{-1} at redshifts $z \simeq 10$. Therefore, the capabilities of Millimetron to measure the star formation rate in galaxies may exceed those of the JWST.

2.2.3 Early galaxies: Ly-α emitters (LAE). These are extremely bright galaxies emitting most of their power in the Lyman-alpha (Ly-α) line of atomic hydrogen due to scattering of the UV emission from the central source (quasar, galaxy nucleus, active star formation region) in a neutral or weakly ionized hydrogen envelope. Here, the luminosity can be as high as $L_{\rm Ly\alpha} \sim 10^{11} L_{\odot}$. Ly-α emitters are considered the most plausible class of the first galaxies. They are found within the redshift interval from $z \sim 2$ to $z \gtrsim 8$ [78]. Therefore, they are important sources for Universe reionization and tools to probe reionization [79–81].

The number of LAEs beyond $z \simeq 6.6$ drastically decreases. The LAE space density scales as $\rho_{\rm Ly\alpha} \propto (1+z)^{-\beta}$, where $\beta \simeq 5$ in the redshift interval $z = 5.5-6.6$ and $\beta \simeq 20$ at $z > 6.6$. Here, the number of UV continuum sources up to redshift $z \simeq 8$ decreases more slowly, with the slope $\beta \simeq 3$, and only at $z \gtrsim 8$ starts falling sharply with $\beta \simeq 9.6$ [82]. This is related to increased mean hydrogen density at higher redshifts and the corresponding Ly-α absorption. The recent narrow-band LAE survey [83] showed that the fraction of atomic hydrogen in the Universe at $z \sim 7$ is $\chi_{\rm HI} \sim 0.2-0.4$; for earlier epochs, $z = 7-8$, the estimate is $\chi_{\rm HI} \sim 0.3-0.5$ [84, 85]. In such conditions, the Ly-α line central optical depth reaches $\tau_{\alpha} \gtrsim 10^8$ on a scale of ~ 1 Mpc, which at $z \sim 7$ corresponds to $\Delta z = 0.25$. Therefore, Ly-α emission from an LAE galaxy will be strongly suppressed.

One can assume that galaxies with effective star formation, which in the reionized Universe at $z < 7$ appear as LAEs, can exist beyond the reionization threshold at $z > 7$ [74, 75]. Besides the sharp decrease in the number of LAEs above the reionization threshold, a close to primordial chemical abundance of LAEs and an excess of massive stars in the stellar mass function (see below) can be indirect evidence of their existence.

[5] The equivalent star formation rate assuming the standard initial mass function is SFR $= 0.055 M_{\odot}$ yr^{-1} [77].

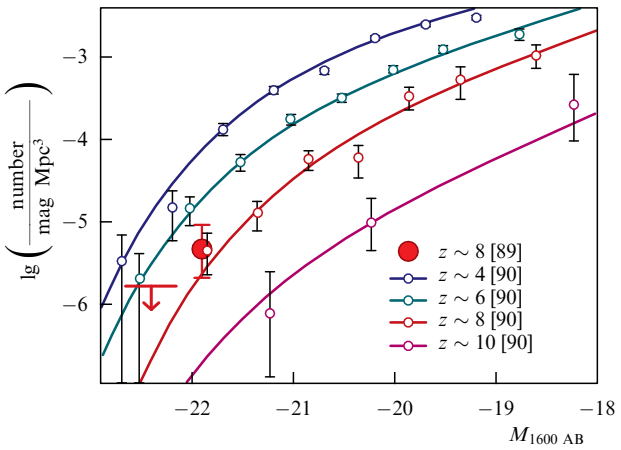

Figure 9. Luminosity function of the brightest galaxies from the CANDELS HST program jointly with Spitzer/IRAC [89, 90] as a function of the stellar magnitude in the HST F160W band (mean wavelength $\lambda = 15436.3$ Å) of the AB photometric system [91]. (Figure from paper [87].)

Such an assumption prods us to search for possibilities of discovering LAE predecessors in the far IR. One option is related to Balmer hydrogen line observations at wavelengths $\lambda \geqslant 6365(1+z)$ Å and will soon be realized by the JWST [86–88]. However, beyond $z > 10$, the JWST sensitivity at $\lambda > 6$ μm (~ 10 μJy for an exposure time of 10,000 s) is insufficient to detect the Balmer spectrum. As noted above, observations in the Paschen, Brackett, and Pfund hydrogen series available for Millimetron (both at THz frequencies and with ten-μJy sensitivity) may be more advantageous. Observations of such star formation regions ('hidden' Ly-α emitters) can be crucial to solving two fundamental questions: the initial stellar nucleosynthesis in the Universe and the dynamics of early large-scale structure formation, because LAEs are predominantly found inside cosmic structure filaments.

The number of these objects at redshifts $z \gtrsim 8$ can be estimated from CANDELS HST (Cosmic Assembly Near-infrared Deep Extragalactic Legacy Survey of the Hubble Space Telescope) and Spitzer/IRAC (InfraRed Array Camera) joint observations [89, 90] (see Fig. 9). For example, at $z = 8$ in a field within the solid angle $\Delta\Omega \sim (\theta = 2')^2$, one can expect to discover one object with luminosity $L \sim 10^{10} L_{\odot}$. A field with $\Delta\Omega \sim (\theta = 2^{\circ})^2$ is needed to detect an object with the same luminosity at $z = 10$. A crude estimate of the expected fluxes in the Paα (rest-frame wavelength 1.875 μm), Brα (4.05 μm), and Pfα (7.46 μm) lines is $\sim 10-30$ μJy, which exceeds the Millimetron sensitivity threshold for middle-resolution spectroscopy. Therefore, MSO deep surveys can be essential to discover the first LAE galaxies and understand their role in the reionization dynamics. Note that these objects are being studied in detail in the optical [90, 92, 93], infrared, and radio [94, 95] ranges.

Present-day observations suggest that Ly-α emitters comprise at least two different classes of objects. On the one hand, there are bright, massive objects with luminosity $L \sim 10^{10}-10^{12} L_{\odot}$ — quasars and massive galactic nuclei embedded in an extended neutral hydrogen envelope [96].

Table 3. LAE properties derived from ALMA observations in the CII and OIII lines.

Object	z	$M_{\rm dyn}/M_\odot$, 10^{10}	$M_{\rm star}/M_\odot$, 10^{10}	$M_{\rm dust}/M_\odot$, 10^9	Reference
MACS0647 – JD	11		0.13 ± 0.01		[104]
MACS1149 – JD1	9.11	0.4 ± 0.3	0.1	5.3×10^{-4}	[106]
A2744 – YD4	8.382		0.2	6×10^{-3}	[114]
MACS0416,1 – 2403	8.312		0.3	4×10^{-3}	[115]
B14 – 65666	7.15	8.8 ± 2		9×10^{-3}	[116]
SPT – SJ031132 – 5823,4W	6.9		3.5 ± 1.5	2.5 ± 1.6	[117]
SPT – SJ031132 – 5823,4E	6.9		3.5 ± 1.5	0.4 ± 0.2	[117]
COS – 3018555981	6.81	1 ± 0.2			[118]
COS – 2987030247	6.85	0.4 ± 0.6			[118]

On the other hand, LAEs include less massive and fainter galaxies with active star formation that can be considered predecessors of galaxies like the Magellanic Clouds and other satellites of the Milky Way and Andromeda galaxies. Here, of particular interest are observations of galactic protoclusters at high redshifts $z \sim 6-7$ [97]. Interestingly, at the end of reionization at $z \sim 10-7$, the number and density of the brightest galaxies become comparable to that of galaxy clusters ($n \leqslant 10^{-6}$ Mpc^{-3}) [93]. Paper [96] reviews the observed and model properties of such protoclusters and clusters. Papers [98–100] considered the properties, dynamics, and emission of the surrounding gas.

The presence of metal and dust in HI shells leads to significant infrared, submillimeter, and millimeter radiation, in particular, in (redshifted) carbon CII (158 μm) and oxygen OIII (88 μm) lines. In recent years, such observations have been performed with the ALMA telescope (see, for example, [90, 101–105]. Observations of galaxies at high redshifts $z \sim 9-15$ were also considered in [106].

Distant LAEs can be discovered in observations of massive galaxy clusters that serve as gravitational lenses for the LAEs behind them. For example, papers [107–109] report the discovery of 452 LAE candidates with star formation rate $1 \leqslant {\rm SFR} < 200\,M_\odot$ yr^{-1}. For instance, lensed LAEs were also found in observations of the galaxy cluster $MS1358+62$ at $z = 4.92$ [110] and $A1689-zD1$ at $z = 7.5$ [111]. Observations of LAEs at $z \sim 1-4$ in the CII, OIII, and other lines are also reported in papers [103, 112, 113]. They enabled the determination of the stellar mass for 130 bright objects from the Spitzer/IPAC catalogue ($\langle M_{\rm star}\rangle = 3\times10^{11}M_\odot$) and fainter objects ($\langle M_{\rm star}\rangle = 10^8 M_\odot$) and the estimation of the star formation rate $\langle {\rm SFR}\rangle \simeq 1.4 M_\odot$ yr^{-1} and the dynamical mass $\langle M_{\rm dyn}\rangle = (6\pm2)\times 10^{10}M_\odot$. For several LAEs, the stellar, dust, and dynamical mass estimates obtained from the ALMA observations are presented in Table 3.

For example, one of the objects from Table 3 is the galaxy $B14-65666$ [116] at redshift $z = 7.15$ with the total luminosity $L_{\rm tot} \approx 10^{12}L_\odot$, Ly$_\alpha$ luminosity $L_\alpha \approx (6.8\pm1.3)\times10^8 L_\odot$, OIII luminosity $L_{\rm OIII} = (34.4\pm4.1)\times10^8 L_\odot$, and CII luminosity $L_{\rm CII} = (11.0\pm1.4)\times10^8 L_\odot$. In this galaxy, CII and OIII emissions are observed in two components shifted by ~ 200 km s^{-1}, suggesting that the observed active star formation there is due to the merging of two less massive galaxies.

Thus, observations of massive galaxy clusters that are gravitational lenses for background objects are invaluable for discovering distant LAEs. For example, paper [108] lists several dozen clusters that can be used to observe LAEs by the Millimetron observatory.

2.2.4 Dusty galaxies: DSFGs and LIRGs. Dusty star-forming galaxies (DSFGs) with a high star-formation rate are a class of very bright infrared galaxies with star formation rate ${\rm SFR} \sim 10^3 M_\odot$ yr^{-1} kpc^{-2} (see Fig. 44 in [119]). When rescaled to our Galaxy, it corresponds to a star formation rate of $10^5 M_\odot$ yr^{-1}, five orders of magnitude higher than the actual value. Due to the high SFR, DSFGs are observed at redshifts $z \gtrsim 7$ [119]. Most of these galaxies harbor dust-obscured nuclei with supermassive black holes that often serve as supplementary or even principal power sources. Nevertheless, in these galaxies, star formation plays an essential role by supplying dust. Luminous infrared galaxies first discovered in the local Universe ($z < 1$) and later found at high redshifts may also be in this class.

Luminous infrared galaxies (LIRGs)[6] with infrared emission exceeding the optical one [120] were discovered at the dawn of infrared astronomy. The spectral energy distribution of normal galaxies and galaxies with an excess of IR emission (ULIRGs) is presented in Fig. 10. The spectral dominance of IR emission is caused by a large amount of dust absorbing and reprocessing optical into IR emission. The dust heating sources mostly determine the diversity of their properties. The LIRG to ELIRG transition is likely associated with an increasing contribution from the galactic nucleus powered by a central supermassive black hole. The excessive amount of dust in these galaxies makes them optically opaque and difficult to detect by optical and ultraviolet telescopes. The nearby galaxy Arp220 ($\simeq 87$ Mpc; see Section 3.4 for more detail) provides a typical example of ULIRGs. The luminosity of ELIRGs reaches $L \sim 3.5\times10^{14}L_\odot$, for instance, W2246-0526 at $z = 4.59$ with the black hole mass $M_\bullet \sim 10^{10}M_\odot$ [122]. A large part of (if not most) LIRGs is opaque to optical and apparently to X-ray emission with a hydrogen column density above the Compton limit $N({\rm H}) > 10^{25}$ cm^{-1} [122, 123].

Both DSFGs and LIRGs are exciting objects for Millimetron. The high optical depth ($N({\rm H}) > 10^{25}$ cm^{-2}) makes them observable only in the far IR hand and submillimeter bands fully covered by Millimetron. Here, the problems that can be addressed exclusively by Millimetron include 1) the nature of supermassive black holes with a billion solar masses found at redshifts $z > 4$, i.e., long before the global star formation burst in the Universe at $z \sim 2$, 2) the mutual influence of black hole mass growth and the stellar mass of the entire galaxy, 3) the possible effect of the galaxy's

[6] The luminosity of these galaxies is $L = 10^{11}-10^{12}L_\odot$. Galaxies with IR-luminosity one, two, and three orders of magnitude higher are referred to as ULIRGs (ultra-), HyLIRGs (hyper-), and ELIRGs (extreme-), respectively.

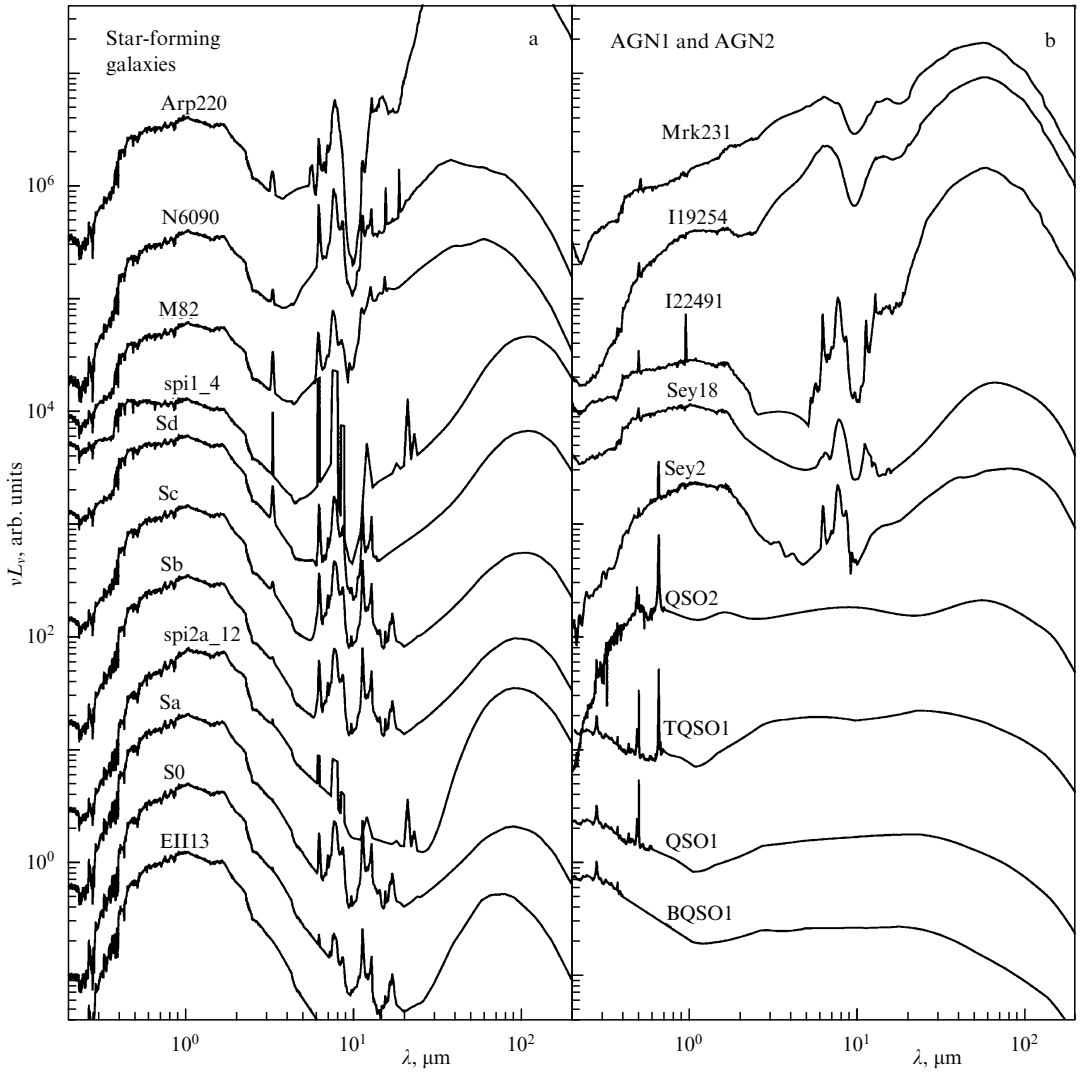

Figure 10. Spectral energy distribution νL_ν as a function of λ for galaxies of various morphological types and galaxies with IR excess. (a) From bottom to top: elliptical, spiral, and star-forming (IR-excess) galaxies. (b) Active galactic nuclei. From bottom to top: 1st and 2nd type AGNs. In 2nd type AGNs, the energy sources are screened by dust. When passing from dust-poor elliptical galaxies to spiral and irregular ones and active galactic nuclei, the IR emission gradually dominates over the optical one (in LIRGs). (Figure from SWIRE Template Library described in [124] (see also http://www.iasf-milano.inaf.it/~polletta/templates/swire-templates.html).)

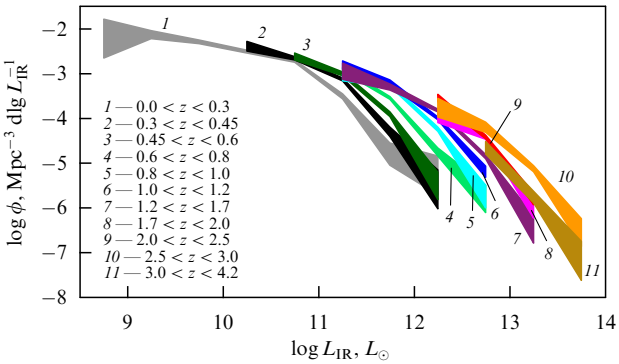

Figure 11. (Color online.) Luminosity function of LIRGs in the redshift interval $z = 0-4.2$ [124].

dynamical mass on the central black hole mass growth that appears as a correlation between the central black hole mass and velocity dispersion in galaxies, 4) dust production and its mass growth before the global star formation burst, etc.

The enormous luminosity of LIRGs renders them observable up to redshifts $z \gtrsim 4$ (Fig. 11). Clearly, LIRGs are brighter at high redshifts. Moreover, as noted in [124], their number at high redshifts is underestimated due to selection effects related to the dominance of galaxies with photometric redshifts.

2.2.5 First supermassive black holes. Observations in recent years have revealed a large number of SMBHs (more than 200) with masses $M_\bullet \gtrsim 10^9 M_\odot$ at redshifts $z \gtrsim 6$ [125–129], with four of them with $z > 7$ [130–134]. This means that, during the first ~ 700 Myr in the Universe, BHs with masses $M_\bullet \sim 10^9 M_\odot$ already existed. How many such objects existed at these early times? How far in the past can they be found?

Most of the galaxies in the local Universe contain central supermassive BHs. The larger the galactic bulge mass (see, for example, [135–138]) and dark halo mass [139], the larger the central BH mass. It is natural to assume that the innermost parts of early galaxies up to

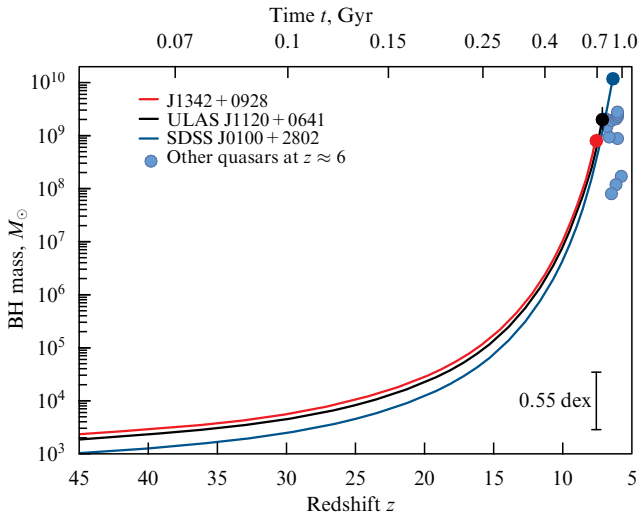

Figure 12. Black hole mass growth with luminosity sustained at the Eddington level and 10% radiation efficiency starting with a BH seed with $M_{\rm seed} = 1000M_\odot$ (lower curve), $M_{\rm seed} \simeq 2000M_\odot$ (middle curve), $M_{\rm seed} = 2500M_\odot$ (upper curve) at $z_0 = 45$. The BH seed masses at $z = 45$ are such, so as to produce the SMBH masses inferred from observations of J1342+0928 ($M_\bullet = 7.8 \times 10^8 M_\odot$ at $z = 7.54$) [131], ULAS (UKIDSS Large Area Survey, UKIDSS — UKIRT Infrared Deep Survey, UKIRT — United Kingdom Infrared Telescope) J1120_0641 ($M_\bullet = 2.0 \times 10^9 M_\odot$ at $z = 7.09$) [130], SDSS (Sloan Digital Sky Survey) J0100+2802 ($M_\bullet = 1.2 \times 10^{10} M_\odot$ at $z = 6.33$) [142].

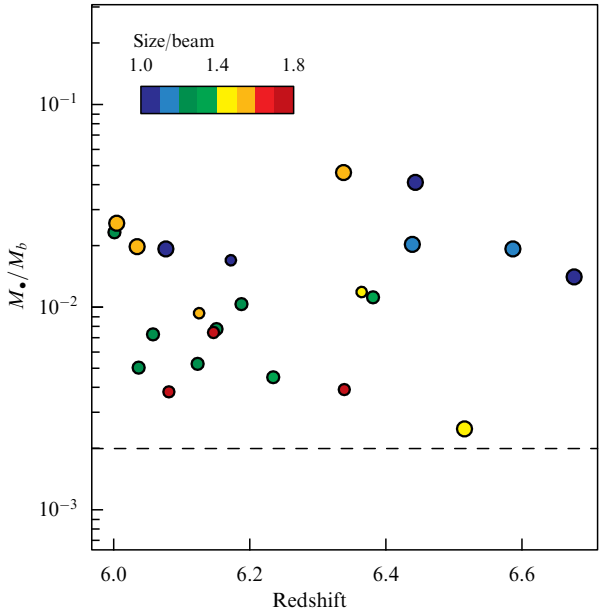

Figure 13. (Color online.) Ratio of the SMBH to the host galaxy baryonic mass at redshifts $z \sim 6$. The horizontal dashed line shows the mean ratio $M_\bullet/M_b$ at present, $z \sim 0$. (Plot from paper [141].)

$z \simeq 11$ (at the age of the Universe of about 400 Myr) [9] can also harbor SMBHs. [7]

Presently, there is no consistent understanding of the emergence of SMBHs at high redshifts ($z \gtrsim 7$). The main problem is that the accretion rate onto an SMBH should either significantly exceed the Eddington limit if its growth started at $z \lesssim 10$ or be kept close to the Eddington limit if the mass increase started at $z \simeq 45-20$ [131] (Fig. 12). Here, however, during the last 100–200 Myr, the accretion rate should be sustained at $\dot{M} \gtrsim 15 M_\odot$ per year, which requires exclusive conditions (see, e.g., [130, 131]). It may be important that the 'BH mass — galaxy mass' relation for SMBHs at $z = 6-6.7$ is systematically one to one and a half orders of magnitude higher than for BHs at later times (Fig. 13). However, observational selection effects cannot be ruled out, because BHs with a lower mass and a smaller BH mass to galaxy mass ratio turn out to be below the detection threshold.

The problem with the optical detection of such black holes at $z > 7$ is related to incomplete ionization of the Universe and that the transmission factor for Lyman quanta is small (see the review of the problem in [143]). Observations of quasar J1342+0928 at redshift 7.5 [131] support this idea. In these conditions, the IR range is the most suitable for detecting such growing SMBHs: the Balmer lines redshifted to the near IR region can be measured by the JWST, and the Paschen and Brackett lines are redshifted to the far IR and submillimeter region. Conservatively assuming the fraction of a growing quasar's total luminosity in these line series to be 0.1% and shifting the quasar J1342+0928 to redshift $z = 20$ with an order of magnitude smaller luminosity, we find the flux $F_\nu \sim 10^{-3}$ Jy at ~ 5 THz, available for Millimetron.

Here, it is essential to identify the signal from such an object, i.e., reliably conclude that the signal indeed comes from a growing supermassive black hole (a quasar 'seed'). To this end, paper [144] calculated the emission spectrum from an 'obese black hole galaxy' (OBG) [8] containing a growing massive black hole, a lot of gas (with primordial chemical abundance), and a stellar population that was insignificant in mass or absent. The OBG model concordantly describes the entire evolution of early galaxies in which SMBHs can arise at redshifts $z \gtrsim 8-10$. Therefore, this model now seems to be the most likely one [87, 146, 147]. It turns out that, depending on the ratio of BH mass and gas mass in the galaxy, a break in the infrared spectrum from the black hole and hot surrounding gas arises. This break is due to the transition from the Rayleigh–Jeans quasi-blackbody spectrum $\propto \nu^2$ from the outer parts of an accretion disk [148] to a bremsstrahlung spectrum $\propto \nu^{-0.118}$ from hot gas, as illustrated in Fig. 14. The transition frequency and the corresponding luminosity are determined by the BH mass and the emitting gas mass. The hydrogen and helium spectral lines enable measuring the source redshift.

The expected fluxes from growing black holes at redshifts $z = 10$ are shown in Fig. 15. It is seen that galaxies with gas mass $M_{\rm g} \gtrsim 10^{10} M_\odot$ produce fluxes at a spectral break frequency detectable by Millimetron. Estimates in [144] show that the number of such sources with BH masses $M_\bullet = 10^7 - 10^8 M_\odot$ at redshifts $z = 10-11$ can be as high as $N \sim 0.03-2$ per square minute. At least one such object can fall within the Millimetron aperture, $6' \times 6'$, at the lower sensitivity limit.

This means that the scientific program of MSO allows discovering SMBHs in the early Universe. However, considering the tiny detection probability even in systematic sky scans, we are left with the only possibility of searching for

[7] For estimates, one can use the relation $M_\bullet = 0.002 M_{\rm dyn}$, where $M_{\rm dyn}$ is the total mass of the galaxy [138, 140, 141]. The existing data could enable us to estimate the BH mass in the galaxy GN-z11 [9] as $\sim 10^7 M_\odot$. Here, however, one should bear in mind the dispersion $\Delta M_\bullet$ for a given stellar mass by more than two orders of magnitude (see, for example, Fig. 9b in [140]).

[8] First described in [145].

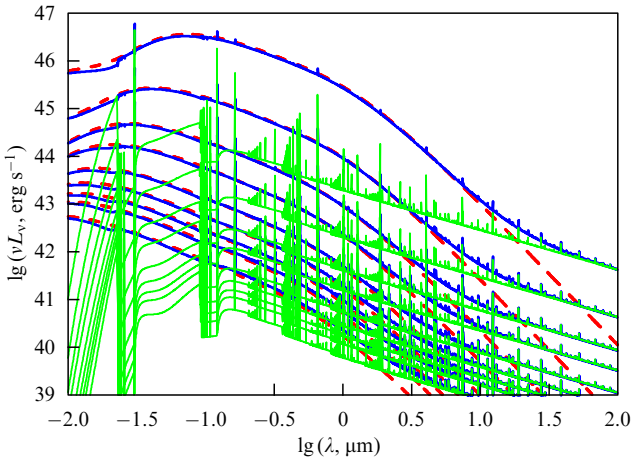

Figure 14. (Color online.) Total OBG spectrum (blue lines). The spectrum from the accretion disk around a growing black hole and ionized circumgalactic gas (red dashed lines and green lines, respectively). The spectrum is shown in the reference frame of the black hole. The black hole mass increases from $10^5 M_\odot$ at $z = 16$ to $9 \times 10^8 M_\odot$ at $z = 8$. The curves are plotted for black hole masses in the redshift range from $z = 16$ to $z = 8$ with $\Delta z = 1$ intervals from bottom to top (corresponding to points in Fig. 12). (Figure from paper [144].)

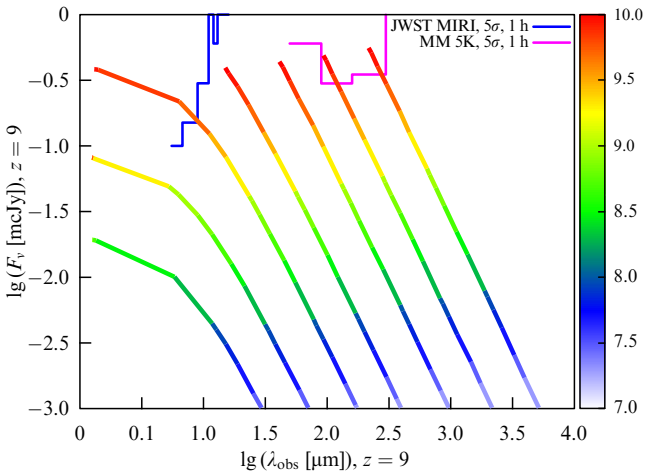

Figure 15. (Color online.) Expected spectral flux from a growing black hole at $z = 9$ and ionized surrounding gas near that spectral break ν_k from low-resolution ($R = 100$) spectral observations for the black hole mass $M_\bullet$: 10^5, $10^{5.5}$, 10^6, $10^{6.5}$, 10^7, $10^{7.5}$, $10^8 M_\odot$ (from left to right). The line color shows the gas mass in the OBG host galaxy. The blue and violet lines indicate the detection threshold in a one-hour exposure with the JWST and Millimetron telescope. (Plot from paper [144].)

their appearances in remote galaxies discovered in ultra-deep Hubble Space Telescope surveys (see [74, 75]). The rest-frame luminosity of these galaxies is $L \sim 10^{10} L_\odot$. At redshifts $z > 7$, the expected central SMBH mass is of the order of $M_\bullet \sim 3 \times 10^7 M_\odot$ with the Eddington luminosity $L_E \sim 10^{11} L_\odot$ and submillimeter fluxes of about one micro Jy, available for Millimetron for an exposure time of about 3–10 hours. Considering that, according to the CANDELS survey [149], the number of galaxies beyond $z > 9$ is about one every 47 square arcseconds, i.e., about 0.8 within the Millimetron field of view, the probability of detecting at least one SMBH is high.[9] The discovery of BHs in galaxies at $z > 8$ and their mass measurement will shed light on SMBH formation in the reionization epoch and their rapid mass growth dynamics, a key open issue in modern cosmology. Millimetron can play a crucial role in measuring low-frequency emission from SMBH surroundings (the Paschen and Brackett hydrogen lines), for which the pre-reionization intergalactic medium is transparent.

[9] Even nondetection can be significant from the point of view of understanding the early evolution of galaxies and their SMBHs.

3. Supermassive objects in the Universe

Exploring space-time and matter properties close to the event horizon of black holes — black-hole 'microscopy' — is one of the fundamental problems in modern science. The existence of black holes — compact relativistic objects predicted by K Schwarzschild from the exact solution of the Einstein equations [150] — has been known for about half a century, since the discovery of the compact X-ray source Cyg X-1. However, this knowledge has been based on indirect data on high X-ray luminosity and rapid variability of the source (see the discussion in [151, 152]). Direct observations are difficult, because the size of black holes, i.e., their event horizon radius, is tiny. Therefore, their 'microscopy' is possible only for SMBHs using submillimeter very long baseline interferometry (VLBI) to provide the necessary angular resolution. Such observations have been carried out in the last few years, but a reliable result was obtained only very recently. In April 2019, a series of papers reported direct observations confirming a supermassive black hole in the center of the M87 galaxy. An image of a shadow around the supermassive black hole (the region from which negligible emission reaches the observer) was taken [17, 18]. A shadow around a black hole appears due to the capture of some of the photons emitted by the accretion disk with small impact parameter q. For a nonrotating (Schwarzschild) black hole, $q < 3\sqrt{3} r_g$, where $r_g = GM/c^2$ is the gravitational radius, M is the BH mass [153, 154] (see, e.g., [155–162] for later discussions).

During the last decade, the Event Horizon Telescope (EHT) project participants carried out submillimeter measurements of brightness distribution around black holes in the canter of our Galaxy and the M87 galaxy. The observations aimed at imaging the black hole shadow with the size and form predicted by General Relativity (see, however, the note in the footnote to Section 1.3). The analysis of brightness distribution around SMBH candidate in M87 led to discovering the expected SMBH shadow in M87 [17, 18], thus validating General Relativity.

This EHT result demonstrated the ability to probe phenomena in the immediate vicinity of SMBHs and rendered future observations of nearby SMBHs even more actual and exciting, although technically extremely challenging. Subsequent studies should address detailed plasma processes determining the halo emission around the BH shadow and their dependence on the BH parameters (mass, spin, and possibly charge). The geometry and dynamic state of the magnetic field around the shadow, the dynamical state of the accretion disk itself near the shadow, the possibility of effective high-energy cosmic ray generation, etc. should also be studied. These issues will be addressed in one of the three key top-level projects of the Millimetron space observatory.

From the viewpoint of fundamental physics, SMBH candidates offer the intriguing possibility to observe shadow contours near their event horizon and learn the properties of matter with extreme energy densities through spectral and spectropolarimetric observations. The SMBH surroundings

Table 4. SMBHs for Millimetron.

	M, $M_\odot$	R_S, AU†	D, Mpc††	$\theta_S^\ddagger$	F_{300}, Jy	Reference
MW	4×10^6	8.6(−2)	8.5(−3)	$\simeq 10$	~ 3	[159, 163]
M31	1.4×10^8	3	0.75	4	$\sim 1(-2)^*$	[164–166]
M87	6×10^9	124	16.4	8	1	[167–169]
NGC 1600	$\simeq 10^{10}$	$\simeq 200$	50.2	4	—	[170]
NGC 6166	$\simeq 3 \times 10^{10}$	$\simeq 600$	112	6	—	[170]
Holm15A*	$\sim 10^{11}$	$\simeq 200$	$\simeq 220$	0.9	—	[171, 172]

† AU $= 1.5 \times 10^{13}$ cm is the astronomical unit, the distance from Earth to the Sun.
†† 1 Mpc $= 3 \times 10^{24}$ cm is a megaparsec; 1 pc $= 3 \times 10^{18}$ cm, a parsec.
‡ Angular size in microarcseconds.
* Indirect indications.

can be important sites for the production of high-energy cosmic rays and other high-energy phenomena (see below). However, besides probing the unusual properties of matter under such conditions, these measurements can be crucial in solving a truly fundamental problem of space-time — the search for observational appearances of exotic, so far purely hypothetical, objects — wormholes (see Section 3.3).

Of the many SMBHs available for detailed investigations of the shadow structure by Millimetron both in the single-dish and SVLBI modes, we highlight two, Sgr A* and M87*, whose shadow angular sizes and expected fluxes are within reach of the MSO angular resolution and sensitivity. Several other comparatively close galaxies with SMBHs are presented in Table 4. More extensive lists of SMBHs [10] (including those potentially interesting for MSO) can be found, for example, in papers [173, 174]. An SMBH in the galaxy Holm15A from Table 4 is assumed, because it is the brightest object in the A85 galaxy cluster and has a bright diffuse central radio source. The large velocity dispersion in this cluster, $\sigma_{cl} \simeq 750$ km s^{-1}, can be exactly due to the central SMBH in Holm15A with mass $M_\bullet \simeq 1.5 \times 10^{11} M_\odot$ (see arguments in [171]). Although the SMBHs in Table 4 have comparable angular sizes, expected fluxes are either low (as from the SMBH in M31) or unknown. Therefore, the possibility of a detailed study of their shadow surroundings is presently unclear, and they are not considered to be the main targets.

3.1 Sgr A*

Sagittarius A* (Sgr A*) is the closest supermassive black hole. For a long time, it had been considered the most preferential 'target' to observe the 'image' of the event horizon — the black hole shadow [175] — and probe physical processes in its surroundings [163, 176–178]. Thanks to its proximity, the emission spectrum of Sgr A* has been measured in detail from radio ($\sim$ 100 MHz, see [179]) to hard X-rays [180] (see also reviews [157, 159]). Therefore, the first attempts to image the black hole were, quite expectedly, undertaken for Sgr A*.

These observations were natural to perform in the submillimeter range, where the submillimeter spectral bump, peaking at 0.3–1 mm, is found [181] (see [182, 183] for later results). The emission from a black hole arises in the surrounding accretion disk, and so the spectral features are fully determined by thermal and hydrodynamical properties of the accretion flow and by the emitting particle kinetics. The submillimeter bump arises due to synchrotron self-absorption at low frequencies when passing from the inner optically thick parts of the accretion flow to the optically thin outer regions. This implies that high frequencies at the submillimeter bump are more favorable for shadow imaging [181, 184]. The need for a higher (a few microarcseconds) angular resolution in the submillimeter range requires VLBI observations with baselines as large as Earth's radius or higher. With this goal, the EHT large international project was designed. The project includes several millimeter telescopes located on different continents: Europe, the USA, Mexico, Chile, and the South Pole. [11] The goal of EHT was to image the shadow contour and the surrounding brightness distribution in a 'crescent' form [158]. With sufficient angular resolution and flux sensitivity, these two related characteristics determine, in principle, the parameters of the metric around the black hole, although there is a definite dependence of the brightness distribution and emission spectrum of the 'crescent' around the shadow contour on the magneto-hydrodynamical properties of the accretion flux. For this reason, the determination of the metric is a challenging problem [185–188]. Despite efforts, it was impossible to image the shadow around Sgr A*, even at the highest EHT frequency $\nu = 230$ GHz (1.3 mm), formally providing an angular resolution of around one half the shadow radius [189]. Plasma properties along the line of sight may be responsible for this failure.

3.1.1 Refraction scattering effects on the shadow image. An increase in a source's angular size due to scattering on turbulent inhomogeneities in the interstellar plasma along the line of sight, $\theta \propto \lambda^2$, is a significant factor hampering SMBH imaging [190].

The total wavelength dependence of the image's angular size is presented in Fig. 16 [191] (see papers [183, 192, 193] for other details). Clearly, for observations of Sgr A* at wavelengths $\lambda \lesssim 1.3$ mm, the angular resolution is already under the BH shadow threshold ($\theta \simeq 50$ microarcseconds). The last EHT observations, including the APEX telescope in Chile, almost doubled the VBI baseline and enabled probing three Schwarzschild radii ($\theta \simeq 30$ microarcsec) at 1.3 mm. Thus, resolution is a factor of $\sqrt{3}$ smaller than the shadow size, but its image remained unresolved apparently because of refraction scattering [189].

[10] The most comprehensive information about SMBHs is collected in the NASA/IPAC (National Aeronautics and Space Administration/Infrared Processing and Analysis Center) Extragalactic Database (NED): http://ned.ipac.caltech.edu/.

[11] IRAM/NOEMA (Institut de Radioastronomie Millimetrique/Northern Extended Millimeter Arre) in Europe, JCMT/SMA (James Clerk Maxwell Telescope/SubMillimeter Array), SMTO/KPNO (SubMillimeter Telescope Observatory/Kitt Peak National Observatory) in the USA, APEX (Atacama Pathfinder EXperiment), ALMA in Chile, LMT (Large Millimeter Telescope) in Mexico, and the South Pole Telescope at the South Pole; see http://eventhorizontelescope.org.

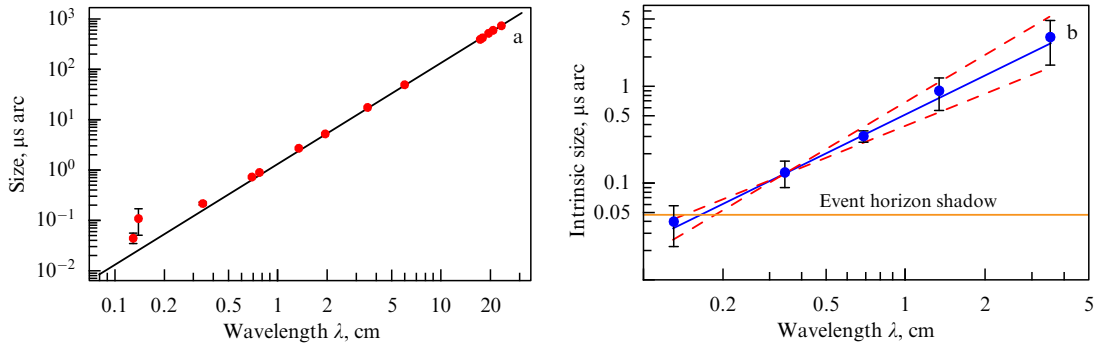

Figure 16. (Color online.) Scattering effects in VLBI observations of Sgr A* [157]. (a) The visible size of the source along the large semiaxis as a function of wavelength. The dependence $\theta \propto \lambda^2$ caused by scattering on inhomogeneities of the turbulent medium is clearly seen. (b) The source's visible angular size after subtracting the dependence $\theta \propto \lambda^2 + \text{const}$ due to the interstellar medium contribution near the black hole. The horizontal line shows the black hole shadow's angular size. (Plot from paper [191].)

Thus, refraction scattering effects are critically important to take an image with the accuracy needed to reliably probe the space-time metric near Sgr A*, the main EHT task. Scattering effects, in turn, are determined by plasma turbulence along the entire line of sight and especially near the black hole. In particular, scattering on electron density inhomogeneities when passing through a turbulent plasma deviate the ray by angle $\langle\theta\rangle \propto \langle\Delta n_e/\sqrt{a}\rangle$, where Δn_e is the electron density fluctuation amplitude, and a is the characteristic size of the turbulence cell (see [194, 195]). This suggests that an increase in the high-frequency harmonics of the fluctuation spectrum will enhance the scattering effects. Recent calculations showed that even a comparatively insignificant change in the turbulence power spectrum $Q(\mathbf{q}) \propto |\mathbf{q}|^{-\beta}$ ($\mathbf{q}$ is the wave vector, β is the spectral power index) from the Kolmogorov ($\beta = 11/3$) to a flatter ($\beta = 3.38$) spectrum would blur the scattering spot (i.e., increase the image size) and other scattering characteristics by an order of magnitude [196].

This fact suggests that high-frequency detectors for which the refraction spot is smaller than at 230 GHz should be used in SVLBI observations. Joint MSO — EHT observations at the shortest wavelengths available offer such an opportunity. These observations will enable probing deeper layers of the Sgr A* shadow. It will be possible, on the one hand, to take an image of the BH shadow, and, on the other hand, to understand the nature and limits of the scattering effects in its surroundings. Recent simulations of synthetic observations in this configuration by the Spektr-M and EHT experimental groups are presented in paper [23].

Here, we should note one more critical point related to the variability of the central parts of the accretion flow and its brightness distribution, which can also appear in the brightness variability of a crescent around the shadow contour and above it. Existing studies suggest variability of Sgr A*'s IR and submillimeter luminosity on a broad time scale from fractions of a minute to several months [197–199]. The synthetic dynamical Millimetron-EHT observations of Sgr A* with a time resolution of 221 s compellingly demonstrate the possibility of constructing a shadow image and its 'crescent' with possible brightness variations [23].

Recently, alternative approaches, including 'space–space' VLBI observations with two-three space telescopes in near-Earth orbit, have also been discussed [200].

3.1.2 Measuring the black hole accretion rate. Determining the accretion rate $\dot{M}_{\rm acc}$ is crucial to understanding processes occurring in the closest vicinity to a black hole, the mass-to-energy transformation mechanisms in the accreting matter, and plasma properties determining radiation from regions immediately close to the black hole shadow. However, current accretion rate estimates are ill-defined and can differ by orders of magnitude (see, for example, [201–203]).

X-ray observations (0.5–10 keV) by the Chandra Space Telescope with high angular resolution ($\sim 1''$) yield the mass accretion rate $\dot{M}_{\rm acc} \sim 10^{-6} M_\odot$ per year. Still, this estimate relates to the periphery of the accretion flow with a size of 0.04×0.04 pc around the galactic center [204].

The determination of $\dot{M}_{\rm acc}$ in deeper regions invokes submillimeter measurements of linear polarization and Faraday rotation measure RM. Due to the Faraday effect, the polarization position angle changes as $\chi(\lambda) = \chi_0 + \lambda^2 \mathrm{RM}$, where [12] $\mathrm{RM} = V \int n_e \mathbf{B}\,\mathrm{d}\mathbf{l}$. The position angle difference at two neighboring wavelengths yields the rotation measure $\mathrm{RM} = [\chi(\lambda_1) - \chi(\lambda_2)]/(\lambda_1^2 - \lambda_2^2)$, which in turn enables the accretion rate to be determined for a given accretion flow model. As a rule, the estimates assume a spherically symmetric flow with power-law density profile $n(r) \propto r^{-\beta}$. The power index β varies from $1/2$ in the convective-dominated accretion flow (CDAF [206]) to $3/2$ for the Bondi accretion ([207]; see also review [208]) and advection-dominated accretion flows (ADAF's [209]). Considering the uncertainty of the models, especially the magnetic field configuration, the upper limit on the accretion rate varies from $\sim 10^{-7}$ (in observations at 230 GHZ [201]) to $\sim 10^{-6} M_\odot$ per year (340 GHz, [202]).

Accretion rate estimates based on brightness temperature measurements of the H30α recombination line near Sgr A* $\sim 10^5 R_S$ [203] are even more model-dependent. They vary from $\sim 2.7 \times 10^{-10} M_\odot$ to $\sim 1.2 \times 10^{-7} M_\odot$ per year, depending on the accretion flow model. Moreover, in this case, the $\dot{M}_{\rm acc}$ estimate can be overestimated because of the maser effect on the H30α line.

In general, the change in the mass accretion rate $\dot{M}_{\rm acc}$ when moving to smaller scales remains highly uncertain. The dependence $\dot{M}_{\rm acc}(r)$ is crucial to understanding physical processes near the black hole event horizon in Sgr A* and the observational appearance of its shadow. Therefore, measuring its spectrum, polarization, and Faraday rotation in a broad range of scales from R_S to $\sim 10^5 - 10^6 R_S$, including

[12] $V = e^3/2\pi m_e^2 c^4 = 8.1 \times 10^5$ rad m^{-2} for n_e in units cm^{-3}, B in micro Gauss, and l in parsecs [205].

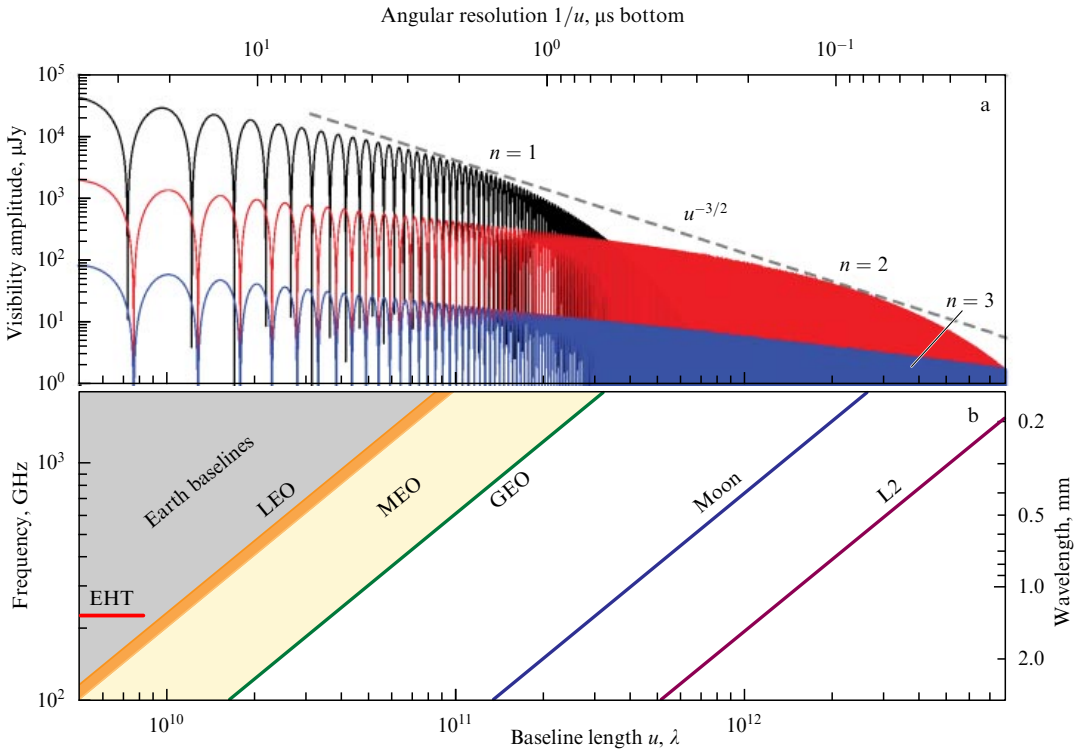

Figure 17. (Color online). (a) The visibility amplitude versus baseline length for a photon ring with angular size $\theta = 40$ microarcseconds and spectral flux similar to that from M87. The black, red, and blue lines correspond to $n = 1, n = 2, n = 3$, respectively. (b) From left to right: the baseline lengths equal to Earth's diameter (corresponding to the EHT interferometer), low near-Earth orbit (LEO), mean near-Earth orbit (MEO), geostationary orbit (GEO), near-Moon orbit (moon), and the L2 point. The visibility amplitude decreases as $u^{-3/2}$ with baseline length. (Plot from paper [155].)

SVLBI observations at wavelengths $\lambda = 420-500$ μm, is essential.

3.2 M87

The M87 galaxy is located at a distance of $\simeq 17$ Mpc; its black hole mass is $M_{\rm BH} \simeq 6 \times 10^9 M_\odot$, so the angular size of its gravitational radius and shadow radius is $\theta_g \simeq 4$ and $\theta_s \simeq 40$ microarcsec, respectively, virtually the same as for the black hole in our Galaxy. The spectral flux at 300 GHz from the M87 SMBH is $F_\nu \sim 1$ Jy, close to that from Sgr A* $F_\nu \sim 3$ Jy (see Table 4). Therefore, from the observational viewpoint, they are practically equivalent. Thus, more striking were successful observations of the SMBH shadow in M87 and failed attempts to see the shadow around Sgr A*. One of the apparent reasons is the difference in refraction scattering. The refraction scattering in M87 should be smaller on general grounds due to the low density and high gas temperature, $n_{\rm e} \sim 0.2$ cm^{-3} and $T \sim 1$ keV, in the very central part within $r < 300$ pc [210]. The low electron density results in lower fluctuation amplitude $|\Delta n_{\rm e}|$; the high temperature and low electron density increase the dissipation scale and, correspondingly, the turbulence cell size a.

3.2.1 Shadow halo substructure at high harmonics. In the SVLBI mode with a baseline of 1000 Gλ, Millimetron will resolve the fine structure of the bright ring around the BH shadow [155]. The BH shadow halo represents a superposition of rings corresponding to the number of 'semi-orbits' of n photons on their way from the source — the accretion disk around the BH, to the observer [155, 156, 211]. Profiles of the consecutive rings with $n > 1$ get 'sharper', i.e., steepen almost exponentially when approaching the shadow boundary. On the interferometric visibility function versus baseline plot, each value of n appears as a set of harmonics, as shown in Fig. 17. The amplitude of the harmonics envelope changes with baseline as $\propto u^{-3/2}$, although the amplitude of fixed harmonics changes as $\propto u^{-1/2} \exp(-wu^\zeta)$, where $w = w(n)$ and $\zeta = \zeta(n)$ are parameters [155]. Clearly, due to the exponential visibility profile amplitude steepening with increasing n and baseline, the current maximum achievable angular resolution of $\theta \simeq 20$ microarcsec is insufficient to resolve not only the photon ring fine structure but even the large baseline asymptotics, $u \gtrsim 10^{12}\lambda$, where different n ($n = 1, 2, 3$) change differently. Figure 17 suggests that this can be possible with Millimetron observations in a highly elliptic orbit. Observations from the L2 point with longer baselines $u > 300$ Gλ will enable measuring the asymptotic $u^{-3/2}$ for $n > 1$.

3.2.2 Studying physical processes near the event horizon. A clear advantage of Millimetron compared to the current EHT array is the possibility of multifrequency VLBI observations (bands of ~ 100, 240, 310, and 640 GHz), which makes it possible to perform polarization measurements of the close vicinities of the Sgr A* and M87 SMBHs. By themselves, such observations will narrow the class of statistically acceptable models inferred from comparisons with numerical simulations and increase the reliability of quantitative conclusions. Measurements of the Faraday rotation and magnetic fields on Schwarzschild scales, especially their variations, will be critical. These data will provide information on plasma turbulence near the shadow and radiation generation and

transfer mechanisms. The turbulence in this region can determine the shadow distortions due to refraction scattering blur. Indeed, for long VLBI exposures, turbulent pulsations on scales of a few gravitational radii with a characteristic time from a few dozen seconds to several minutes can sum up to increase the refraction scattering blur. Such superposition can appear as a sufficiently broad emission spectrum and hamper BH shadow imaging even at high frequencies. Considering that time variations of far IR and submillimeter intensity from Sgr A* can reach one order of magnitude [163], the effect can hardly be disregarded. Its quantitative measuring is critical. It is important to note that, in this spectral range, structural changes of the accretion flow on larger scales in the shadow region can also appear [212, 213], which can also contribute to the scattering blur in the VLBI observations.

Results of spectropolarimetric observations of broader regions around Sgr A* and M87*, up to the Bondi radius $R_B \sim 10^5 R_S$ (for M87*, it corresponds to about 0.1 pc), will probably be of similar significance. Here, measurements of multifrequency intermittence patterns (including differential characteristics) and their wide-field space profiles can be very informative. Such observations are aimed at elucidating the turbulence properties (power spectrum, dissipation scale), refraction scattering limit, characteristics of the putative jet along the line of sight (see the discussion in [189]), accretion flow features, mechanisms of the accretion rate decrease when going from the periphery to the center, etc. These measurements are crucial to understanding the accretion plasma processes (which is important by itself) and constructing average radial density and velocity profiles of the accretion flow needed to get a more reliable accretion rate estimate. Measurements of the magnetic field strength, topology, and radial dependence in and outside the accretion disk are also valuable. Current accretion rate estimates are based on the Faraday rotation measure RM with the subsequent (mostly arbitrary) fitting of the accretion flow parameters (see [214, 215] and Section 3.1.2 for more discussion). The magnetic field strength and radial dependence are also critical for the potential appearances of wormholes.

3.3 Wormholes and Millimetron

The search for wormholes is one of the important research initiatives of the Millimetron observatory. A wormhole is a hypothetical object theoretically predicted by General Relativity [216–218]. It consists of two entries (mouths) — three-dimensional holes in space connected by a tunnel (throat) lying outside our space-time in a superspace. The mouths can be located in space far away from each other; the throat length in the superspace can be very short. The mouths can even be in different universes. Unlike black holes, wormholes have not been discovered in astrophysical observations so far. Note that GR has theoretically predicted several objects whose existence was categorically negated initially by both theoreticians and observers because of their extreme peculiarity. Among them are neutron stars, black holes, and the Λ-term in GR equations. Only after decades of thorough development by theoreticians and observers were they discovered in the Universe. Among such peculiar objects, wormholes take a special place, because the possibility of their existence enables probing complex space topology and the presence of other universes, which is a philosophical issue. The hypothesis [219] argues that the nuclei of some galaxies can be wormhole entries and not supermassive black holes. The project proposes checking the wormhole hypothesis by using different observational appearances of wormhole entries and black holes.

Wormholes can be of two types: with space-oriented (spacelike) and time-oriented (timelike) tunnels [220]. The project aims to search for type-one wormholes, because they are expected to demonstrate more distinct observational appearances and are better studied theoretically. We will deal with such wormholes and mention type-two wormholes only when necessary.

The masses of type-one wormhole entries can be arbitrary, unequal in each pair or even negative. The entries remove do not have, unlike black holes, an event horizon and sharp boundaries in general. One may enter and exit a wormhole. Wormholes, in principle, can be static or quasi-static. They can be traversable in both directions for matter and radiation. The radial magnetic field can pass through the throat from one entry to another and be kept from expanding by the space topology — tunnels. In this case, the exits will appear as magnetic monopoles with the opposite sign. Note that, in the absence of an elementary magnetic monopole in nature, such fields cannot exist in black holes. [13]

Principal observational signatures that a compact object is a wormhole mouth and not a black hole are as follows:

- The magnetic field near the entry is monopole. The maximum magnetic field is estimated to be

$$H = 3 \times 10^{10} \left(\frac{3 \times 10^{14} \text{ cm}}{R_{\text{th}}} \right) \text{G} . \tag{11}$$

Here, R_{th} is the radius of the wormhole throat.

- Matter can outflow from the mouth, i.e., one can observe blueshifted radiation from the outflow near the mouth. The blueshift depends on the outflow rate through the wormhole, which is a priori unknown.

- In principle, one can see other regions of our Universe or even other universes through the wormhole throat, resulting in a specific shadow of the wormhole with apparent small-size structures.

- The fundamental possibility of seeing wormhole interiors and space outside the opposite entry enables the variability of radiation passing through the wormhole on timescales smaller than its mouth's light-crossing time. Changes in the time dilation in strong gravitational fields must be taken into account.

These observational properties are sufficient but not necessary.

When equilibrium is broken, the gravitational collapse of a spacelike wormhole results in the appearance of two black holes at the site of the entries [221]. These black holes are connected in the superspace by a singularity arising during the collapse. When the original wormhole contains a magnetic field, this field will be conserved near the exits consisting of black holes (see [221] for more details).

Note, in conclusion, that the structure of tunnels of timelike wormholes is much more complicated and contains, in particular, Cauchy horizons and infinite space-time regions outside our Universe. Therefore, processes outside the Cauchy horizons depend on conditions both in our Universe and in these additional structures (see [220]).

[13] Theoretically, one may consider an electric field instead of a magnetic one. However, in real astrophysical conditions, the electric charge is rapidly neutralized by charged particles with the opposite sign. Therefore, we do not consider this option.

Importance.

The discovery of wormholes would revolutionize modern astrophysics by proving the existence of fundamentally new objects, a complicated topological space-time structure, and even the possibility of the presence of other universes.

The results would be of fundamental significance for astrophysics, physics, and science in general and bear philosophical meaning.

Realizability.

MSO will perform direct SVLBI observations, including polarization measurements with a record-high angular resolution previously unavailable. Estimates show that these observations are possible for our galactic center and other galaxies (see the discussion above in Sections 3.1, 3.1.1, and 3.2). It is important to stress that searches for wormholes will be based only on observations designed to probe physical processes and space-time geometry near the event horizon of possible black hole candidates. Therefore, they will not require additional technical or time resources. Here, measuring the strength and spatial configuration of the magnetic field can be crucial. The magnetic field in accretion disks around supermassive black holes is described by the radial profile $\propto r^{-1}$ and has an upper limit of the order of $H \sim 10^3 - 10^4$ G (see, for example, [222]). Therefore, finding a field exceeding this upper limit or different from the r^{-1} radial profile may suggest the presence of a wormhole (see [223] for a brief discussion).

3.3.1 Probing space-time near the event horizon. The (orbit-dependent) possibility of measuring space-time scales much smaller than the Schwarzschild radius $2r_g$ and light-crossing time $2r_g/c$ of nearby SMBHs (see Table 4) is an important advantage of Millimetron over currently operating projects and those slated for the next decade. The angular size of the Schwarzschild radius in Sgr A* and M87 is ~ 10 microarcsec. Even for the Millimetron lunar-orbit size orbit, the 'Earth–Space' interferometer at the longest common wavelength with ALMA, $\lambda = 3$ mm, will have an angular resolution of $\theta \sim 2$ microarcsec. The same configuration for Millimetron at the Lagrangian point L2 will yield $\theta \sim 0.4$ microarcsec. In the first and second case, this value is one fifth and one twenty-fifth the Schwarzschild radius, respectively. Such observations would enable both probing the geometry and physics of the halo fine structure around black hole shadows and registering phenomena on sub-Schwarzschild scales, which is now unavailable. They would also check the (sufficient) signatures of a wormhole in Sgr A* and M87 (see Section 3.3 above), by assuming the gravitational radius r_g of the central object to be the wormhole throat size.

The Millimetron orbit at the L2 point will allow studying black hole shadows and searching for wormhole signatures in other galaxies from Table 4 with much smaller Schwarzschild angular sizes. This will substantially extend our capabilities to probe various space-time geometries in strong gravitational fields. In Sgr A* and M87*, angular and time resolutions are smaller (and significantly smaller) than $\Delta\theta \sim 5$ microarcsec and $\Delta t \sim 20$ s and $\Delta t \sim 25$ min, respectively.

In recent years, extensions of VLBI methods for the observation of objects with extremely small angular sizes and time variations on the corresponding short time scales have been discussed [224–226]. This VLBI 'dynamical' imaging is based on simple time separation of images on time scales sufficient to detect the signal at a given signal-to-noise level. An example of synthetic 'dynamical' VLBI images of the shadow halo around the black hole in M87 is presented in Fig. 18. Here, a relativistic magneto-hydrodynamical model of the accretion disk emission around M87* is utilized.

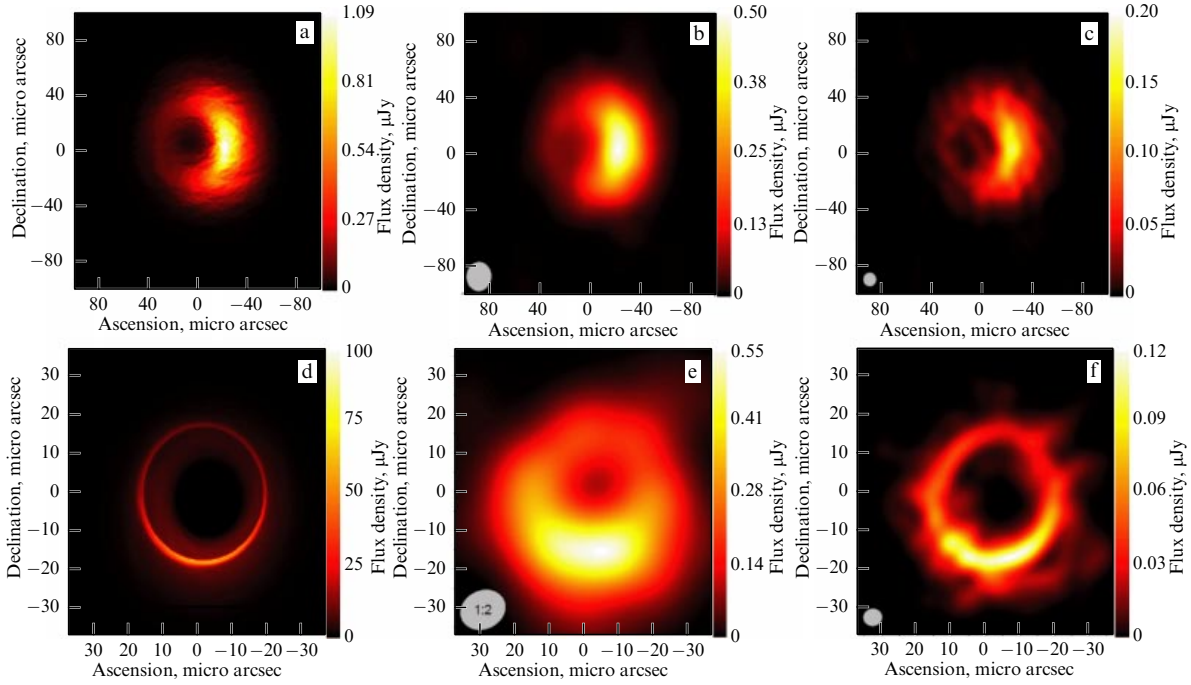

Figure 18. (Color online.) Recovered VLBI image of Sgr A* (a, b, c) and M87* (d, e, f) at 230 GHz. (a, d) Averaged MHD models (a – Sgr A* taking into account scattering, d — M87* with parameters corresponding to the EHT 2017 observations [20]). (b, e) Recovered VLBI images using ground-based EHT telescopes. (c, f) Recovered VLBI images from observations of ground-based EHT telescopes together with Millimetron in a near-Earth elliptical orbit. (Images from paper [23].)

Observations of Sgr A* at $\lambda = 3$ mm with a baseline of $\sim 500\ G\lambda$ corresponding to the L2 point will resolve ~ 0.6 microarcsec details with space scales of $\sim 0.15 r_g$ with a visibility function amplitude of $V \sim 30$ mJy. This means that with a ~ 1 mJy sensitivity of Millimetron for a one-hour exposure, it will be sufficient to separate images by several minutes. This time interval is much longer than the light-crossing time $t_g = r_g/c \sim 20$ s for a black hole or hypothetical wormhole in Sgr A* but is comparable to the characteristic time near the shadow, $t_{sh} \gtrsim 3\sqrt{3} r_g/c \sim 2$ min. Assuming the possible time variability at the wormhole entry with the Schwarzschild radius of Sgr A* $r = r_g$, the observed redshift of matter can be high enough (considering that the effective masses near wormhole entries and gravitational potential distribution in the throat are strongly model-dependent) to enable 'dynamical' VLBI observations by Millimetron.

3.3.2 'Microscopy' of SMBHs in the distant Universe. Clearly, the capabilities of MSO to probe regions near black hole horizons are not limited to the closest SMBHs in our Galaxy and M87. A potential object is the quasar TON 618 with an optical luminosity of $\lambda L_\lambda \sim 2 \times 10^{47}$ erg s^{-1} and SMBH mass $M_{BH} \simeq 6 \times 10^{10} M_\odot$ [227]. Despite the quasar redshift $z = 2.2$, the black hole shadow can be studied in detail by VLBI Millimetron observations. In addition to measuring the space-time geometry and plasma dynamics near the black holes discussed above, observations of distant SMBHs could be invaluable for clarifying the origin of ultra-high energy cosmic rays (UHECRs). In recent years, a lot of observational evidence has appeared suggesting that high-energy CRs (including neutrinos) with energy from hundreds of TeV to several PeV can originate in quasars, specifically in their subclass blazars with ultra-relativistic jets directed along the line of sight towards us. The most well-known is quasar TXS 0506+056, from which an intense neutrino flux with energies up to PeV and gamma rays was detected [228] (see also note added in proof). Radio observations of TXT 0506+056 suggest that both gamma rays and high-energy neutrinos can be generated in the innermost (close to the event horizon) accretion disk parts [229]. This hypothesis could be tested with Millimetron. Presently, it is hard to assess such a possibility because of the lack of reliable observational data on submillimeter emission from such objects.

3.4 Search for obscured SMBHs in galaxy mergers: Arp220

Galaxy mergers (merging galaxies) represent the main elementary event in the hierarchical scenario of galactic mass spectrum formation in the Universe. Considering observational selection effects, one can conclude that most galaxies should harbor central SMBHs [230], due to the stimulating role of converging flows during the merging that provide mass inflow into central regions and enhance mass accretion rate onto already existing central SMBHs or their seeds [231, 232]. Moreover, for the same reason, the brightest $L \sim 10^{45} - 10^{47}$ erg s^{-1} SMBHs (active galactic nuclei) occur predominantly in obscured (by heavy dust and gas absorption) mergers [233]. Thus, galaxy mergers hide in their interiors one of the most intriguing physical and astrophysical phenomena — the origin of SMBHs. Probing deep inside them will enable understanding physical process under extreme accretion rates onto black holes and possibly plasma properties with extreme energy density near binary supermassive black holes. It is a challenging task, because the column densities along the line of sight far exceed the Compton limit $N_{CT} \sim 10^{24}$ cm^{-2}, and therefore the central regions are highly absorbed by large masses of dust and gas. Direct observations are possible only in the far IR and submillimeter range and in hard X-rays ($E \geqslant 15$ keV) [233].

Closely approaching merging galaxies appear as ultraluminous infrared galaxies (ULIRGs) with luminosity above $L \sim 10^{12} L_\odot$ [119, 234]. Such a galaxy, Arp220, lies nearby at a distance of 77 Mpc and has an IR luminosity of $L \simeq 2 \times 10^{12} L_\odot$ [235, 236]. Due to the high dust concentration in Arp220, four times as high as in our Galaxy [120], most of its stellar population is obscured (optical depth in the visual band is $\tau_v \sim 45$ [237]). Moreover, the galaxy's central regions are not transparent even to far IR and submillimeter radiation: the optical depth inside $R \sim 100$ pc is about $\tau_{100} \simeq 5$ at $\lambda \sim 100$ μm [238] and $\tau_{1000} \sim 1$ at $\lambda \sim 1$ mm; therefore, a detailed study of the central parts of Arp220 is very complicated. Radio observations of Arp220 compellingly suggest that its center is split into two nuclei, eastern and western, separated by $\sim 1''$ (~ 400 pc). The nuclei are surrounded by counter-rotating disks with similar rotation parameters. The disks are embedded into a giant ($\sim$ kpc) molecular cloud. The supernova explosion rate in the WN region with radius $R \sim 100$ pc is 100 times as high as in our entire Galaxy. It results in an unusually high radio brightness and dust production rate in the Arp220 center (see, for example, [239–241]).

3.4.1 X-ray. The possible existence of an SMBH in Arp220 (in the western nucleus, WN) hidden from direct observations by a high optical depth of dust has been actively debated since paper [242]. The first arguments favoring the black hole were based on the very high IR luminosity of the dusty central nucleus with a size of about 70 pc, $L_{IR} \sim 10^{12} L_\odot$, which required an unusually high density of OB stars, about 10^6 in a volume with a radius of 35 pc [242] (see also the discussion in [241]). Later X-ray observations ($E_x = 2-10$ keV, likely primarily due to 6.7 keV FeXXV line emission) revealed the presence in the center of Arp220 (both in the western and easter (EN) nuclei) of powerful sources with luminosities of 2×10^{40} erg s^{-1} and 3×10^{40} erg s^{-1}, respectively. Calculations of bolometric luminosity taking into account absorption of optical and near IR emission by dust yield lower limits of 8.3×10^{43} erg s^{-1} (EN) and 2.5×10^{43} erg s^{-1} (WN). Assuming the Eddington luminosity with an efficiency of $\sim 5 \times 10^5 M_\odot$, the BH masses are $\sim 10^5 M_\odot$ and $\eta = 0.1$, respectively [243]. However, it should be borne in mind that the IR and X-ray observations can equally suggest an accreting black hole or a star-formation burst as the power source.

3.4.2 Molecular lines. Additional indirect arguments favoring black holes in Arp220 came from interferometric observations of molecular ($H^{13}CN$, $H^{13}CO^+$, $HN^{13}C$, and SiO) lines [244]. The abundance ratio $[H^{13}CN/H^{13}CO^+] = 11$ in the western nucleus, WN, is two orders of magnitude as high as in the eastern nucleus, EN. Such a significant difference can most likely be due to the presence of an active galactic nucleus in the WN, as suggested by the empirical data on the molecular composition in AGNs and star-formation regions [244–246]. This is a qualitative conclusion and cannot be used to estimate the black hole mass.

Observations of CO molecule kinematics jointly with dust emission in the WN and EN suggest that gas and dust are

located highly symmetrically with a regular axially symmetric velocity distribution corresponding to disks. This can result from the long lifetime of the disks over several proper rotational periods. The disk kinematics in the western nucleus suggest a compact central (unresolved) body with a total mass of $\sim 8 \times 10^8 M_\odot$, likely a black hole embedded in a very compact molecular-dust cloud.

H_2O megamasers serve as one of the SMBH indicators. In particular, this can be due to water being a ubiquitous molecule thanks to active evaporation of dust ice mantles under shock heating conditions around black holes [247]. High-resolution ALMA observations of H_2O emission in the nucleus of Arp220 show that most (2/3) of the emission comes from the western nucleus [248]. The H_2O molecule number density in the emission region is estimated to be $X(H_2O) \geqslant 10^{-6}$, typical of water masers. In total, three lines at 22, 183, and 325 GHz are observed. Their low brightness temperatures $T_b \lesssim 10$ K (see Table 2 in [248]), unusual for water masers, can be easily explained by the fact that maser concentrations have sizes significantly (by at least an order of magnitude) less than the ALMA beam, $\simeq 0.02''$. The relation between brightness temperatures T_b at different frequencies rules out their thermal character in molecular disks of Arp220. The reason for this can be due to varying sizes of concentrations producing the maser effect in the 22 GHz line, on the one hand, and in the 183 and 325 GHz lines, on the other hand [248]. The origin of the maser H_2O emission in Arp220 can be clarified by Millimetron SVLBI observations. For the Arp220 distance ($\simeq 80$ Mpc), at 325 GHz, Millimetron's angular resolution in a near-Earth orbit and in the L2 point orbit would correspond to the space scales of $\gtrsim 2 \times 10^{-3}$ pc (around 500 a.u.) and 4×10^{-5} pc (6 a.u.), respectively.

4. H_2O, prebiotics, life in the Universe

Studying the origin and evolution of life in the Universe is one of the key fields in modern astrophysics. Great interest in this topic resulted in the emergence of a new science discipline, astrobiology, combining the efforts of various specialists: astronomers, biologists, geologists, etc. Many space agencies, including NASA, have an astrobiology division. In Europe, the European Astrobiology Network Association, including a Russian council representative, was created to coordinate astrobiological research. There are several scientific journals dedicated to astrobiological research.

Observational astronomy, astrophysics, and astrochemistry have their niche in this research: they endeavor to find astronomical prerequisites for the appearance of life in the Universe. The search for these premises is conducted in different areas: studies of the evolution of organic matter (chemical basis of life) in the interstellar medium, protostellar condensations, and protoplanetary and planetary systems; studies of the synthesis and transportation of water as an effective solvent (assuming that life in the Universe is predominantly carbon-water based); extrasolar planetary systems with an energy source and conditions suitable for the origin of life; the discovery of exobiosphere indicators; etc. Stellar nucleosynthesis enriched the Universe with the heavy (heavier than helium) elements live organisms consist of. At first glance, it seems inevitable that, as stellar populations of galaxies in the observed part of the Universe are very similar, the conditions for the emergence of life should be approximately the same everywhere. However, details of the evolutionary chain leading to the origin of life with all prerequisite conditions and even more straightforward questions related to the transformation of a fraction of gas in galaxies into stars are only crudely understood and need further studies [21].

Besides studies of the nonbiological evolution of organic matter, also of interest are more general questions related to stellar and planetary formation, especially massive star formation in which thermonuclear reactions begin before the stellar mass increases to the total value. Despite many studies, the specific formation scenario of these objects is unclear (most likely, there are several mechanisms). High-sensitivity submillimeter observations will enable clarifying the formation of massive young stellar objects and their interaction with the ambient medium. In particular, these observations will make it possible to investigate the structure of so-called 'hot cores' around massive protostars, ionized hydrogen regions, including the very early stages of their evolution, photodissociated regions, and high-velocity matter outflows. Studies of these structures will enable us to consider the active interaction between different interstellar and circumstellar medium components, where the energy release by forming and recently formed stars stimulates the subsequent stellar generation formation.

The possibility of planetary system formation around massive stars is questionable (although circumstellar disks are observed around them, see, e.g. [249, 250]). However, massive stars are undoubtedly important in the evolution of organic matter. High temperatures around massive (proto)stars stimulate the chemical synthesis of complex molecules both in the gas and on cosmic dust surfaces. Studies of cosmic dust grains themselves in star-forming regions (possible changes in the dust chemical composition and structure, variations of the dust to gas mass ratio, dust grain destruction) are of great interest. Millimetron will enable investigating these phenomena by observing emission from dust, high-excitation transitions of different molecules, as well as atoms, ions, and molecules that are unobservable by ground-based telescopes. In combination with ground-based observations, these measurements will provide a much more complete picture of star formation.

4.1 Star formation

Life in the Universe originated from the first star. The initial stages of stellar nucleosynthesis enriched the Universe with the elements heavier than helium (metals) that enter all living matter; hence, the possibility of forming life everywhere in the Universe. For this reason, learning processes related to star birth in the Galaxy are relevant to the issue of the origin of life. Here, the following is important: as noted above, the existence of planetary systems around massive stars with huge luminosity seems to be ruled out. More favorable conditions can be met around solar-type stars, as suggested by present-day observations (see [251] for a review). Thus, massive stars produce heavy elements, while low-mass stars harbor planetary systems and supply them with energy. Therefore, it is essential to understand the transition of heavy elements in the right amount from massive to low-mass stars (some aspects of this process are discussed in [21]).

Presently, it is commonly accepted that stars form in dense interstellar gas-dust clouds. Due to a large amount of dust along the line of sight, their interiors are well protected from external ultraviolet radiation. The principal constituent of the interstellar medium, hydrogen, is present in such clouds in molecular form. These clouds are called molecular clouds.

The characteristic temperatures of the clouds are 10–20 K. The H_2 molecule does not have a dipole moment; therefore, it does not have a rotational spectrum that could be observed at these low temperatures. Thus, molecular clouds are probed by rotational transitions of CO molecules, the second most abundant after H_2 molecules in the interstellar medium. The clouds contain a variety of molecules, from the simplest to complex organic species. To date, about 200 different molecules, excluding isotopologues, have been found in molecular clouds.[14] Observations of these molecules and dust provide the main information about these clouds' physical characteristics and ongoing processes.

At these temperatures, the dust mostly radiates at submillimeter wavelengths. Spectral lines of molecules from these clouds also fall within the submillimeter wavelength range. Most of these lines are produced by transitions between different vibration-rotational states of the molecules. So-called inverse transitions (for example, in the ammonia molecule) and several others are also observed. Measurements of lines arising from transitions between fine-structure spectra of some atoms and molecules (for example, OI, CI, CII) are also invaluable. Observations of many important lines are impossible from the ground even at high-mountain observatories because of the high atmospheric opacity at these frequencies. Airborne SOFIA (Stratospheric Observatory For Infrared Astronomy) is used to alleviate this problem [252]. Great progress in molecular cloud studies was achieved from the space submillimeter observatory Herschel [253], operated successfully in 2009–2013. Millimetron's capabilities (both sensitivity and angular resolution) will be much better than Herschel's, enabling us to obtain unique information that can help resolve the key issues of the structure and evolution of molecular clouds and star formation.

One such question is the understanding of the initial conditions and possible trigger mechanism of star formation. Recently, thanks to the Herschel space telescope observations, a new star formation paradigm has appeared. According to this idea, active star formation occurs mainly in the interstellar filaments that have been known for a long time [254]. Most of the interstellar clouds appear to have a filamentary structure. The Herschel telescope studied filaments in relatively nearby (~ 200 pc) clouds. The main features of the filaments have been determined. In particular, they were found to have a universal thickness of ~ 0.1 pc, which is not fully understood. Subsequently, more distant filaments were observed (e.g., [255]). Generally, interstellar filaments are a very promising field of research, and Millimetron observations can strongly contribute here. The filament thickness corresponds to an angular size of $20''$ from one kpc distance. With a few arcseconds of angular resolution, Millimetron can investigate in detail such objects in the wavelength range unavailable to ground-based telescopes. Here, of importantance will be observations of both the spectropolarimetric dust continuum and line emissions from different atoms and molecules.

Observations of dust will be crucial for the study of cold clouds. First of all, Millimetron will have maximum sensitivity in the continuum. Second, in cold regions, submillimeter transitions of most molecules will be weakly excited. The carbon ion [CII] line at 158 μm is one of the most important tracers of different components of the interstellar medium. The Herschel telescope observed this line from very different regions [256]. The discovery of a large amount of molecular gas in which no CO molecule lines (which is thought to be the primary molecular gas tracer) were observed was important [257]. CII emission was also shown to be well correlated with the star formation rate [258], thus being a useful indicator of this process. In the SOFIA observations, ^{13}CII isotope lines were registered [259], enabling estimating the principal isotope line's optical depth and column density.

Observations of CII and ^{13}CII lines should be priority studies of the interstellar medium by Millimetron. They allow investigating different ISM components, including star-forming regions, with a record high sensitivity and angular resolution.

The deuterium hydrogen molecule HD can also be a valuable molecular gas tracer. The HD to H_2 ratio is $\sim 3 \times 10^{-5}$. Unlike the main hydrogen isotope, the HD molecule has a small electric dipole moment. As a result, a rotational spectrum arises with the resonance transition $J = 1-0$ at a wavelength of about 112 μm. As the level $J = 1$ excitation energy is about 130 K, its population in cold molecular clouds should be small. Correspondingly, the HD emission intensity will also be weak. Nevertheless, this line was successfully measured by the Herschel telescope with a high signal-to-noise ratio in the disk around the star TW Hya, whose temperature is about 30 K [260]. Studies of individual sources and surveys in the HD line are a valuable tool for probing star-forming regions. In particular, in addition to CO, HD molecules can be used to measure the mass of protoplanetary disks [261–263], because their abundance is determined solely by the local disk temperature and density and only weakly depends on chemical details. As a result, the HD molecules' spatial distribution and total mass in the disk are primarily determined by the H_2 mass and disk morphology (Fig. 19). HD observations are in principle possible with the SOFIA aircraft observatory. However, Millimetron will be able to provide much better sensitivity and angular resolution.

Generally, the formation stages of comparatively low-mass stars are now known quite well both observationally and theoretically (see, e.g., [264]). The formation of massive stars in which nuclear reactions begin at the mass growth stage is much more poorly understood [264, 265]. These stars strongly affect the surrounding medium. In particular, the protostar radiation pressure can stop mass accretion, making it difficult to explain the formation of very high-mass stars.

The basic scenarios of high-mass star formation presently discussed include a monolithic collapse of a massive dense nucleus and so-called concurrent accretion. Quite exotic models have also been proposed in which massive stars result from the coalescences of lighter components [266].

Observations of star-forming regions of massive stars are problematic, because they are rare and distant. The monolithic collapse model assumes the presence of massive nuclei (with a mass of $\sim 30 M_\odot$ and a radius of 0.03 pc) that could form a high-mass protostar. However, only a few dozen such candidates have been found [267]. A large number of low-mass nuclei are known, though. Millimetron's angular resolution and sensitivity enable searching for dense protostellar nuclei within several kiloparsecs. Surveying large sky patches would require too much time, but Millimetron could search for dense pre-stellar and protostellar nuclei inside selected areas, which would be invaluable to understand the star formation process in general.

[14] https://zeus.ph1.uni-koeln.de/cdms/molecules, http://www.astrochymist.org/astrochymist_ist.html.

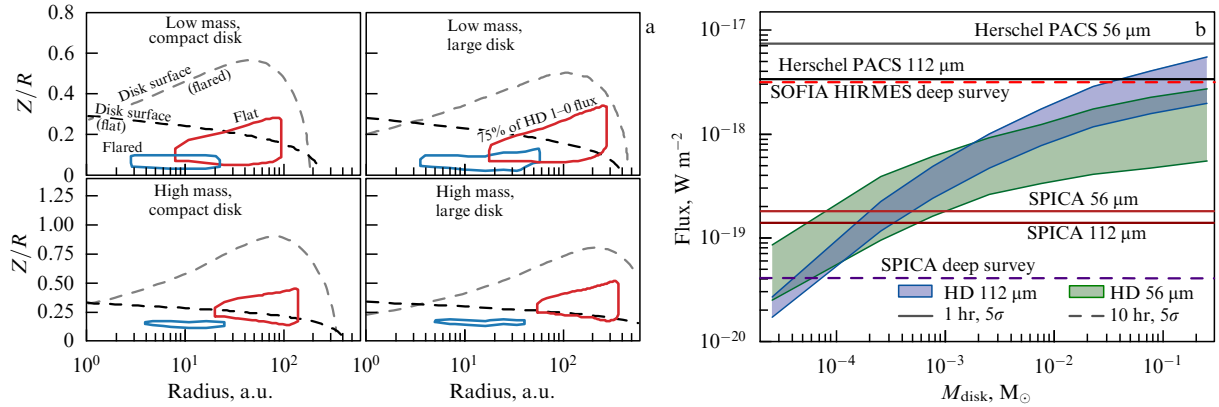

Figure 19. (Color online). (a) Model HD molecule distribution in protoplanetary disks from HD $J = 1 - 0$ observations. Solid contours encircle 75% $J = 1 - 0$ disk emission regions. The blue and red contours correspond to thin (cold) and thick (warm) disks, respectively. The dashed lines are isocontours of equal gas number density $n_g = 10^6$ cm^{-3} in the disk. The top and bottom rows show low/high-mass disks, respectively. The left/right columns correspond to compact/extended disks. Figure from [262]. (b) Model dependence of the HD $J = 1 - 0$ (blue band) and HD $J = 2 - 1$ (green band) flux on the protoplanetary disk mass at 140 pc. Different lines show the far-IR sensitivity limits of various telescopes: the Herschel telescope (completed operations), the SOFIA HIRMES (High-Resolution Mid-infrared Spectrometer) stratospheric observatory, and future SPICA (Space Infrared telescope for Cosmology and Astrophysics). The 100–300-μm sensitivity of the MSO mirror cooled to 20 K will be almost two orders magnitude better than SPICA's. (Figure from paper [261].)

Hot cores, ionized hydrogen, and photodissociation regions are formed around massive protostars. Powerful high-velocity outflows are observed. Active interaction between interstellar and circumstellar matter occurs. Induced star formation is possible. The effect of massive stars on the surrounding medium creates high-density and high-temperature regions radiating mostly at submillimeter wavelengths. Observations of high-excitation transitions of different molecules, first and foremost CO, serve as an important diagnostic tool.

One of the key missions of the Herschel space telescope (WISH, Water in Star-forming regions with Herschel) was dedicated to probing water in star-forming regions [268]. This mission's results showed that a strong emission of water molecules is observed from different types of protostellar objects and supplies unique information. Water emission is often associated with shocks, because the enhanced temperature in these regions leads to water molecule evaporation from dust grain surfaces. In particular, submillimeter water molecular lines probe different bipolar outflow components in star-forming regions that can hardly be studied by other means [269]. The discovery of different absorption lines of H_2O^+ from various objects was unexpected. These lines arise in a low-density gas with a small molecular proportion. Millimetron will be able to continue these critical studies at the new level.

Ionized hydrogen regions around young massive stars and protostars — nonstationary objects that actively interact with the ambient matter and may trigger new star formation in the surrounding envelopes — have been actively investigated. Recently, the SOFIA observations enabled measuring for the first time the HeH^+ molecule $J = 1 - 0$ line at a frequency of about two THz (149 μm) [270] (Fig. 20). The line was detected from the planetary nebula NGC7027. This molecule is formed most efficiently in the He^+ helium ion reaction with atomic hydrogen. Thus, its number density should peak at the boundary of ionized regions around very hot stars, which produce enough ultraviolet radiation. Observations of this line could provide a new diagnostic of such objects, and here Millimetron will be beyond comparison. Measurements of the HeH^+ $J = 2 - 1$ transition at 4 THz could help to better understand physical conditions in these regions.

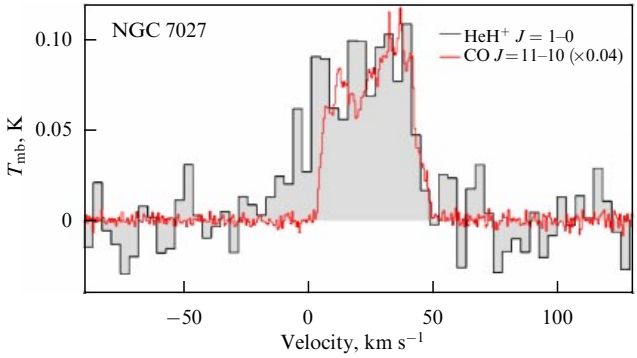

Figure 20. (Color online.) Spectrum of the rotational HeH^+ ($J = 1 - 0$) transition measured with the upGREAT (upgraded German REceiver for Astronomy at Teraherz frequencies) instrument aboard SOFIA in the direction of NGC 7027. For comparison, shown is the CO ($J = 11 - 10$) line arising in a dense molecular shell near the ionization front from which the HeH^+ emission is expected. (Figure from paper [270].)

High gas temperatures around massive protostars stimulate chemical processes of complex organic molecule formation. These molecules are considered below.

4.2 Evolution of organic substances

Recent submillimeter and millimeter observations have significantly extended our knowledge about the evolution of the molecular composition of interstellar clouds, protostellar objects, and protoplanetary objects. PRIMOS (Prebiotic Interstellar Molecule Survey) at Green Bank (see, for example, [271]) and SOLIS (Seeds Of Life In Space) conducted at the IRAM NOEMA interferometer [272] should be noted among ground-based projects. The latter project investigates the spatial distribution of complex organic molecules characteristic of different chemical processes (in the gas phase, on surfaces, and inside ice mantles of dust grains, related to gas-solid phase interactions) in the direction of typical objects at each star-formation stage. These objects include cold pre-stellar cores, hot cores, class 0 and I protostellar objects, protoclusters, and shock fronts in molecular outflows [273–276]. The purpose is to find the most efficient and prevailing synthesis paths of complex organic

molecules during the formation and evolution of protostellar objects of different masses. In astrochemistry, complex organic molecules (COMs) include substances consisting of five-six atoms [277], which, of course, significantly differs from the notion of a complex molecule in biology. However, on the other hand, one should remember that here we consider chemical synthesis at very low density and cryogenic temperature. Clearly, under these conditions, the number density of more complex molecules can prove to be too low, rendering their discovery challenging. Nevertheless, even in such conditions, recent observations enabled detecting emission from COMs consisting of many more than ten atoms [278, 279]. Their number density was found to be higher than the model predictions (see in [279]). By itself, this fact strongly suggests the existence of complex ('prebiotic') interstellar organics.

Modern submillimeter observations became possible first of all due to the Herschel Space Telescope and ground-based ALMA interferometer. High-sensitivity observations in this range allow lines of new molecules and new reservoirs of already known species to be discovered, for example, by detecting transitions from highly excited levels. Presently, the complete list of interstellar and circumstellar molecules includes more than 200 species [278]. Their main synthesis mechanisms are elaborated theoretically.

The formation of molecules (including organic) occurs both in the gas phase and on the surface of dust grains. It is assumed that in dark, cold clouds (at the pre-stellar stage), methanol is synthesized by diffusion chemistry on the interstellar dust grain surface (see, for example, [280]). The formation mechanisms of more complex molecules are less understood. Ion-molecular reactions in gas apparently synthesize hydrocarbonates (C_xH_y-like molecules). The formation of COMs containing oxygen and nitrogen remains unclear. At least two possible scenarios are discussed. The first assumes COM synthesis in cold icy mantles of dust grains due to interaction with cosmic ray particles [281]. In the second scenario, COM synthesis occurs in neutral-neutral reactions in the gas phase. Reactants for these reactions are produced on dust grain surfaces and then expelled into the gas by chemical (reactive) desorption [282].

When ultraviolet radiation sources emerge inside molecular clouds at later protostellar evolution stages, COMs are recognized to be formed during the gradual heating of a gas-dust mixture (the warm-up scenario, [283]). Here, photo-induced processes in icy mantles of cosmic dust grains become essential [284]. Photons destruct the initial cold synthesis products present in the mantles after the cold protostellar phases. The increasing dust temperature provides the mobility of radicals formed during this process, which leads to the formation of next-generation molecules. A close protostar's subsequent evolution almost completely evaporates dust mantles to enrich the surrounding gas by surface synthesis products, which then start reacting with each other to form more complex substances.

Although there are detailed theoretical descriptions of various COM formation scenarios in cold gas, none of them is reliable enough because of a scarcity of observational data. There is very little information about COMs' spatial distribution; only a comparison of the COM abundance in the direction of the dust and methanol peak emissions in the pre-stellar core L1544 has been made [285]. Therefore, mapping complex organic molecules in the direction of star-formation regions, searching for their spatial correlations, and testing chemical models are very relevant. COM mapping by ground-based telescopes requires a lot of observation time. The high sensitivity of Millimetron will enable mapping the COM emission towards cold cores. The maps will allow us to clarify physical processes leading to COM formation and constrain the rapidly growing number of their formation theories.

The discovery of transient substances — short-living intermediate gas-phase chemistry products without which it is impossible to form other essential chemicals — can be another important task for the Millimetron space project. As noted above, about 200 substances have been found in the interstellar and circumstellar medium. However, in addition, many hundreds of neutral and ionized components should be included in the chemical models. Transient substances rapidly react, i.e., are rapidly formed and destroyed, so they are found in small numbers, and most of them have not been observed. The discovery of such substances would help in understanding which formation reactions of complex organic molecules prevail in star-forming regions.

So far, the complexity limits of the forming organics have not been established. Presently, the most complex molecule reliably found in molecular clouds is benzonitrile (C_6H_5CN), consisting of 13 atoms [286]. Other examples include propylene oxide (CH_3CHCH_2O) [287], glicolenitrile ($HOCH_2CN$) [288], and cyanomethanimine [289]. Propylene oxide is the first interstellar molecule with chirality. Cyanomethanimine is thought to be the precursor of adenine, one of four nucleotides coding information in the DNA molecule. There have been several claims of discovery in star-forming regions of the simplest amino acid molecule — glycine. Although this discovery is not reliably confirmed, it is clear that there are no fundamental obstacles to the synthesis of amino acids in molecular clouds. Observations of glycine in comets 81P/Wild2 by the STARDUST mission [290] and 67P Churyumov–Gerasimenko by the ROSETTA mission [291] support this idea.

Of particular astrobiological interest may be studies of chiral molecules, which might be a Millimetron breakthrough discovery. Chirality is a feature of the spatial molecular structure when a molecule cannot be identical with its mirror reflection. The importance of chirality for the origin of life stems from the fact that living organisms on Earth contain exclusively one enantiomer (a variant of chiral molecules' spatial structure). Amino acids in living organisms' proteins are the L-conformation enantiomers, while carbohydrates are the D-configuration enantiomers. This feature of living nature is called homochirality.

Complex chiral molecules are formed from more simple substances lacking chirality (achiral molecules). Generally, in this case, in chemical reactions, a so-called racemate, a mixture of equal amounts of L- and D-conformation of the product molecule, should be formed. Presently, the selection mechanism leading to homochirality is unknown. There are grounds to believe that the preferential formation of enantiomers of one type begins already in space. One piece of evidence supporting this hypothesis is the asymmetry of enantiomers of organic molecules found in meteorites. In particular, in the Murchison meteorite, the prevalence of L-conformation over D-conformation of the isovaline amino acid was discovered (the same as in living proteins) [292].

Possible reasons for the prevalence of one conformation over another may be fundamental features in the Universe (parity violation in electroweak interactions) or different

rates of photolysis (synthesis) of chiral molecules by interstellar ultraviolet radiation with left or right circular polarization [293, 294].

Indeed, if the asymmetry of conformation abundance is caused by a polarized interstellar ultraviolet radiation field, it is logical to suppose that it appears already at the early stages of protostellar cloud evolution and can be observed in chiral molecules there. Presently, only one chiral interstellar molecule, the propylene oxide (CH_3CHCH_2O), is known. It was discovered in 2016 [287]. The molecule is detected in the direction of the Sgr B2 complex containing a variety of complex molecules. Unfortunately, the authors of the discovery could not measure the polarimetry of the found propylene oxide emission, so the possible asymmetry of this molecule's conformation abundance in the interstellar medium remains an open issue. Millimetron's unprecedented capabilities make it possible to expect a breakthrough in studies of the appearance of homochirality in the Galaxy.

The evolution of COM abundance during star and planet formation is challenging to study, because the reliable identification of a molecule requires observing a maximal number of lines. However, most submillimeter molecular lines are unavailable for ground-based observations, which are possible only in several transparency windows. The insufficient sensitivity also allows only pointing observations of COMs in individual objects, making it difficult to understand the properties of their evolution. The more complex (by the number of atoms) the molecule, the larger the number of its degrees of freedom and hence radiation transitions. Therefore, on average, the lines of more complex molecules are less intense than those of simple substances. This fact additionally hampers investigating complex organics in space.

Milllimetron observations will solve both these problems. Space observations will allow measurements of much more numerous lines, enabling more reliable COM identification. The high sensitivity enables detecting more complex molecules which have a low abundance (with respect to the H_2 molecule) as a rule. Deuterated and other isotopologues (containing C, N, O) of these molecules are interesting by themselves. The deuterated molecules can also be indicators of the further transport of molecular matter from pre-stellar cores into protoplanetary disks [295]. One of the interesting problems here is the analysis of the evolution of various methanol isotopologues (with the substitution of different H atoms in the molecule by D atoms). This analysis will help explain the difference between the observed and theoretical abundance of CH_3OD and CH_2DOH molecules [296–299].

Observations of organic substances both in protostellar objects and at later stages in protoplanetary disks are significant for the submillimeter observatory. Presently, the list of organic substances discovered in the disks is much shorter than that of interstellar molecules. However, their number is constantly increasing, primarily due to submillimeter ALMA interferometer observations. It is sufficient to mention, for example, the discovery of methyl cyanide (CH_3CN) [300], methanol [301], and formic acid (HCOOH) [302].

Calculations show that organic molecules are mainly found in the solid phase in protoplanetary disks, i.e., in the icy mantles of dust grains. However, they can become visible if some process heats up the dust grains and evaporates their mantles. For example, luminous outbursts observed from objects like Fuors can be such a process. Numerical modeling suggests that disk heating increases the gas-phase content of many organic molecules by many orders of magnitude [303, 304]. High abundances of methanol, acetone, acetonitrile, acetaldehyde, and methyl formate observed in Fuor V 883 Ori [305] support these models.

4.3 Water

Beyond organic substances, submillimeter observations of water molecules in protoplanetary disks are also crucial for the origin and abundance of life. Water plays a unique role in the development of protein life. It is not only a universal solvent. Presumably, for the development and survivability of live organisms on Earth, special water ice and liquid water features were essential.

The search for water in the interstellar medium has been among the main topics of molecular astrophysics for a long time. Water molecular lines excited in a cold gas radiate at frequencies of 500–1700 GHz, unavailable to ground-based instruments due to atmospheric water vapor screening. Therefore, observations of water in cold nuclei have been conducted by space telescopes, most importantly SWAS (Submillimeter Wave Astronomy Satellite) and Herschel [268, 306]. Importantly, water proved crucial in interstellar chemistry processes and is an excellent diagnostic tool of the physics of space objects. In particular, observations of P Cyg profiles of water lines confirmed the beginning of the collapse in the pre-stellar core L1544 [307]. They also enabled measuring the accretion rate in hot cores and envelopes of protostars [308].

Identifying the source of water on Earth is one of the key issues of the Solar System's evolution. The problem is solved by searching for a population of Solar System bodies that possesses a semi-heavy to ordinary water ratio similar to terrestrial oceans. In comets, which were initially thought to be the leading water suppliers on Earth, this ratio proved to be several times as high as in Earth's ocean (the comets Hartly-2 [309] and Virtanen [310] are exceptions). Therefore, the possibility of water being supplied to Earth due to asteroid bombardment is under consideration. In this respect, it would be exciting to trace the HDO and H_2O abundances in other forming planetary systems. So far, such observations are scarce and yield only the upper limits due to low sensitivity [311, 312]. Observations with the existing ground-based and space instruments SMA (Submillimeter Array, a joint project of the Smithsonian Astrophysical Observatory and the Institute of Astronomy and Astrophysics of the Taiwan Academy of Sciences), JCMT (James Clerk Maxwell Telescope), and Herschel have already significantly contributed to these studies. The high submillimeter sensitivity of Millimetron will enable measuring the HDO/H_2O ratio in many objects, offering the opportunity of making statistical generalizations and establishing a possible relationship between semi-heavy water abundance and the protoplanetary disk and host star parameters.

As the Millimetron angular resolution ($\theta = (6-13)''$ at the frequencies of main water lines) is insufficient to resolve a protoplanetary disk, it is possible to probe the origin of water on Earth and Earth-type planets by observing, first of all, different planetary formation stages and, second, various water molecular lines excited under diverse physical conditions. Early evolutionary stages — cold pre-stellar and hot protostellar cores — can be spatially resolved to measure the HDO/H_2O ratio's radial distribution. In protoplanetary disks, the water distribution can be recovered by observing

different water lines. Generally, the central star heats up the inner disk more strongly than its periphery. This results in a higher excitation temperature [15] of water rotational levels T_{ex} in the inner disk than in the outer disk. The width of spectral lines formed in the inner disk should also be significantly higher. This is supported by the Herschel observations (see, for example, [313]) and by numerical simulations [314].

Observations of water isotopologues are also crucial to explore physical conditions at the transitional stage from the pre-stellar core to the protoplanetary disk. Water in the molecular cloud arises before the appearance of a pre-stellar core and continues synthesizing during the evolution of the whole protostellar system. The HDO/H_2O ratio depends on the para- to ortho-hydrogen ratio, which, in turn, depends on the physical conditions in the medium. Thus, the isotope water composition can probe the place and time of its arising.

4.4 Solar System

Far IR observations by the Herschel Space Telescope were a great leap forward in studies of important and fundamental problems of the Solar System's formation, including the water cycle on Mars, water sources in the stratospheres of external giant planets, and isotope ratios in cometary and planetary atmospheres. New observations are required to confirm the presence of water vapor in a torus around Saturn, formed due to water vapor outflows and ice and dust grain expulsion from Enceladus's south pole, in the atmospheres of Jupiter's ice satellites and the dwarf planet Ceres, and in cometary comas. The obtained results posed new questions and are a solid base for future Solar System studies by Millimetron. Complex (prebiotic and biotic) molecules in gas shells of planets, their satellites, and small bodies (comets and asteroids) in the Solar System's outer cold parts radiate in the infrared and submillimeter ranges. Therefore, the Millimetron science program in the single-dish mode with a super-high sensitivity will address the following issues.

- Molecular composition and physical conditions in the atmospheres of giant planets and their satellites. Special attention will be given to studies of Neptune, because Neptune-like planets (hot Neptunes, sub-Neptunes, and ocean planets) are found in many exoplanetary systems.
- Ocean worlds: determining the chemical composition of gas shells and the surfaces of icy satellites of Jupiter and Saturn and estimating chemical exchange between under-ice ocean water and the surface.
- Asteroids and comets: searching for new objects; measuring the emission spectra, reflection properties, and other physical characteristics.
- Interplanetary dust and objects in the Kuiper belt and Oort cloud made of primeval Solar System elements.

Thus, the key Millimetron measurements to understand the Solar System's origin include determining the deuterium to hydrogen ratio, isotopic water composition, and the isotopic ratios of O and N atoms in many asteroids and comets, Jupiter's and Saturn's icy satellites, and Kuiper belt objects.

4.4.1 Ocean worlds in the outer Solar System. There is a diversity of celestial bodies in the cold outer parts of the Solar System. They include Europa, with bizarre surface features; small, geologically active Enceladus; Titan, a unique satellite with a significant atmosphere; and Pluto, with its nitrogen glaciers. In the last 25 years, space observations have shown that many of these celestial bodies are 'ocean worlds' because of a large amount of liquid water under the ice surface. This new group of bodies — ocean worlds — is important for several reasons. The most crucial and simultaneously the most straightforward reason is that they can be habitable. Life as we know it needs liquid water, a chemically diverse and stable medium, and energy sources capable of sustaining homeostasis. All these requirements can be met on some of the above mentioned celestial bodies.

Measurements by the Galileo and Cassini spacecraft confirmed the existence of undersurface oceans on Enceladus, Europa, Titan, Ganymede, and Callisto. Europa and Enceladus are distinguished as ocean worlds by showing the ocean-surface connection and the possibility of interaction between the ocean and rocky core of the satellite. These factors can be important for their potential habitability. Undersurface oceans on Titan, Ganymede, and Callisto are expected to be covered by thick icy layers hampering exchange with the surface and hiding surface signatures of the oceans.

Although Titan has a sizeable under-ice ocean, it also has a surface layer made of diverse organic substances and liquids that are easily accessible and can be inhabited by exotic life forms. Moreover, there can be transient liquid water on Titan's surface in the form of impact-melted water basins and fresh cryovolcanic flows interacting with both solid and liquid organics. These media are unique and essential targets for prebiotic chemistry research and possibly the first steps towards the origin of life [315].

Celestial bodies like Triton, Pluto, Ceres, and Diona are considered candidates for ocean worlds because of sparce space observations. Our knowledge about other celestial bodies like Uranus's satellites is limited. Knowledge of the presence of oceans on them is not reliable, although it is possible. In the following description of observational appearances of ocean worlds in the outer Solar System, we will stick to the classification suggested in recent reviews [316, 317].

The giant planets' satellites with oceans — Europa, Ganymede, Titan, and Enceladus — are the primary targets for Millimetron space observations.

- On Saturn's icy satellites, Enceladus and Titan, under-ice water oceans with highly probable potential habitability were discovered. No space missions to the Saturn system are foreseen in the nearest future. Therefore, super-sensitive Millimetron measurements of the chemical composition of the atmosphere and surface of ocean worlds will be unique to estimate ocean-surface chemical exchange and their potential habitability. In the case of Titan, such observations will help investigate for the first time the complex organic chemistry of the dense atmosphere and carbohydrate lakes and seas discovered on its surface.
- The Jovian icy satellites, Europa and Ganymede, will be explored in the nearest future (after 2030) by the European Space Agency (ESA) JUICE (JUpiter ICy moons Explorer) and NASA's Europa Clipper space missions. Their expected joint observations, along with those from Millimetron, of chemical exchange by complex molecules between the under-ice ocean and surface are very important for assessing the astrobiological potential of these ocean worlds.

Ocean worlds. Enceladus. The most compelling evidence for the presence of an under-ice liquid water ocean in Saturn's satellite system, and perhaps in the whole Solar System, is the

[15] It characterizes the excitation of levels.

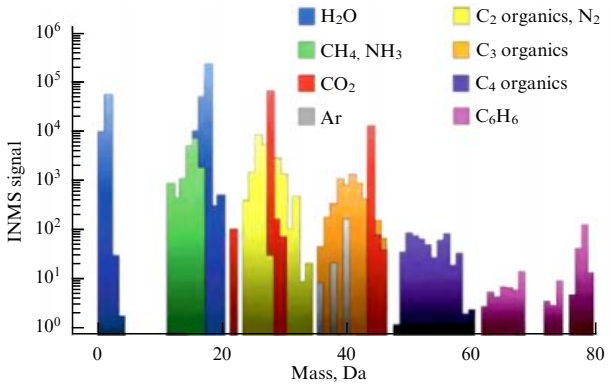

Figure 21. (Color online.) Mass spectrum of the Enceladus trail measured with the ion and neutral mass-spectrometer (INMS) during the NASA Cassini mission passage on October 9, 2008. Colored is the contribution of various chemical substances and possible parts of them. (Figure from paper [320].)

ocean of Saturn's small satellite Enceladus. In 2004, the NASA Cassini mission discovered gas and dust trails emanating from Enceladus's south pole. The satellite density suggests that it consists of a mixture of rocky formations and ice with stones. Its bright icy surface most likely indicates that its silicate core is separated from the ice crust by a liquid water layer. During its last and deepest flight through the trail on 28 October 2015, the Cassini spacecraft discovered water molecules in the gas and ice plume ejected by geysers at Enceladus's south pole. The Cassini apparatus also measured the plume composition during the first flight through it. These observations showed that almost 98% of the plume gas consists of water molecules, 1% is hydrogen, and the rest is a mixture of other molecules, including those containing carbon [318, 319].

The chemical composition of Enceladus's south pole geyser ejecta measured by the Cassini INMS mass-spectrometer (Fig. 21), especially the complex carbon organics that were not resolved in the Cassini observations, can be determined from Millimetron observations of the geyser ejecta.

Ocean worlds. Titan. Titan represents an almost equal mixture of rocks and water ice. It is the only natural satellite with a thick atmosphere, which, near its surface, is about four times as dense as the terrestrial atmosphere at sea level. Titan's atmosphere primarily consists of molecular nitrogen, like Earth's atmosphere. The very faint solar radiation at the remote Saturn orbit can sustain a very low surface temperature, 94 K at the equator, even with a modest greenhouse effect, suggesting that the atmospheric water freezes out. In turn, methane serves as a weather driver: the NASA Cassini observations made by the Huygens lander on the surface of Titan discovered clouds, rain, surface dew, ravines, and river valleys [321, 322].

The NASA Cassini mission discovered high latitude lakes and seas on Titan, mainly close to its northern pole. Radiolocation data showed that these liquid reservoirs mainly consist of methane with a small ethane and nitrogen admixture [322]. Whether exotic life forms can arise and survive in these reservoirs remains an open question [315]. However, the Cassini and Huygens probe measurements found evidence of a much warmer liquid water ocean deep under the surface [323]. The Millimetron observations of Titan's atmosphere and the surface's complex chemical composition can shed new light on Titan's astrobiology.

Galilean satellites of Jupiter. Observations suggest that internal liquid water oceans can be present on three of the four large Galilean Jovian satellites. The most compelling evidence was found for Europa [324]. The exterior of Europa's surface imaged by the NASA Voyager spacecraft suggests the possible prevalence of a liquid layer beneath the ice crust. Unlike many other satellites, including the Moon, a small number of craters are found on Europa's surface. Images taken by the NASA Voyager and Galileo spacecraft show that most of its surface is heavily cracked. Apparently, in some regions, the ice crust blocks were separated and rotated in sludge ice or liquid water. Presently, the satellite's full surface is frozen, but its geological features are consistent with the possible existence of liquid water under the ice presently or in the recent past. The NASA Galileo mission's spectral measurements of the surface were noisy due to intense radiation produced by Jupiter's magnetic field. Nevertheless, there is evidence of salt spots on the surface [325] corresponding to the recent ejection of liquid water from the satellite interiors [336]. In order to sustain the bulk of the liquid ocean, as inferred from NASA Galileo mission measurements [327], the energy should be tapped from Europa's orbital motion by tidal dissipation. Commensurate orbital periods of Io, Europa, and Ganymede around Jupiter suggest that Europa's orbital eccentricity will be maintained for long geological periods, while the tidal capture energy circularizes the satellite's orbit [328].

Unlike Europa, for which there are two independent pieces of evidence of a liquid ocean under the surface, only one type of observation suggested oceans on Ganymede and Callisto. In the case of Callisto, the evidence was found from measurements of Jupiter's magnetic field fluctuations by the magnetometer aboard the NASA Galileo mission, which are, however, weaker than perturbations produced by Europa [329]. Regarding Ganymede, the situation is more complicated, because it has its own magnetic field produced by the internal dynamo in the metallic core. This hampers reliable measurements of the Ganymede-induced Jovian field, although Jupiter's magnetic field fluctuations near Ganymede were found; other explanations are also possible [330]. The presence of an ocean on Ganymede was supported by observations of weak auroral polar glows on Ganymede with the Hubble Space Telescope. The glows turned out to be more stable in Jupiter's magnetic field than in the absence of a subsurface conductor partially screening the external field [331]. Ganymede's and Callisto's surfaces have a great number of impact craters. Considering that a thick and cold ice crust is required to sustain ancient craters, it is possible to conclude that Ganymede's and Callisto's oceans are located deep under the surface, likely at a depth exceeding 100 km. As both these satellites are more massive than Europa and have a comparable amount of ice and rock, some proportion of the ice should be in the high-pressure phase, which is denser than liquid water. Thus, their oceans are most likely squeezed between the upper and bottom ice layers, making contact with the central silicate core (which is thought to be essential for generating life) highly improbable.

The Hubble Space Telescope observations discovered water vapor plumes near Europa's south pole [326], suggesting cryovolcanic activity or a change in the surface tensions, depending on Europa's orbital phase. The Herschel/HIFI (Heterodyne Instrument for the Far Infrared) observations detected asymmetric water vapor atmospheres on Ganymede and Callisto [332]. Spraying, sublimation, or unknown sur-

face processes are their potential sources. Correspondingly, Millimetron observations offer the opportunity to monitor the space-time evolution of these water vapor atmospheres/trails, relate them in more detail with orbital phases, and possibly determine their sources and absorbers.

Astrobiological potential of ocean worlds. During close flybys of the NASA Cassini mission, the ion and neutron mass-spectrometer (INMS) discovered the presence of organic and nitrogen-containing molecules in the vapor trail of Enceladus [318, 320] (see Fig. 21). In the trail's ice grains, the cosmic dust analyzer (CDA) revealed traces of salts [333]. These measurements suggested contact between the ocean water and a rocky core [320, 334]. This conclusion was additionally supported by the recent discovery of dust silicate grains with characteristic sizes from 2 to 8 nm in the Enceladus trail. Laboratory modeling showed that such nanoparticles could only result from hydrothermal reactions with a high constant temperature (> 90 °C) in the ocean [333]. The composition of the silicate grains from Enceladus's geysers suggests that its ocean has existed since the birth of the Solar System or that molecular hydrogen is constantly created in its interiors, being likely the potential energy source for the ocean water [335]. Recently, active hydrothermal reactions in Enceladus's rocky core containing minerals and organic substances were confirmed as the most plausible molecular hydrogen source [319]. A relatively high density of hydrogen in the plume suggests a thermodynamic nonequilibrium in the salt-saturated ocean, which, notably, helps to form methane from carbon dioxide in the ocean of Enceladus. Sustaining the nonequilibrium H_2 concentration in the ocean requires a permanent energy source, for example, from hydrothermal reactions.

The main volatiles ejected by Enceladus's geysers include water vapor, H_2O, 96–99%, carbon dioxide, CO_2, 0.3–0.8%, methane, CH_4, 0.1–0.3%, ammonia, NH_3, 0.4–1.3%, and molecular hydrogen, H_2, 0.4–1.4% [318–320]. Also, traces of carbon monoxide, CO, acetylene, C_2H_2, ethylene, C_2H_4, ethane, C_2H_6, molecular nitrogen, N_2, hydrogen cyanide, HCN, formaldehyde, CH_2O, and nitrogen oxide, NO were found. Their content varies from 0.2% to 100 ppm [16] (parts per million, 0.01%). In addition, 33 species with an abundance of below 100 ppm, producing too low a signal to be reliably detected (so-called 'mass noise'), were reported. As a rule, these are sufficiently complex, various organic substances, as well as molecular oxygen, O_2, argon, Ar, hydrogen sulfide, H_2S, and phosphine, PH_3. Should their presence be confirmed, the under-ice ocean of Enceladus will have all necessary chemical elements for the existence of life.

The Millimetron Space Observatory can measure many more lines of complex molecules, rendering their identification more reliable. Moreover, the high sensitivity of Millimetron gives hope to discovering biotic molecules in gas shells and on the surface of icy satellites — worlds with an ocean. Observations of deuterated isotopologues of simple and complex molecules in the Solar System's cold outer parts are critical, because deuterated molecules are indicators of the transfer of volatiles between the planetary system's inner and outer parts.

4.4.2 Asteroids, comets and Kuiper Belt objects. Recent Herschel/HIFI observations of water plumes near the dwarf planet Ceres's surface in the main asteroid belt with a production rate of about 6 kg s^{-1} suggest their possible cryovolcanic origin [336]. The presence and abundance of water on asteroids are important for many Solar System studies, including the origin of water and life on Earth and the large-scale migration of Jupiter-like giant planets. Long (~ 10 hr) observations of Ceres discovered two presumably active regions on its surface. The water production rate sensitivity in these observations was about one kg s^{-1}. The Millimetron instruments' planned parameters will increase the sensitivity to 100 g s^{-1} or less, depending on the observed water molecule transition. This high sensitivity opens new prospects in asteroid studies. Indeed, a recent analysis of the Dawn space mission to the dwarf planet Ceres [337] shows that, deep under the Occator crater, there is a vast saltwater reservoir. Presumably, the impact of a celestial body that created Occator could have caused the saltwater to rise to the surface. Water ejections can be discovered on other asteroids, for example, on carbonaceous chondrites or comets from the main asteroid belt. Water vapor sublimation, among other reasons, may be responsible for the creation of the observed dust comas of the main asteroid belt comets. However, so far, all attempts to discover water on these comets have failed [338] due to the restricted sensitivity of previous observations, including those by Herschel/HIFI.

Kuiper Belt objects (KBOs) are the best-preserved remnants from the Solar System's formation. They keep information on the protoplanetary disk's chemistry and physical processes that led to the planet formation. The fundamental characteristic of KBOs, their size, is hard to measure from the ground. Due to the large distances from the Sun, most KBOs are unresolved, and their brightness is degenerate because of the unknown sizes and albedos. KBO parameter distributions are useful for their formation and destruction studies. Very little is known about these bodies' internal structure, whose size varies from Pluto and Eris (with a diameter of about 2300 km) to objects of less than 100 km. In 2015, the New Horizon space mission visited Pluto and its satellite Charon and discovered different geological features on their surfaces, evidencing internal activity. In Pluto's case, various molecules, like carbon monoxide and nitrogen, are 'pumped out' of the interior and presently exist in the form of surface snow depositions [339]. Thermal models of these relatively rock-rich bodies combined with evidence of their geological activity may suggest the presence of internal liquid water.

Calculations of the sizes and albedos of unresolved small bodies are the most fundamental application of thermal observations in Solar System astronomy. However, much better can be achieved in the submillimeter range. Millimetron's capabilities will enable the detection and measurement of Rayleigh–Jeans thermal radiation from hundreds of KBOs. In this limit, the radiation flux is almost proportional to the instant cross section of the object. It very weakly depends on other poorly known parameters, such as the IR-emissivity and surface temperature distribution. Such KBO measurements will provide a reliable, unbiased estimate of the KBO size distribution. Precise albedos are also crucial for spectral modeling of KBO surfaces [340]. The Millimetron sensitivity is two orders of magnitude higher than that of the Herschel Space Telescope. Therefore, this is very prospective research, considering the significant progress in KBO studies provided by the Herschel observations (see, for example, [341]). Millimetron offers the exciting prospect of discovering

[16] For such small fractions, it is convenient to use the widely accepted designation "parts per million" (ppm).

thermal radiation from more than 1000 presently known KBOs and new objects that will be found before its launch. Measurements of the albedo and size of thousands of bodies will provide a great deal of observational data for comparative planetology. In addition, Millimetron will measure the spectral energy distribution of KBOs, which can be done using very detailed thermophysical models allowing for the spin state, thermal inertia, and infrared emission effects. For example, high surface thermal inertia usually points to a porous, regolith-covered surface, and enhanced IR flux suggests a cratered surface [342]. It is interesting to understand the dependence of these properties on the KBO size. The spectroscopic capabilities of Millimetron enable us to search for long-wavelength features of icy and mineral surface structures on KBOs, which are more pronounced and more reliable at long wavelengths than at short wavelengths. Presently, only several of the brightest KBOs can be successfully probed by visible optical and near IR observations. Little information about the KBO surface is based on broadband photometry. Millimetron observations will enable the surface mapping of small bodies across the Solar System's entire outskirts. The relatively unexplored millimeter wavelength range can also bring novel discoveries.

Neptune's satellite Triton revolves in a retrograde orbit, suggesting that it was captured from the Kuiper belt in the early Solar System. On Triton, which is larger than Pluto by several hundred kilometers, nitrogen geysers were discovered in images taken by the Voyager-2 space mission in 1989. So far, their origin is thought to be from the heating of relatively transparent ice by solar radiation [343], but they also possibly suggest interior activity of the satellite. Therefore, as on Pluto, indirect geological facts, combined with internal structure models [344], point to the possible presence of an undersurface ocean. Millimetron observations will offer a unique possibility of discovering and investigating simple and complex molecules in gas shells and on the surface of many of these Kuiper Belt objects. They will enable us to understand better the formation and evolution of the residual (fragmentation) disk in the Solar System.

Studies of water vapor excitation in the cold outer parts of the Solar System at low temperatures of 10–100 K can be successfully continued only with Millimetron space observations. Studies of water and its isotopologues in Solar System bodies [345–347] will yield basic information on their structure and evolution. The most crucial parameter, in particular, is the deuterium-to-hydrogen ratio (D/H) (Fig. 22) measured for water. Laboratory experiments confirmed by interstellar medium observations suggest that deuterium is enriched in ice due to gas-molecular reactions and reactions on dust grain surfaces at low temperatures. The D/H ratio for Solar System objects (see Fig. 22) yields information about the physical-chemical conditions of water formation and water mixture processes in comet ice, depending on the D/H ratio, which increases with the heliocentric distance. This ratio may also shed light on the formation of external planets and thermal evaporation of Earth-like planets' atmospheres. Observations show that the D/H ratio in six comets from the Oort cloud is, on average, two times as high as the isotopic composition of VSMOW (Vienna Standard Mean Ocean Water), which rules out comets as the external water suppliers of Earth. The Herschel/HIFI observations measured for the first time the D/H ratio in a Jupiter-family comet (103P/Hartley 2), in agreement with VSWOM [309]. The Herschel/HIFI observations and observations [348] of the Jupiter-family comet 45P Honda-Mrkos-Pajdusakova confirmed the low D/H ratio (Fig. 23). Therefore, D/H measurements for a larger number of comets will be invaluable for learning about the Solar System's formation. The determination of the deuterium-to-hydrogen and other essential isotopic ratios by Millimetron can be crucial to understanding this formation. Observations of water ejections from active asteroids will bring information on the main asteroid belt's water content, vital for future missions to asteroids.

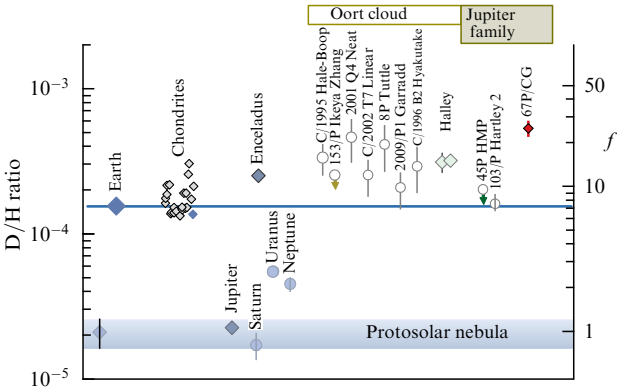

Figure 22. (Color online.) Deuterium to hydrogen ratio for planets and small bodies of the Solar System. Diamonds show direct measurements by different missions. Circles show data obtained by astronomical methods. Dark blue and blue lines show the D/H ratio in Earth's ocean and protosolar nebula, respectively. (Figure from paper [346].)

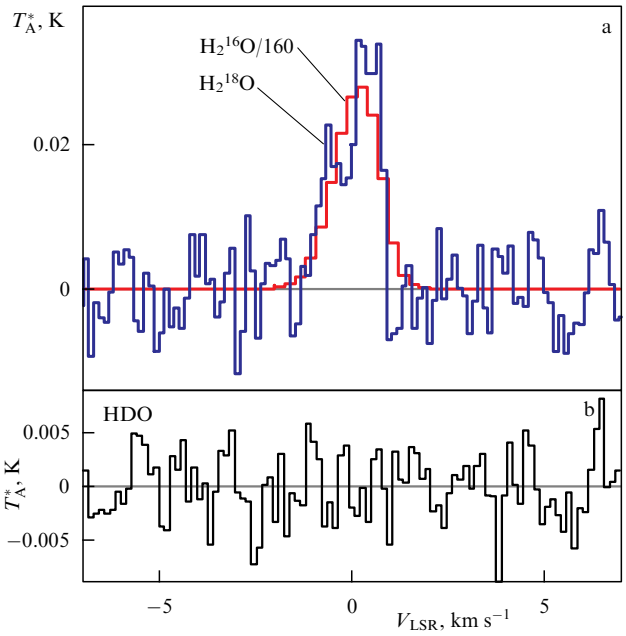

Figure 23. (Color online.) (a) Herschel/HIFI measurements of the $1_{10}-1_{01}$ transition for isotopologues $H_2^{18}O$ (blue line) and $H_2^{16}O$ (red line) of the water molecule in the coma of comet 45P. (b) Spectrum of the transition $1_{10}-1_{01}$ of the HDO molecule. (Figure from paper [348].)

Space measurements showed that many of the outer Solar System's bodies are ocean worlds hiding big reservoirs of liquid water under icy surfaces. It is crucial to understand their characteristics and ways of chemical exchange by complex molecules among the under-ice ocean, surface, and gas atmosphere [349–351]. Unique Millimetron observations of chemical exchange by complex molecules between the

under-ice ocean and surface in ocean worlds seem to be critical to assess their astrobiological potential and search for life in the Solar System.

5. Conclusion

• Three factors determine the uniqueness of the Millimetron space observatory: 1) it will be able to carry out broadband observations in the wavelength range from 50 μm to 10 mm, 2) it will have an unprecedentedly high angular resolution, and 3) it will have a sensitivity unavailable earlier in this energy range.

• In the single-dish mode, the Millimetron space observatory will be able to measure y- and μ-CMB spectral distortions caused by very early energy release in the Universe starting from $z \sim 2 \times 10^6$. This will open a new information channel for cosmological observations of the early Universe unavailable so far.

• Joint Millimetron, ALMA, and EHT observations can obtain fundamental results on the space-time geometry and plasma properties in strong gravitational fields around the black holes Sgr A* and M87* with a spatial resolution at least an order of magnitude higher than their Schwarzschild radii; for M87, the time resolution will be an order of magnitude shorter than the Schwarzschild time.

• The Millimetron space observatory will investigate energy sources and physical processes in the dusty, optically thick regions of active galactic nuclei, as well as in the central parts of nearby and distant ($z \gtrsim 7$) IR-bright galaxies.

• The Millimetron Space Observatory will unveil the mystery of the origin of supermassive ($M_\bullet \gtrsim 10^9 M_\odot$) black holes in the young (pre-reionization) Universe.

• The high-resolution spectroscopy ($R \gtrsim 10^5$) and high sensitivity of the Millimetron instruments will be crucial to the molecular analysis of interstellar clouds harboring nests of young stars and planetary systems. This will increase the complexity limit of organic molecules in the interstellar medium and possibly shed light on the origin of Earth's life chirality.

• Spectral and photometrical observations of protoplanetary disks by Millimertron will enable a detailed analysis of the dynamics of the origin and growth of planetesimals and protoplanets and water transportation into habitable zones.

• The Millimetron Space Observatory will provide new opportunities to observe the chemical exchange between different phases in ocean worlds in the Solar System.

We appreciate the referees for their critical notes. The study was partially supported by the project "New Scientific Groups of LPI", no. 41-2020. AP thanks the RSF for its support (project 19-72-00064). AB is supported by RSF grant 18-12-00351 and by the State Target FEUZ-2020-0038. The work by IZ (Section 4) is supported by RFBR grant 18-02-00660. DV was supported by a grant from the Russian Government and Ministry of Higher Education and Science, 075-15-2020-780 (no. 13.1902.21.0039). The work by VSh (Section 4.4) was supported by a grant from the Russian Government for research by leading scientists under the program "Studies of Stars with Exoplanets" (agreement 075-15-2019-1875).

Note added in proof

Very recently, based on a sample of 1938 active galactic nuclei in the northern sky with an 8 GHz flux above 0.33 Jy, paper [352] reported a clear relation between TeV–PeV neutrino events and blazars.

References

1. Kardashev N S et al. *Tr. Fiz. Inst. im. P N Lebedeva Ross. Akad. Nauk* **228** 112 (2000)
2. Smirnov A V et al. *Proc. SPIE* **8442** 84424C (2012)
3. Kardashev N S et al. *Phys. Usp.* **57** 1199 (2014); *Usp. Fiz. Nauk* **184** 1319 (2014)
4. Spergel D N et al. *Astrophys. J. Suppl.* **170** 377 (2007)
5. Nolta M R et al. *Astrophys. J. Suppl.* **180** 296 (2009)
6. Ade P A R et al. (Planck Collab.) *Astron. Astrophys.* **594** A13 (2016)
7. Perlmutter S et al. *Astrophys. J.* **517** 565 (1999)
8. Goobar A et al. *Physica Scr.* (T85) 47 (2000)
9. Oesch P A et al. *Astrophys. J.* **819** 129 (2016)
10. Lo Faro B et al. *Astrophys. J.* **762** 108 (2013)
11. Thacker C et al. *Astrophys. J.* **811** 125 (2015)
12. Baganoff F K et al. *Nature* **413** 45 (2001)
13. Sun M et al. *Astrophys. J.* **565** 867 (2002)
14. Bregman J N et al. *Astrophys. J.* **699** 1765 (2009)
15. Abbott B P et al. (LIGO Scientific Collab. and Virgo Collab.) *Phys. Rev. Lett.* **116** 061102 (2016)
16. Verkhodanov O V *Phys. Usp.* **59** 3 (2016); *Usp. Fiz. Nauk* **186** 3 (2016)
17. Akiyama K et al. (Event Horizon Telescope Collab.) *Astrophys. J. Lett.* **875** L1 (2019)
18. Akiyama K et al. (Event Horizon Telescope Collab.) *Astrophys. J. Lett.* **875** L2 (2019)
19. Akiyama K et al. (Event Horizon Telescope Collab.) *Astrophys. J. Lett.* **875** L3 (2019)
20. Akiyama K et al. (Event Horizon Telescope Collab.) *Astrophys. J. Lett.* **875** L5 (2019)
21. Shchekinov Yu A, Lukash V N, Mikheeva E V, Pilipenko S V *Phys. Usp.* **60** 961 (2017); *Usp. Fiz. Nauk* **187** 1033 (2017)
22. Shaykhutdinov A R, Kostenko V I *Cosmic Res.* **58** 393 (2020); *Kosmich. Issled.* **58** 434 (2020)
23. Andrianov A S et al. *Mon. Not. R. Astron. Soc.* **500** 4866 (2021)
24. Thompson A R, Moran J M, Swenson G W (Jr.) *Interferometry and Synthesis in Radio Astronomy* 3rd ed. (Cham: Springer Intern. Publ., 2017)
25. Johnson M D *Astrophys. J.* **833** 74 (2016)
26. Kovalenko I D, Eismont N A *Astron. Lett.* **44** 289 (2018); *Pis'ma Astron. Zh.* **44** 307 (2018)
27. Mather J C et al. *Astrophys. J. Lett.* **354** L37 (1990)
28. Zeldovich Ya B, Sunyaev R A *Astrophys. Space Sci.* **4** 301 (1969)
29. Illarionov A F, Syunyaev R A *Sov. Astron.* **18** 691 (1975); *Astron. Zh.* **51** 1162 (1974)
30. Burigana C, Danese L, de Zotti G *Astron. Astrophys.* **246** 49 (1991)
31. Hu W, Silk J *Phys. Rev. D* **48** 485 (1993)
32. Chluba J *Mon. Not. R. Astron. Soc.* **454** 4182 (2015)
33. Hu W, Scott D, Silk J *Phys. Rev. D* **49** 648 (1994)
34. Hill J C et al. *Phys. Rev. Lett.* **115** 261301 (2015)
35. Carr B J et al. *Phys. Rev. D* **81** 104019 (2010)
36. Hu W, Silk J *Phys. Rev. Lett.* **70** 2661 (1993)
37. Hu W, Scott D, Silk J *Astrophys. J. Lett.* **430** L5 (1994)
38. Daly R A *Astrophys. J.* **371** 14 (1991)
39. Kompaneets A S *Sov. Phys. JETP* **4** 730 (1957); *Zh. Eksp. Teor. Fiz.* **31** 876 (1956)
40. Sunyaev R A, Zeldovich Ya B *Astrophys. Space Sci.* **7** 20 (1970)
41. Abitbol M H et al. *Mon. Not. R. Astron. Soc.* **471** 1126 (2017)
42. Challinor A, Lasenby A *Astrophys. J.* **499** 1 (1998)
43. Ade P A R et al. (Planck Collab.) *Astron. Astrophys.* **594** A27 (2016)
44. Kogut A et al. *JCAP* **2011** (07) 025 (2011)
45. Ade P A R et al. (Planck Collab.) *Astron. Astrophys.* **576** A104 (2015)
46. Adam R et al. (Planck Collab.) *Astron. Astrophys.* **594** A10 (2016)
47. Lamarre J M *Appl. Opt.* **25** 870 (1986)
48. de Bernardis P et al. *Astron. Astrophys.* **538** A86 (2012)
49. Aghanim N et al. (Planck Collab.) *Astron. Astrophys.* **641** A6 (2020)
50. Riess A G et al. *Astrophys. J.* **876** 85 (2019)
51. Alam S et al. *Mon. Not. R. Astron. Soc.* **470** 2617 (2017)
52. Freedman W L et al. *Astrophys. J.* **882** 34 (2019)
53. Gao F et al. *Astrophys. J.* **817** 128 (2016)
54. Reid M J et al. *Astrophys. J.* **767** 154 (2013)
55. Kuo C Y et al. *Astrophys. J.* **800** 26 (2015)

56. Refsdal S *Mon. Not. R. Astron. Soc.* **128** 307 (1964)
57. Larchenkova T I, Lyskova N S, Lutovinov A A *Astron. Lett.* **37** 441 (2011); *Pis'ma Astron. Zh.* **37** 483 (2011)
58. Suyu S H et al. *Astrophys. J. Lett.* **788** L35 (2014)
59. Wong K C et al. *Mon. Not. R. Astron. Soc.* **498** 1420 (2020)
60. Abbott T M C et al. (The Dark Energy Survey and the South Pole Telescope Collab.) *Mon. Not. R. Astron. Soc.* **480** 3879 (2018)
61. Di Valentino E, Melchiorri A, Silk J *Nat. Astron.* **4** 196 (2020)
62. Larchenkova T I, Ermash A A, Doroshkevich A G *Astron. Lett.* **45** 821 (2019); *Pis'ma Astron. Zh.* **45** 866 (2019)
63. Kakiichi K et al. *Mon. Not. R. Astron. Soc.* **463** 4019 (2016)
64. Konno A et al. *Publ. Astron. Soc. Jpn.* **70** S16 (2018)
65. Naab T, Ostriker J P *Annu. Rev. Astron. Astrophys.* **55** 59 (2017)
66. McQuinn M *Annu. Rev. Astron. Astrophys.* **54** 313 (2016)
67. Bullock J S, Boylan-Kolchin M *Annu. Rev. Astron. Astrophys.* **55** 343 (2017)
68. Wechsler R H, Tinker J L *Annu. Rev. Astron. Astrophys.* **56** 435 (2018)
69. Weisz D R et al. *Astrophys. J.* **789** 148 (2014)
70. Vieira J D et al. *Nature* **495** 344 (2013)
71. Dowell C D et al. *Astrophys. J.* **780** 75 (2014)
72. Hezaveh Y D et al. *Astrophys. J.* **767** 132 (2013)
73. Bouwens R J et al. *Astrophys. J.* **670** 928 (2007)
74. Bouwens R J et al. *Nature* **469** 504 (2011)
75. Ellis R S et al. *Astrophys. J. Lett.* **763** L7 (2013)
76. Bouchet P et al. *Publ. Astron. Soc. Pacific* **127** 612 (2015)
77. Senarath M R et al. *Astrophys. J. Lett.* **869** L26 (2018)
78. Laursen P et al. *Astron. Astrophys.* **627** A84 (2019)
79. Stark D P et al. *Mon. Not. R. Astron. Soc.* **464** 469 (2017)
80. Songaila A et al. *Astrophys. J.* **859** 91 (2018)
81. Matthee J et al. *Astron. Astrophys.* **619** A136 (2018)
82. Konno A et al. *Astrophys. J.* **797** 16 (2014)
83. Hu W et al. *Astrophys. J.* **886** 90 (2019)
84. Mesinger A et al. *Mon. Not. R. Astron. Soc.* **446** 566 (2015)
85. Choudhury T R et al. *Mon. Not. R. Astron. Soc.* **452** 261 (2015)
86. Pacucci F et al. *Mon. Not. R. Astron. Soc.* **459** 1432 (2016)
87. Natarajan P et al. *Astrophys. J.* **838** 117 (2017)
88. Barrow K S S, Aykutalp A, Wise J H *Nat. Astron.* **2** 987 (2018)
89. Roberts-Borsani G W et al. *Astrophys. J.* **823** 143 (2016)
90. Bouwens R J et al. *Astrophys. J.* **803** 34 (2015)
91. Oke J B, Gunn J E *Astrophys. J.* **266** 713 (1983)
92. Robertson B E et al. *Astrophys. J. Lett.* **802** L19 (2015)
93. Bouwens R J et al. *Astrophys. J.* **830** 67 (2016)
94. Miley G, De Breuck C *Astron. Astrophys. Rev.* **15** 67 (2008)
95. Mellema G et al. *Exp. Astron.* **36** 235 (2013)
96. Overzier R A *Astron. Astrophys. Rev.* **24** 14 (2016)
97. Harikane Y et al. *Astrophys. J.* **883** 142 (2019)
98. Cantalupo S, in *Gas Accretion onto Galaxies* (Astrophysics and Space Science Library, Vol. 430, Eds A Fox, R Davé) (Cham: Springer, 2017) p. 195
99. Garel T et al. *Mon. Not. R. Astron. Soc.* **422** 310 (2012)
100. Sarkar A, Samui S *Publ. Astron. Soc. Pacific* **131** 074101 (2019)
101. Geach J E et al. *Astrophys. J.* **832** 37 (2016)
102. Ono Y et al. *Astrophys. J.* **795** 5 (2014)
103. Decarli R et al. *Astrophys. J.* **882** 138 (2019)
104. Lam D et al., arXiv:1903.08177
105. Mahler G et al. *Astrophys. J.* **873** 96 (2019)
106. Hashimoto T et al. *Nature* **557** 392 (2018)
107. Shibuya T et al. *Publ. Astron. Soc. Jpn.* **70** S15 (2018)
108. Coe D et al. *Astrophys. J.* **884** 85 (2019)
109. Hao C-N et al. *Astrophys. J.* **864** 145 (2018)
110. Franx M et al. *Astrophys. J.* **486** L75 (1997)
111. Watson D et al. *Nature* **519** 327 (2015)
112. Boogaard L A et al. *Astrophys. J.* **882** 140 (2019)
113. Aravena M et al. *Astrophys. J.* **882** 136 (2019)
114. Laporte N et al. *Astrophys. J. Lett.* **837** L21 (2017)
115. Tamura Y et al. *Astrophys. J.* **874** 27 (2019)
116. Hashimoto T et al. *Publ. Astron. Soc. Jpn.* **71** 71 (2019)
117. Marrone D P et al. *Nature* **553** 51 (2018)
118. Smit R et al. *Nature* **553** 178 (2018)
119. Casey C M, Narayanan D, Cooray A *Phys. Rep.* **541** 45 (2014)
120. U V et al. *Astrophys. J. Suppl.* **203** 9 (2012)
121. Polletta M et al. *Astrophys. J.* **663** 81 (2007)
122. Tsai C-W et al. *Astrophys. J.* **805** 90 (2015)
123. Gilli R, Comastri A, Hasinger G *Astron. Astrophys.* **463** 79 (2007)
124. Gruppioni C et al. *Mon. Not. R. Astron. Soc.* **432** 23 (2013)
125. Venemans B P et al. *Astrophys. J. Lett.* **801** L11 (2015)
126. Jiang L et al. *Astrophys. J.* **833** 222 (2016)
127. Bañados E et al. *Astrophys. J. Suppl.* **227** 11 (2016)
128. Reed S L et al. *Mon. Not. R. Astron. Soc.* **468** 4702 (2017)
129. Matsuoka Y et al. *Astrophys. J.* **869** 150 (2018)
130. Mortlock D J et al. *Nature* **474** 616 (2011)
131. Bañados E et al. *Nature* **553** 473 (2018)
132. Wang F et al. *Astrophys. J.* **884** 30 (2019)
133. Yang J et al. *Astron. J.* **157** 236 (2019)
134. Matsuoka Y et al. *Astrophys. J. Lett.* **872** L2 (2019)
135. Kormendy J, Richstone D *Annu. Rev. Astron. Astrophys.* **33** 581 (1995)
136. Marconi A, Hunt L K *Astrophys. J. Lett.* **589** L21 (2003)
137. Ferrarese L, Ford H *Space Sci. Rev.* **116** 523 (2005)
138. Kormendy J, Ho L C *Annu. Rev. Astron. Astrophys.* **51** 511 (2013)
139. Bullock J S et al. *Mon. Not. R. Astron. Soc.* **321** 559 (2001)
140. Heckman T M, Best P N *Annu. Rev. Astron. Astrophys.* **52** 589 (2014)
141. Decarli R et al. *Astrophys. J.* **854** 97 (2018)
142. Wu X-B et al. *Nature* **518** 512 (2015)
143. Dijkstra M *Saas-Fee Adv. Course* **46** 1 (2019)
144. Vasiliev E O, Shchekinov Y A *Astrophys. J.* **887** 174 (2019)
145. Agarwal B et al. *Mon. Not. R. Astron. Soc.* **432** 3438 (2013)
146. Ferrara A et al. *Mon. Not. R. Astron. Soc.* **443** 2410 (2014)
147. Alexander T, Natarajan P *Science* **345** 1330 (2014)
148. Novikov I D, Thorne K "Astrophysics of black holes", in *Black Holes* (Eds C de Witt, B S de Witt) (New York: Gordon and Breach, 1973) p. 343
149. Bouwens R J et al. *Astrophys. J.* **880** 25 (2019)
150. Schwarzschild K *Sitzungsber. Königlich Preuß. Akad. Wiss. Berlin* 189 (1916)
151. Bisnovatyi-Kogan G S, Blinnikov S I *Sov. Astron. Lett.* **2** 191 (1976); *Pis'ma Astron. Zh.* **2** 489 (1976)
152. Oda M *Space Sci. Rev.* **20** 757 (1977)
153. Bardeen J M, in *Black Holes* (Eds C de Witt, B S de Witt) (New York: Gordon and Breach, 1973) p. 215
154. Luminet J-P *Astron. Astrophys.* **75** 228 (1979)
155. Johnson M D et al. *Sci. Adv.* **6** eaaz1310 (2020)
156. Johannsen T, Psaltis D *Astrophys. J.* **718** 446 (2010)
157. Falcke H, Markoff S B *Class. Quantum Grav.* **30** 244003 (2013)
158. Kamruddin A B, Dexter J *Mon. Not. R. Astron. Soc.* **434** 765 (2013)
159. Goddi C et al. *Int. J. Mod. Phys. D* **26** 1730001 (2017)
160. Dokuchaev V I, Nazarova N O *Phys. Usp.* **63** 583 (2020); *Usp. Fiz. Nauk* **190** 627 (2020)
161. Dokuchaev V I, Nazarova N O *Universe* **6** 154 (2020)
162. Gralla S E *Phys. Rev. D* **102** 044017 (2020)
163. Genzel R, Eisenhauer F, Gillessen S *Rev. Mod. Phys.* **82** 3121 (2010)
164. Kormendy J *Astrophys. J.* **325** 128 (1988)
165. Dressler A, Richstone D O *Astrophys. J.* **324** 701 (1988)
166. Garcia M R et al. *Astrophys. J.* **710** 755 (2010)
167. Gebhardt K et al. *Astrophys. J.* **729** 119 (2011)
168. Walsh J L et al. *Astrophys. J.* **770** 86 (2013)
169. Broderick A E et al. *Astrophys. J.* **805** 179 (2015)
170. Magorrian J et al. *Astrophys. J.* **115** 2285 (1998)
171. López-Cruz O et al. *Astrophys. J. Lett.* **795** L31 (2014)
172. Bonfini P, Dullo B T, Graham A W *Astrophys. J.* **807** 136 (2015)
173. Hogan M T et al. *Mon. Not. R. Astron. Soc.* **453** 1201 (2015)
174. Koss M et al. *Astrophys. J.* **850** 74 (2017)
175. Falcke H, Melia F, Agol E *Astrophys. J. Lett.* **528** L13 (2000)
176. Genzel R, Townes C H *Annu. Rev. Astron. Astrophys.* **25** 377 (1987)
177. Melia F, Falcke H *Annu. Rev. Astron. Astrophys.* **39** 309 (2001)
178. Ghez A M et al. *Astrophys. J.* **689** 1044 (2008)
179. Roy S, Pramesh Rao A *Mon. Not. R. Astron. Soc.* **349** L25 (2004)
180. Dibi S et al. *Mon. Not. R. Astron. Soc.* **441** 1005 (2014)
181. Falcke H et al. *Astrophys. J.* **499** 731 (1998)
182. Yuan F, Quataert E, Narayan R *Astrophys. J.* **606** 894 (2004)
183. Lu R-S et al. *Astron. Astrophys.* **525** A76 (2011)
184. Falcke H, in *Proc. of the 169th Symp. of the Intern. Astronomical Union, The Hague, The Netherlands, August 23–29, 1994* (Eds L Blitz, P Teuben) (Dordrecht: Kluwer, 1996) p. 169; astro-ph/9411065

185. Chan C-K t al. *Astrophys. J.* **799** 1 (2015)
186. Younsi Z, Wu K, Fuerst S V *Astron. Astrophys.* **545** A13 (2012)
187. Younsi Z, Wu K *Mon. Not. R. Astron. Soc.* **454** 3283 (2015)
188. Yuan F, Narayan R *Annu. Rev. Astron. Astrophys.* **52** 529 (2014)
189. Lu R-S et al. *Astrophys. J.* **859** 60 (2018)
190. Davies R D, Walsh D, Booth R S *Mon. Not. R. Astron. Soc.* **177** 319 (1976)
191. Falcke H, Markoff S, Bower G C *Astron. Astrophys.* **496** 77 (2009)
192. Doeleman S S et al. *Nature* **455** 78 (2008)
193. Brinkerink C D et al. *Astron. Astrophys.* **621** A119 (2019)
194. Fejer J A *Proc. R. Soc. Lond. A* **220** 455 (1953)
195. Rickett B J *Annu. Rev. Astron. Astrophys.* **15** 479 (1977)
196. Zhu Z, Johnson M D, Narayan R *Astrophys. J.* **870** 6 (2019)
197. Dexter J et al. *Mon. Not. R. Astrophys. Soc.* **442** 2797 (2014)
198. Chen Z et al. *Astrophys. J. Lett.* **882** L28 (2019)
199. Iwata Y et al. *Astrophys. J. Lett.* **892** L30 (2020)
200. Roelofs F et al. *Astron. Astrophys.* **625** A124 (2019)
201. Bower G C et al. *Astrophys. J.* **588** 331 (2003)
202. Marrone D P et al. *Astrophys. J.* **640** 308 (2006)
203. Murchikova E M et al. *Nature* **570** 83 (2019)
204. Baganoff F K et al. *Astrophys. J.* **591** 891 (2003)
205. Gardner F F, Whiteoak J B *Annu. Rev. Astron. Astrophys.* **4** 245 (1966)
206. Quataert E, Gruzinov A *Astrophys. J.* **539** 809 (2000)
207. Bondi H *Mon. Not. R. Astron. Soc.* **112** 195 (1952)
208. Edgar R *New Astron. Rev.* **48** 843 (2004)
209. Narayan R, Yi I *Astrophys. J. Lett.* **428** L13 (1994)
210. Di Matteo T et al. *Astrophys. J.* **582** 133 (2003)
211. Gralla S E, Holz D E, Wald R M *Phys. Rev. D* **100** 024018 (2019)
212. Mościbrodzka M et al. *Astrophys. J.* **706** 497 (2009)
213. Dexter J et al. *Astrophys. J.* **717** 1092 (2010)
214. Eatough R P et al. *Nature* **501** 391 (2013)
215. Bower G C et al. *Astrophys. J.* **868** 101 (2018)
216. Flamm L, Schumann R *Phys. Z.* **17** 448 (1916)
217. Einstein A, Rosen N *Phys. Rev.* **48** 73 (1935)
218. Wheeler J A *Phys. Rev.* **97** 511 (1955)
219. Kardashev N S, Novikov I D, Shatskiy A A *Int. J. Mod. Phys. D* **16** 909 (2007)
220. Novikov I D *Phys. Usp.* **61** 280 (2018); *Usp. Fiz. Nauk* **188** 301 (2018)
221. Novikov I D, Novikov D I *J. Exp. Theor. Phys.* **129** 495 (2019); *Zh. Eksp. Teor. Fiz.* **156** 585 (2019)
222. Field G B, Rogers R D *Astrophys. J.* **403** 94 (1993)
223. Lobanov A *Nat. Astron.* **1** 0069 (2017)
224. Johnson M D et al. *Astrophys. J.* **850** 172 (2017)
225. Bouman K L et al., arXiv:1711.01357
226. Palumbo D C M et al. *Astrophys. J.* **881** 62 (2019)
227. Shemmer O et al. *Astrophys. J.* **614** 547 (2004)
228. Liao N-H et al., arXiv:1807.05210
229. Ros E et al. *Astron. Astrophys.* **633** L1 (2020)
230. Ricci C et al. *Mon. Not. R. Astron. Soc.* **468** 1273 (2017)
231. Sanders D B et al. *Astrophys. J.* **325** 74 (1988)
232. Di Matteo T, Springel V, Hernquist L *Nature* **433** 604 (2005)
233. Bär R E et al. *Mon. Not. R. Astron. Soc.* **489** 3073 (2019)
234. Lagache G, Puget J L, Dole H *Annu. Rev. Astron. Astrophys.* **43** 727 (2005)
235. Persic M, Rephaeli Y *Mon. Not. R. Astron. Soc.* **403** 1569 (2010)
236. Rephaeli Y, Persic M, in *Cosmic Rays in Star-Forming Environments* (Astrophysics and Space Science Proc., Vol. 34, Eds D Torres, O Reimer) (Berlin: Springer, 2013) p. 193; arXiv:1304.0416
237. Anantharamaiah K R et al. *Astrophys. J.* **537** 613 (2000)
238. Rangwala N et al. *Astrophys. J.* **743** 94 (2011)
239. Downes D, Solomon P M *Astrophys. J.* **507** 615 (1998)
240. Barcos-Muñoz L et al. *Astrophys. J.* **799** 10 (2015)
241. Shchekinov Yu A, Vasiliev E O *Astrophysics* **60** 449 (2017); *Astrofizika* **60** 487 (2017)
242. Downes D, Eckart A *Astron. Astrophys.* **468** L57 (2007)
243. Paggi A et al. *Astrophys. J.* **841** 44 (2017)
244. Tunnard R et al. *Astrophys. J.* **800** 25 (2015)
245. Meijerink R et al. *Astron. Astrophys.* **525** A119 (2011)
246. García-Burillo S et al. *Astron. Astrophys.* **567** A125 (2014)
247. Liu L et al. *Astrophys. J.* **846** 5 (2017)
248. König S et al. *Astron. Astrophys.* **602** A42 (2017)
249. Chini R et al. *Astrophys. J.* **645** L61 (2006)
250. Zinchenko I et al. *Astrophys. J.* **810** 10 (2015)
251. Winn J N, Fabrycky D C *Annu. Rev. Astron. Astrophys.* **53** 409 (2015)
252. Gehrz R D et al. *Adv. Space Res.* **44** 413 (2009)
253. Pilbratt G L et al. *Astron. Astrophys.* **518** L1 (2010)
254. André P et al., in *Protostars and Planets VI* (Eds H Beuther et al.) (Tucson, AZ: Univ. of Arizona Press, 2014) p. 27; arXiv:1312.6232
255. Li G-X et al. *Astron. Astrophys.* **591** A5 (2016)
256. Pineda J L et al. *Astron. Astrophys.* **554** A103 (2013)
257. Langer W D et al. *Astron. Astrophys.* **561** A122 (2014)
258. Pineda J L, Langer W D, Goldsmith P F *Astron. Astrophys.* **570** A121 (2014)
259. Graf U U et al. *Astron. Astrophys.* **542** L16 (2012)
260. Bergin E A et al. *Nature* **493** 644 (2013)
261. Trapman L et al. *Astron. Astrophys.* **605** A69 (2017)
262. Kama M et al. *Astron. Astrophys.* **634** A88 (2020)
263. Venturini J, Ronco M P, Guilera O M *Space Sci. Rev.* **216** 86 (2020)
264. McKee C F, Ostriker E C *Annu. Rev. Astron. Astrophys.* **45** 565 (2007)
265. Tan J C et al., in *Protostars and Planets VI* (Eds H Beuther et al.) (Tucson, AZ: Univ. of Arizona Press, 2014) p. 149; arXiv:1402.0919
266. Bonnell I A, Bate M R, Zinnecker H *Mon. Not. R. Astron. Soc.* **298** 93 (1998)
267. Louvet F, in *SF2A-2018*: *Proc. of the Annual Meeting of the French Society of Astronomy and Astrophysics* (Eds P Di Matteo et al.) (2018) p. 311
268. van Dishoeck E F et al. *Publ. Astron. Soc. Pacific* **123** 138 (2011)
269. Mottram J C et al. *Astron. Astrophys.* **572** A21 (2014)
270. Güsten R et al. *Nature* **568** 357 (2019)
271. Corby J F et al. *Astron. Astrophys.* **610** A10 (2018)
272. Ceccarelli C et al. *Astrophys. J.* **850** 176 (2017)
273. Fontani F et al. *Astron. Astrophys.* **605** A57 (2017)
274. Codella C et al. *Astron. Astrophys.* **605** L3 (2017)
275. Punanova A et al. *Astrophys. J.* **855** 112 (2018)
276. Favre C et al. *Astrophys. J.* **859** 136 (2018)
277. Herbst E, van Dishoeck E F *Annu. Rev. Astron. Astrophys.* **47** 427 (2009)
278. McGuire B A *Astrophys. J. Suppl.* **239** 17 (2018)
279. McCarthy M C et al. *Nat. Astron.* **5** 176 (2021)
280. Watanabe N, Kouchi A *Astrophys. J.* **571** L173 (2002)
281. Shingledecker C N et al. *Astrophys. J.* **861** 20 (2018)
282. Vasyunin A I et al. *Astrophys. J.* **842** 33 (2017)
283. Garrod R T, Herbst E *Astron. Astrophys.* **457** 927 (2006)
284. Murga M S et al. *Russ. Chem. Rev.* **89** 430 (2020); *Usp. Khim.* **89** 430 (2020)
285. Jiménez-Serra I et al. *Astrophys. J. Lett.* **830** L6 (2016)
286. McGuire B A et al. *Science* **359** 202 (2018)
287. McGuire B A et al. *Science* **352** 1449 (2016)
288. Zeng S et al. *Mon. Not. R. Astron. Soc.* **484** L43 (2019)
289. Rivilla V M et al. *Mon. Not. R. Astron. Soc.* **483** L114 (2019)
290. Elsila J E, Glavin D P, Dworkin J P *Meteorit. Planet. Sci.* **44** 1323 (2009)
291. Altwegg K et al. *Sci. Adv.* **2** e1600285 (2016)
292. Pizzarello S, Zolensky M, Turk K A *Geochim. Cosmochim. Acta* **67** 1589 (2003)
293. Bailey J et al. *Science* **281** 672 (1998)
294. Modica P et al. *Astrophys. J.* **788** 79 (2014)
295. Cleeves L I et al. *Astrophys. J.* **819** 13 (2016)
296. Osamura Y, Roberts H, Herbst E *Astron. Astrophys.* **421** 1101 (2004)
297. Parise B et al. *Astron. Astrophys.* **416** 159 (2004)
298. Parise B et al. *Astron. Astrophys.* **453** 949 (2006)
299. Faure A et al. *Astron. Astrophys.* **584** A98 (2015)
300. Öberg K I et al. *Nature* **520** 198 (2015)
301. Walsh C et al. *Astrophys. J. Lett.* **823** L10 (2016)
302. Favre C et al. *Astrophys. J. Lett.* **862** L2 (2018)
303. Molyarova T et al. *Astrophys. J.* **866** 46 (2018)
304. Wiebe D S et al. *Mon. Not. R. Astrophys. Soc.* **485** 1843 (2019)
305. Lee J-E et al. *Nat. Astron.* **3** 314 (2019)
306. Snell R L et al. *Astrophys. J.* **539** L101 (2000)
307. Caselli P et al. *Astron. Astrophys.* **521** L29 (2010)
308. van der Tak F F S et al. *Astron. Astrophys.* **625** A103 (2019)
309. Hartogh P et al. *Nature* **478** 218 (2011)

310. Lis D C et al. *Astron. Astrophys.* **625** L5 (2019)
311. Ceccarelli C et al. *Astrophys. J.* **631** L81 (2005)
312. Jørgensen J K, van Dishoeck E F *Astrophys. J. Lett.* **725** L172 (2010)
313. Riviere-Marichalar P et al. *Astron. Astrophys.* **538** L3 (2012)
314. Notsu S et al. *Astrophys. J.* **836** 118 (2017)
315. Neish C D, Somogyi Á, Smith M A *Astrobiology* **10** 337 (2010)
316. Nimmo F, Pappalardo R T *J. Geophys. Res.* **121** 1378 (2016)
317. Lunine J I *Acta Astronaut.* **131** 123 (2017)
318. Waite J H (Jr.) et al. *Science* **311** 1419 (2006)
319. Waite J H et al. *Science* **356** 155 (2017)
320. Waite J H (Jr.) et al. *Nature* **460** 487 (2009)
321. Lunine J I, Lorenz R D *Annu. Rev. Earth Planet. Sci.* **37** 299 (2009)
322. Hayes A G *Annu. Rev. Earth Planet. Sci.* **44** 57 (2016)
323. Iess L et al. *Science* **337** 457 (2012)
324. Teolis B D et al. *Icarus* **284** 18 (2017)
325. Dalton J B et al. *Icarus* **177** 472 (2005)
326. Roth L et al. *Science* **343** 171 (2014)
327. Schubert G, Sohl F, Hussmann H, in *Europa* (The University of Arizona Space Science Series, Eds R T Pappalardo, W B McKinnon, K K Khurana with the assistance of René Dotson with 85 collaborating authors) (Tucson, AZ: Univ. of Arizona Press, 2009) p. 353
328. Sotin C, Tobie G, Wahr J, McKinnon W B, in *Europa* (The University of Arizona Space Science Series, Eds R T Pappalardo, W B McKinnon, K K Khurana with the assistance of René Dotson with 85 collaborating authors) (Tucson, AZ: Univ. of Arizona Press, 2009) p. 85
329. Khurana K K et al. *Nature* **395** 777 (1998)
330. Kivelson M G, Khurana K K, Volwerk M *Icarus* **157** 507 (2002)
331. Saur J et al. *J. Geophys. Res.* **120** 1715 (2015)
332. Wirström E S et al. *Astron. Astrophys.* **637** A90 (2020)
333. Hsu H-W et al. *Nature* **519** 207 (2015)
334. Postberg F et al. *Nature* **474** 620 (2011)
335. Sekine Y et al. *Nat. Commun.* **6** 8604 (2015)
336. Küppers M et al. *Nature* **505** 525 (2014)
337. De Sanctis M C et al. *Nat. Astron.* **4** 786 (2020)
338. O'Rourke L et al. *Astrophys. J. Lett.* **774** L13 (2013)
339. Stern S A et al. *Science* **350** aad1815 (2015)
340. de Bergh C et al., in *The Science of Solar System Ices* (Astrophysics and Space Science Library, Vol. 356, Eds M S Gudipati, J Castillo-Rogez) (New York: Springer Science + Business Media, 2013) p. 107
341. Müller T G et al. *Astron. Astrophys.* **518** L146 (2010)
342. Lellouch E et al. *Astron. Astrophys.* **557** A60 (2013)
343. Soderblom L A et al. *Science* **250** 410 (1990)
344. Robuchon G, Nimmo F *Icarus* **216** 426 (2011)
345. Hartogh P et al. *Planet. Space Sci.* **57** 1596 (2009)
346. Altwegg K et al. *Science* **347** 1261952 (2015)
347. Altwegg K, Balsiger H, Fuselier S A *Annu. Rev. Astron. Astrophys.* **57** 113 (2019)
348. Lis D C et al. *Astrophys. J. Lett.* **774** L3 (2013)
349. Teolis B D et al. *Astrobiology* **17** 926 (2017)
350. Shematovich V I *Solar Syst. Res.* **52** 371 (2018); *Astron. Vestn.* **52** 379 (2018)
351. Plainaki C et al. *Space Sci. Rev.* **214** 40 (2018)
352. Plavin A V et al. *Astrophys. J.* **908** 157 (2021)